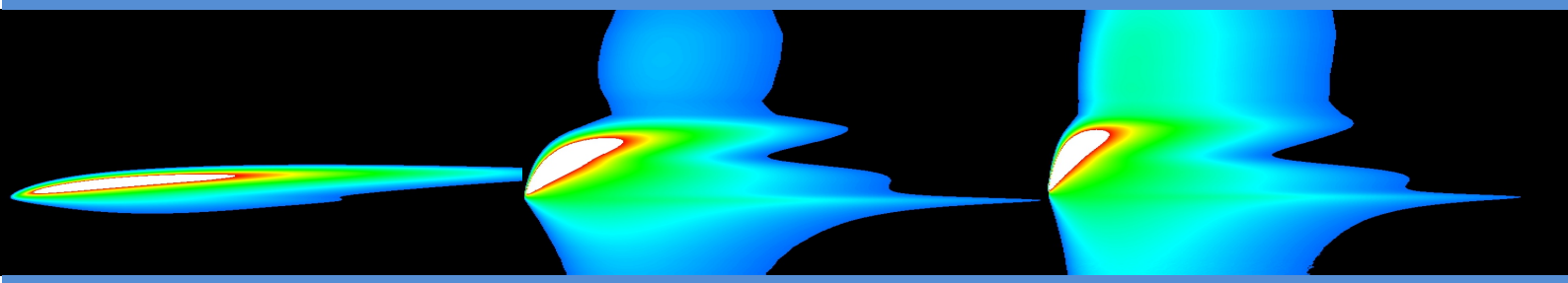

Nonlocal and Collective Phenomena in the Plasmons of Metallic Nanostructures

with application to ultrasensitive biosensing and nonlinear nano-optics

Christin David

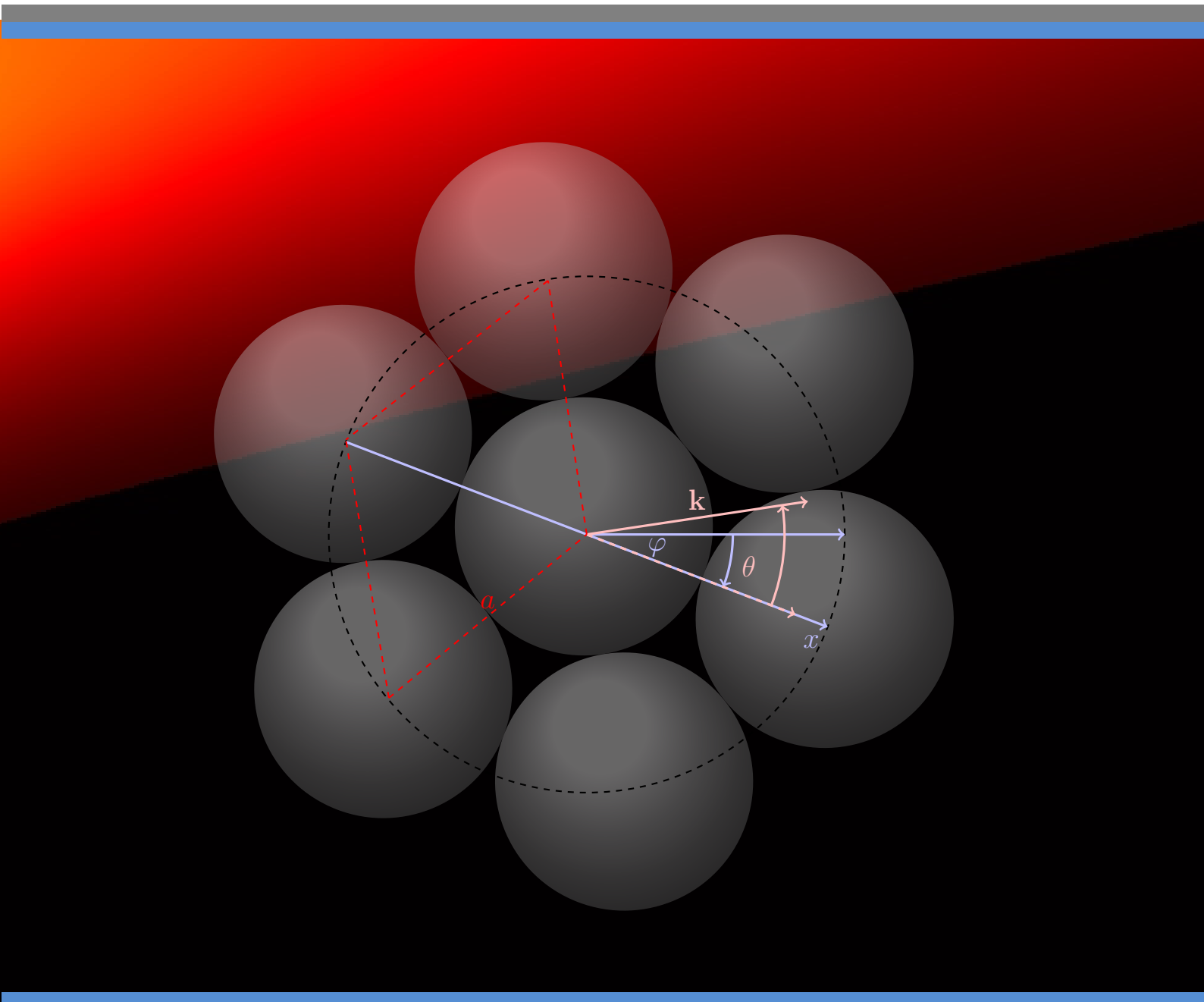

Nonlocal and Collective Phenomena in the Plasmons of Metallic Nanostructures

with application to ultrasensitive biosensing and nonlinear nano-optics

Universidad Autónoma de Madrid
Facultad de Ciencias
Departamento de Física de la Materia Condensada (DFMC)

Doctoral Thesis
en Física de la Materia Condensada y Nanotecnología

submitted by Christin David

June 3, 2014

Advisor:
Prof. Francisco Javier García de Abajo

- To my parents -

For their endless love and trust and for offering a place to always return to: home.

The present doctoral thesis was conducted in the Nanophotonics group supervised by Prof. F. Javier García de Abajo in the following locations

- Instituto de Óptica "Daza de Valdés", Consejo Superior de Investigaciones Científicas, Serrano 121, 28006, Madrid, Spain (IO-CSIC, 01/2010 - 09/2011)
- Instituto de Química-Física "Rocasolano", Consejo Superior de Investigaciones Científicas, Serrano 119, 28006, Madrid, Spain (IQFR-CSIC 10/2011 - 12/2013)
- Institut de Ciencies Fotoniques, Mediterranean Technology Park, Av. Carl Friedrich Gauss 3, 08860, Castelldefels (Barcelona), Spain (ICFO 01/2014 - 12/2014)

During the period of this research, funding was received by national and international sources. I would like to thank the Spanish Ministry of Education for financing the Spanish national projects NanoLight.es Consolider and Math2010-14885 and the European Commission for support of the FP7 European project LIMA. Furthermore, the PhD thesis has been made possible through an FPU fellowship (*Programa de Formación del Profesorado Universitario*) by the Spanish Ministry of Education (Ref. AP2010-0750).

Abstract

Plasmonics has provided us with a number of fascinating optical phenomena and taught us ways to squeeze light down to the nanometer scale. Current research, with emphasis on applied aspects, focuses on the design and experimental characterization of sensors, detectors and communication devices, such as compact optical switches and waveguides, all on the nanoscale. One of many challenges within this framework is to provide integrated building blocks in order to facilitate high-bandwidth and long-range plasmon propagation for many intriguing engineering applications. Beyond these technical complexities, there are other more fundamental ingredients in plasmonic nanostructures that need to be regarded when seeking for maximum field enhancement, super-focusing and improving the figures of merit within these components. Apart from resistive losses of metals, the dominant role played by quantum effects and, in particular, intrinsic nonlocality in the dielectric response are known to be limiting factors when aiming at the highest possible plasmonic robustness for full control of light.

Light-matter interaction in nanophotonics mainly involves processes within the electron subsystem in solids, crystals and molecules. Dealing with nanosized metal structures makes it therefore necessary to account for the quantum nature of electrons and include effects induced by the free conduction band electrons. Spatial inhomogeneities in the order of the electron Fermi wavelength produce scattering and interference modifying in turn the interaction of electrons with incoming light. The common local response approximation of material parameters does suppress the impact from short-range electron-electron interactions, which give rise to nonlocal effects. In general, these effects lead to additional damping and thus compromise idealized optical concepts, since plasmon resonances are broadened, undergo strong frequency shifts and become attenuated. The increased ability of fabricating suitable, nanosized structures to successfully observe these quantum effects has fueled the interest in theoretical studies of the impact of nonlocal optical response.

Spatial nonlocality is known to play an important role in nano-optics when nanometer-sized structures are involved. It arises from bulk properties as well as from edge effects, where in particular, the spill-out of electrons into the surrounding media influences the optical properties of metal nanostructures dramatically. The spill-out regions of two metal interfaces in close proximity to each other can overlap and thus from a tunneling junction not observed in classical electrodynamic theory. Local descriptions fail in the proximity of metal surfaces, in particular below distances of the spill-out size, typically about 0.25 nm. The optical response of nanosized metal structures is greatly influenced by the quantum confinement of their conduction electrons, which adds up to the intrinsic nonlocality in the response of homogeneous bulk media.

The first part of the present thesis aims to understand the physics of nonlocal effects by finding the limiting regimes of strutcural parameters in plasmonic devices in which the commonly used local approximation may break down. Furthermore, we analyse the role

of nonlocal effects in the optical field enhancement underlying a number of spectroscopical methods, such as in plasmonic assisted enhancement of photoluminescence (PL) and in surface enhanced Raman scattering (SERS).

We use a semi-classical approach to account for nonlocal interactions of the free electron gas. In the Bloch hydrodynamic model, the strength of the nonlocal response is quantified by a nonlocal parameter associated with the hydrodynamic pressure due to electron-electron interactions. The presence of additional pressure waves induced by the electron oscillation leads to a substantial change in the optical response of metal nanostructures. It is advisable to distinguish between bulk and edge nonlocality and discuss effects arising from these different aspects of the free electron density distribution. Inside the bulk of a metal nanostructure, the electrons are uniformly distributed and the presence of bound electrons (in alkali metals, such as Ag, Au) leads to a screening of the bulk plasma frequency. Towards the jellium edge and beyond, a smooth change in the electron density is observed which leads to two competing mechanisms: (i) The reduction of the electron density produces a redshift and (ii) the decreasing influence of the bound electrons elevates the screened bulk plasmon frequency and a blueshift is observed. For alkali metals, the net effect is a blueshift, but for simple metals (Na, Al) the redshift is dominant.

Including realistic electron density profiles, spreading into the dielectric or vacuum environment via a tunneling evanescent electron tail, molecules in the proximity of narrow gaps or metallic surfaces allow for complex interactions with the substrate. By extending our procedure to smooth metal surfaces, we can investigate nonlocal edge effects for both nonlocal and local metal structures. For larger systems, these edge effects induced by the electron spill-out are expected to play a minor role compared to nonlocal bulk effects that are subject to the uniform electron distribution inside the metal structure.

Besides exploring the fundamental nature of complex light matter interactions at the nanoscale, integrated building blocks for electro-optical devices used for sensing and communication applications demand a deep understanding of the effect of nonlocality. With the theoretical approach investigated in the first part of this thesis, we observe significant changes with respect to the common local approximation of metal optical properties and a remarkable impact on nanoscale applications. Comparison with available experiments results in excellent agreement with our parameter-free modeling of nonlocal effects. It is shown that nonlocality produces a sizable plasmon blue shift and broadening in a single metal nanoparticle (MNP) as well as in complex structures such as dimers, particle antennas and nanoshells. Analysis of the plasmon resonance dependence on the interparticle spacing and nanoparticle size allows us to additionally separate nonlocal and retardation effects. There are common conditions for which both of them coexist, giving rise to coexisting mechanisms of field enhancement and mode displacement.

This first main part of the present study is particularly relevant for broad, active areas involving applications of local field enhancement to biosensing and nonlinear optics in plasmonics. We provide an analytical insight into nonlocal plasmonic structures compris-

ing illustrative application-inspired examples, by deriving extended Mie coefficients for metal nanospheres and nanoshells. These can be used to calculate the optical response in complex aggregates of nanoparticles, such as dimers and nanoantennas, with a multiple scattering approach. This is compared to other semi-classical approaches, namely the specular reflection model employing a dielectric function accounting for nonlocal effects in the bulk material. A nonlocal analogue to Fresnel's optical coefficients is derived including the longitudinal pressure waves not present in the common local approximation. This allows us to study a variety of planar structures, such as metal slabs and metal-insulator-metal waveguides with intriguing properties for small slab thickness and gap size, respectively. Finally, we investigate realistic metal surfaces by setting up a numerical framework based on the transfer matrix approach to calculate optical properties for extended electron density profiles in the hydrodynamic model. This enables us to also study smooth electron distributions for systems using the local approximation. Comparing the optical response of both smooth local and nonlocal interfaces, we find tremendous differences with respect to bulk calculations indicating that the presence of a smooth electron distribution has a huge impact on the optical response even in local systems. Only for vanishing parallel momentum, i. e. for normal incidence, all considered theories coincide.

In the second part, we present and describe optical phenomena based on collective effects in nanoparticle arrays. MNP arrays have the ability of strongly confining photons in all three dimensions at the edge of band gaps found for the specific crystal structure yielding strong local field enhancements. Large area surface-plasmon-assisted enhancement of optical phenomena at nanostructured surfaces allows improving spontaneous as well as stimulated emission rates in single molecule fluorescence and photoluminescence of quantum dots, exploited for example in light emitting diodes, SERS, and photovoltaic (PV) nanodevices. In particular, 3rd generation solar cells benefit from the combined use of collective effects in novel photoactive layers. Nanoparticle assisted absorption enhancement is for instance compatible with the employment of photoluminescent nanocrystals, used for downshifting the incident light to energies close to the bandgap of Si. In this context, a very modest increase in efficiency with low cost increase can have dramatic consequences towards the solution of energetic and environmental problems of our society.

Optical near-fields in the vicinity of metal or dielectric microstructures display complex patterns upon external illumination that can be used for nanoscale imprinting on substrate surfaces. This is a promising concept for nanoprocessing large regular patterns, for example by arranging colloidal particles to form closed-packed layers that act as a mask. This has been used with different types of surfaces and for various particle materials and shapes. Engineered structures exploiting the focal points of the colloids become realizable in practice by angular beam scanning. Particle interaction and multiple scattering effects become important in the pattern formation of the optical near-fields for particles in a close-packed colloidal monolayer. This becomes apparent as a simple, linear superposition of the single particle interference patterns is not able to describe the resulting patterns.

In a combined experiment-theory study, we address the optical near-fields imprinted by colloidal particle arrays to gain insight into the underlying mechanisms of pattern formation. We discuss the possibility of imprinting a range of optical near-field nanostructured patterns into a photosensitive film using a 2D photonic crystal of polystyrene microspheres. Collective effects in the resulting colloidal monolayer produce a wealth of features, beyond a single region of field enhancement as typically reported and exploited, which enlarge the suite of achievable imprinted structures. Our numerical approach yields excellent agreement between experiments under varying illumination conditions. Several patterns are produced demonstrating the uniqueness of each pattern under changes of the experimental conditions, as well as the size of the spheres and even rotations of the hexagonal lattice with respect to the horizontal axis.

In photovoltaics, the conversion efficiency of a solar cell strongly depends on the light trapping mechanisms employed. The aim is to ensure a high efficiency of light absorption within an active volume of the solar cell to boost its carrier generation efficiency. The usage of anti-reflection coatings has improved the internal quantum efficiencies alongside with the continuous development of advanced cell technologies. Nanoparticle assisted light management opens the possibility of direct scattering light towards a higher index material, increasing the optical path length by scattering and to sensitizing light absorption in a semiconductor solar cell even below the band gap of the substrate. Various design principles have been formulated, with special interest in broadband absorption for cost efficient thin film cell technologies. Fundamental properties and efficiencies of devices using both regular and random arrays of a great variety of metal and dielectric nanostructures on the front or rear side of future solar cells have been actively studied both in theory and experiment.

Our first contribution to this research aims to provide a rapid theoretical assessment with a yet rigorous method to accomplish the design tasks. We discuss the absorption enhancement in a photovoltaic device comprised of a regular metal nanoparticle array using the optical analogue of a Salisbury screen, demonstrating 100% absorption not only at but beyond the plasmon resonance of the metal particle array applied. Moreover, we provide a second methodology to generate and characterize numerical samples of randomly distributed nanoparticles. This is compared to physical samples using their statistical data as an input to our modeling. Our contributions to the advancement in the design and understanding of 3rd generation solar cells is done in the framework of the European FP-7 project LIMA. The achievements of this European project have partly given rise to the results presented in the second main part of the present thesis.

Resumen

La plasmónica proporciona una serie de fenómenos ópticos fascinantes y nos enseña la manera de limitar y controlar la luz a la escala nanométrica. En la actualidad la investigación se centra en los aspectos aplicados, como por ejemplo en el diseño y la caracterización experimental de sensores, detectores y dispositivos de comunicación, tales como interruptores y guías compactas de ondas, todos en la nanoescala. Entre otros desafíos en este marco se encuentra el desarrollo de bloques de construcción integrados para facilitar un gran ancho de banda y una propagación de plasmónes de largo alcance para muchas aplicaciones en ingeniería. Más allá de estas complejidades técnicas, hay otros ingredientes más fundamentales en nanoestructuras plasmónicas que necesitan ser considerados en la optimización de campos cercanos. Estos son, la concentración total de ondas en un foco y la mejora de las figuras de mérito en estos componentes. Además de las pérdidas resistivas de los metales, efectos cuánticos y, en particular, la no localidad intrínseca en la respuesta dieléctrica, tienen un impacto apreciable y son conocidos por ser factores limitantes cuando el objectivo sea la máxima robustez plasmónica posible para el control total de la luz.

La interacción entre luz y materia en la nanofotónica implica principalmente procesos dentro del subsistema de electrones en sólidos, cristales y moléculas. Por lo tanto, tratando con estructuras metálicas nanométricas requiere darse cuenta de la naturaleza cuántica de los electrones e incluir los efectos inducidos por los electrones libres de la banda de conducción. Los defectos espaciales en sólidos en el orden de la Fermi longitud de onda de electrones producen dispersión e interferencia modificando a su vez la interacción de los electrones con la luz entrante. La aproximación más común de la respuesta local en los parámetros de los materiales suprime el impacto de las interacciones de corto alcance entre los electrones, que dan lugar a efectos no locales. En general, estos efectos dan lugar a una atenuación adicional y conceptos ópticos idealizados están comprometidos, ya que las resonancias de los plasmones se ensanchan y experimentan fuertes desplazamientos de la frecuencia. El aumento de la capacidad en la fabricación de estructuras adecuadas para observar con éxito estos efectos cuánticos ha impulsado el interés por los estudios teóricos sobre el impacto de la respuesta óptica no local.

La no localidad espacial juega un papel importante en la óptica cuando las estructuras de tamaño nanométrico están involucradas. Surge de las propiedades del bulk, así como de los efectos de borde, donde, en particular, el desbordamiento de electrones dentro el medio ambiente influye dramáticamente en las propiedades ópticas de nanoestructuras metálicas. Este es todavía más interesante, donde dos interfaces de metal se estrechan y los perfiles de densidad de electrones se solapan formando a un túnel energético entre dos regiones de metal clásicamente distintas. Las descripciones locales fallan en la proximidad de las superficies de un metal, en particular a distancias por debajo del desbordamiento de electrones de aproximadamente 0.25 nm. La respuesta óptica de estructuras metálicas nanométricas está fuertemente influenciado por el confinamiento cuántico de sus electrones de conducción, que

se suma a la no localidad intrínseca en la respuesta de los medios homogéneos del bulk.

La primera parte de la presente tesis tiene como objetivo comprender la física de los efectos no locales mediante la búsqueda de los regímenes restrictivos de parámetros strutcural en dispositivos plasmónicos donde la aproximación local podría fallar. Además, analizamos el papel de los efectos no locales en la mejora del campo óptico que está a la base de una serie de métodos espectroscópicos, como en la mejora asistida plasmónica de la fotoluminiscencia (PL) y la espectroscopia Raman (SERS).

Utilizamos un enfoque semi-clásico para introducir las interacciones no locales del plasma de electrones libres. En el modelo hidrodinámico de Bloch, la fuerza de la respuesta no local se cuantifica mediante un parámetro no local asociado con la presión hidrodinámica debido a las interacciones entre electrones. La presencia de ondas de presión inducidas por la oscilación de electrones conduce a un cambio sustancial en la respuesta óptica de nanoestructuras metálicas. Es conveniente distinguir entre la no localidad en el bulk y en el borde y discutir los efectos derivados de estos diferentes aspectos de la distribución de la densidad de los electrones libres. Dentro del bulk de una nanoestructura de metal, los electrones se distribuyen de manera uniforme y la presencia de electrones ligados (en metales alcalinos, tales como Ag, Au) eleva la frecuencia de plasma. Hacia el borde del *jellium* y más allá, se observa un cambio suave en la densidad de electrones que conduce a dos mecanismos que compiten entre sí: (i) La reducción de la densidad de electrones produce un desplazamiento hacia el rojo del espectro y (ii) la disminución de la influencia de los electrones ligados eleva la frecuencia de plasma y se observa un desplazamiento hacia el azul. Para los metales alcalinos, el efecto neto es un desplazamiento hacia el azul, pero para metales simples (Na, Al) el desplazamiento al rojo es dominante.

El hecho de incluir perfiles de densidad de electrones realistas, produce la difusión en el medio ambiente dieléctrico o el vacío a través de una cola evanescente (efecto túnel) de electrones. Esta cola evanescente permite interacciones complejas con el sustrato. Al ampliar nuestro procedimiento para superficies extensas de metal, podemos investigar los efectos de borde no locales, tanto para estructuras metálicas no locales y locales. En sistemas más grandes, se espera que estos efectos de borde inducidos por el desbordamiento de los electrones tienen menor importancia en comparación con los efectos de bulk no locales que están sujetos a la distribución electrónica uniforme dentro de la estructura metálica.

Además de explorar la naturaleza fundamental de la compleja interacción entre luz y materia en la nanoescala, bloques de construcción integrados para dispositivos electro-ópticos utilizados para aplicaciones en detección y comunicación exigen un profundo conocimiento de los efectos no locales. Una vez desarrollado el enfoque teórico, observamos cambios significativos con respecto a la aproximación local de las propiedades ópticas de metal y un impacto notable en las aplicaciones de escala nanométrica. La comparación con los experimentos disponibles resulta en excelente acuerdo con nuestro modelo de efectos no locales sin parámetros libres. Se muestra que la no localidad produce un desplazamiento considerable de la frequencia plasmónica y una reducción de las resonancias ensanchadas en partículas individuales, así

como en estructuras complejas tales como dímeros, antenas y nanocápsulas. El análisis de la dependencia de la resonancia de los plasmones en función de la distancia entre las partículas y el tamaño de las nanopartículas nos permite separar, además, los efectos no locales del retraso. Hay condiciones para que ambos coexistan, dando lugar a mecanismos que coexistan en la mejora del campo y en el desplazamiento de los modos.

Esta primera parte principal del presente estudio es particularmente importante para grandes áreas activas relacionados con las aplicaciones de mejora del campo cercano local para biosensores y efectos ópticos no lineales. Ofrecemos una teoría analítica a las estructuras plasmónicas no locales que rodean ejemplos de aplicación con una inspiración ilustrativa, derivando coeficientes Mie extendidos para nanoesferas de metal y nanocápsulas. Estos pueden ser usados para calcular la respuesta óptica en agregados complejos de nanopartículas, tales como dímeros y nanoantenas, con un enfoque de dispersión múltiple. Esto se compara con otros enfoques semi-clásicos, en particular, el modelo de la reflexión especular empleando una función dieléctrica incluyendo los efectos no locales en el bulk. Un análogo no local a los coeficientes ópticos de Fresnel se deriva incluyendo las ondas de presión longitudinales que no están presentes en la aproximación local. Esto nos permite estudiar una variedad de estructuras planas, tales como capas metálicas y guías de onda con una fisura dieléctrica con propiedades interesantes para espesores pequeños de la fisura y la separación, respectivamente. Finalmente, investigamos superficies metálicas realistas mediante la creación de un método numérico basado en el enfoque de matriz de transferencia. Este método permite calcular las propiedades ópticas de los perfiles de densidad electrónica extendidas en el modelo hidrodinámico. A su vez, esto nos permite estudiar las distribuciones de electrones suaves para los sistemas que utilizan la aproximación local. Comparando la respuesta óptica de ambas interfaces locales y no locales suaves, nos encontramos con enormes diferencias con respecto a los cálculos del bulk que indican que la presencia de una distribución de electrones suave tiene un gran impacto en la respuesta óptica, incluso en los sistemas locales. Sólo para un impulso paralelo desapareciendo, es decir, para incidencia normal, todas las teorías consideradas coinciden.

En la segunda parte de esta tesis, se presentan y describen los fenómenos ópticos basados en efectos colectivos en capas de nanopartículas. Estas capas de partículas metálicas tienen la capacidad de confinar fuertemente fotones en las tres dimensiones y en el borde de las bandas prohibidas encontradas para estructuras cristalinas, produciendo fuertes mejoras de campo locales. La mejora de campos cercanos en una gran área asistida por plasmones de superficie permite mejorar los fenómenos ópticos en superficies nanoestructuradas tal y como las emisiónes espontáneas y estimuladas en una molécula, la fluorescencia y fotoluminiscencia de los puntos cuánticos, explotados por ejemplo en diodos emisores de luz, la espectroscopia Raman (SERS), y dispositivos fotovoltaicos que emplean nanotecnología. En particular, las células solares de tercera generación se benefician de la utilización combinada de los efectos colectivos en nuevas capas fotoactivas. La mejora de la absorción asistida por nanopartículas es también compatible con el empleo de nanocristales fotoluminiscentes, utilizados para reducir la energía de la luz incidente acercandola a la banda prohibida de Silicio. En este contexto,

un aumento de la eficiencia junto con una reducción en los gastos puede tener consecuencias dramáticas para la solución de los problemas energéticos y ambientales de nuestra sociedad.

Los campos cercanos ópticos en la proximidad de microestructuras metálicas o dieléctricas muestran estampados complejos tras la iluminación externa que se puede utilizar para la impresión a la nanoescala en superficies de un sustrato. Este es un concepto prometedor para procesar grandes estampados regulares, por ejemplo, mediante la disposición de las partículas coloidales se forman capas hexagonales que actúan como una máscara. Esto ha sido utilizado con diferentes tipos de superficies y para diversos materiales y formas de partículas. En la práctica se pueden fabricar estructuras explotando los puntos focales de los coloides con un barrido angular del haz. Efectos de interacción entre las partículas y de la dispersión multiple son importantes en la formación de los estampados formados por los campos cercanos ópticos. Esto se hace evidente al considerar que una superposición simple y lineal de los estampados de interferencia de partículas individuales no es capaz de describir los estampados resultantes.

En un estudio combinado de experimento y teoría, nos dirigimos a los campos cercanos ópticos imprimidos por las capas de partículas coloidales que permite conocer mejor los mecanismos subyacentes de la formación de los estampados. Se discute la posibilidad de imprimir una serie de estampados nanoestructurados por el campo cercano en una película fotosensible usando un cristal fotónico 2D de microesferas de poliestireno. Efectos colectivos en la monocapa coloidal resultante producen una gran cantidad de características, más allá de una sola región de la intensificación del campo cercano, que amplia la gama de estructuras alcanzables. Nuestro enfoque numérico produce un acuerdo excelente entre los experimentos bajo condiciones variables de iluminación. Producimos varios estampados demostrando la singularidad de cada estampado en virtud de los cambios de las condiciones experimentales, así como el tamaño de las esferas e incluso rotaciones de la rejilla hexagonal con respecto al eje horizontal.

En la fotovoltaica, la eficiencia de la conversión de una célula solar depende en gran medida de los mecanismos de retención de la luz empleados. El objetivo es garantizar una alta eficiencia de absorción de la luz dentro de un volumen activo de la célula solar para aumentar su eficiencia de la generación de portadores de carga. El uso de recubrimientos antirreflectantes ha mejorado la eficiencia cuántica interna junto con el desarrollo continuado de las tecnologías avanzados de las celulares. La gestión de la luz asistida por nanopartículas abre la posibilidad de dirigir la luz dispersada hacia un material de índice más alto, para aumentar la longitud del camino óptico por la dispersión y para sensibilizar a la absorción de luz en una célula solar de semiconductores incluso por debajo de la banda prohibida del sustrato. Varios principios de diseño se han formulado, con interés en la absorción con banda ancha para las tecnologías de células solares de películas finas rentables. Hemos estudiado propiedades fundamentales de forma activa tanto teórica como experimentalmente la eficiencia de los dispositivos que utilizan capas tanto regulares como aleatorias de una gran variedad de nanoestructuras metálicas y dieléctricas en la parte frontal o trasera de las futuras células solares.

Nuestra primera contribución a esta investigación tiene como objetivo proporcionar una evaluación teórica rápida con un método riguroso para cumplir las tareas de diseño. Se dis-

cute la mejora de la absorción en un dispositivo fotovoltaico compuesto por una capa de nanopartículas de metal regular usando el análogo óptico de una pantalla de Salisbury, lo que demuestra la absorción de 100 %, más allá de la resonancia de plasmones de la capa de partículas aplicadas. Además, ofrecemos una segunda metodología para generar y caracterizar muestras numéricas de nanopartículas distribuidas al azar. Esto se compara con las muestras físicas utilizando sus datos estadísticos como aportación a nuestro modelo. Nuestras contribuciones al avance en el diseño y la comprensión de las células solares de tercera generación se realiza en el programma de marco FP-7 del proyecto LIMA. El rendimiento de este proyecto Europeo han dado lugar en parte a los resultados presentados en la segunda parte de la presente tesis.

Publications and conference contributions

Every year, especially since 1563, the number of writings published in every field is greater than all those produced in the past thousand years.

(Johannes Kepler)

Papers published in the framework of the present doctoral thesis and earlier scientific contributions by the doctorate candidate are listed in the following. In addition, numerous appearences in Spanish national and international conferences have been made, yielding a total of 10 oral contributions and 13 poster presentations (see below).

1. **Christin David** and F. Javier García de Abajo. Surface plasmon dependence on the electron density profile at metal surfaces. (submitted), 2014

2. **Christin David** and F. Javier García de Abajo. Towards total absorption in photovoltaics with the Salisbury screen. (submitted), 2014

3. **Christin David**, Paul Kühler, F. Javier García de Abajo, and Jan Siegel. Near-field nanoimprinting using colloidal monolayers. *Opt. Express*, 22(7):8226–8233, 2014

4. **Christin David**, N. Asger Mortensen, and Johan Christensen. Perfect imaging, epsilon-near zero phenomena and waveguiding in the scope of nonlocal effects. *Sci. Rep.*, 3:2526, August 2013

5. F. Cortés-Juan, C. Chaverri Ramos, J. P. Connolly, **Christin David**, F. J. García de Abajo, J. Hurtado, V. D. Mihailetchi, S. Ponce-Alcántara, and Guillermo Sánchez Plaza. Effect of Ag nanoparticles integrated within antireflection coatings for solar cells. *Journal of Renewable and Sustainable Energy*, 5(3):033116, 2013

6. **Christin David**, James P. Connolly, Christian Chaverri Ramos, F. Javier García de Abajo, and Guillermo Sánchez Plaza. Theory of random nanoparticle layers in photovoltaic devices applied to self-aggregated metal samples. *Solar Energy Materials and Solar Cells*, 109(0):294–299, 2013

7. **Christin David** and F. Javier García de Abajo. Spatial nonlocality in the optical response of metal nanoparticles. *J. Phys. Chem. C*, 115(40):19470–19475, 2011

As a special achievement during my PhD phase, I consider my contribution to the organization of the "Nanophotonics for photovoltaics, a step forward" workshop held in Valencia, Spain, in November 2012 as part of finalizing the FP7-ICT-248909-LIMA (European Commission project) (LIMA) project. Here, I was encouraged to organize and chair the session

and panel discussion "Enhanced light management by exploiting (plasmonic) nanostructures". I am especially thankful to the participation of Supriya Pillai (ARC Photovoltaic Centre of Excellence, UNSW, Australia), Vivian Ferry (UC Berkeley/Lawrence Berkeley National Laboratory, USA) and Pierpaolo Spinelli (FOM Institute AMOLF, Netherlands) in this session.[8]

The following presentations on conferences were made

i. **Christin David** and F. Javier García de Abajo. Inclusion of nonlocal effects in the hydrodynamic description of metal surfaces with smooth density profiles, talk, Progress in electromagnetics research symposium, 34th PIERS, Stockholm, Sweden (2013)

ii. **Christin David**, N. Asger Mortensen, Johan Christensen. Perfect Imaging and ENZ Phenomena for Metallic Slabs in the scope of Nonlocal Effects, talk, Progress in electromagnetics research symposium, 34th PIERS, Stockholm, Sweden (2013)

iii. 3 posters at the 6th International Conference on Surface Plasmon Photonics SPP6, Ottawa, Canada (2013)

iv. **Christin David** and F. Javier García de Abajo. Nonlocal Effects: A classical description of quantum effects with the hydrodynamic model, poster, 4th International Topical Meeting on Nanophotonics and Metamaterials, NanoMeta 2013, Seefeld, Austria (2013)

v. Organization and chairing of the session and panel discussion "Enhanced light management by exploiting (plasmonic) nanostructures", Workshop: Nanophotonics for photovoltaics, a step forward, Valencia, Spain (2012)

vi. **Christin David** and F. Javier García de Abajo. Nonlocal effects in Plasmonic devices, talk and 2 posters, Near-field optics NFO, San Sebastian, Spain (2012)

vii. **Christin David** and F. Javier García de Abajo. Nonlocal effects in Plasmonic devices, poster, GRC on Plasmonics 2012, Waterville, ME, USA (2012)

viii. **Christin David** and F. Javier García de Abajo. Effects of Spatial Dispersion in the Optical Response of Plasmonic Nanostructures, poster, Nanolight, Benasque (2012)

ix. **Christin David**, James P. Connolly, Christian Chaverri Ramos, F. Javier García de Abajo, and Guillermo Sánchez Plaza. Towards Efficient Integration of MNP Layers in Photovoltaic Devices, talk, PlasMeta, Samarkand, Uzbekistan, (2011)

x. 2 posters, International Workshop on Nanoplasmonics for Energy and the Environment IWONEE, Sanxenxo, Spain (2011)

xi. **Christin David** and F. Javier García de Abajo. Effects of Spatial Dispersion in the Optical Response of Plasmonic Nanostructures, talk, 5th International Conference on Nanophotonics ICNP'2011, Shanghai, China (2011)

xii. **Christin David** and F. Javier García de Abajo. Spatial Nonlocality in the Optical Response of Metal Nanoparticles, poster, 5th International Conference on Surface Plasmon Photonics SPP5, Pusan, Corea (2011)

xiii. **Christin David** and F. Javier García de Abajo. Nonlocal Effects in the Optical Response of Plasmonic Nanostructures, talk, 4th Young Scientist Meeting on Metamaterials YSMM'2011, Valencia, Spain (2011)

xiv. **Christin David** and F. Javier García de Abajo. Nonlocal Effects in the Optical Response of Plasmonic Devices, poster, 3rd International Topical Meeting on Nanophotonics and Metamaterials, NanoMeta 2011, Seefeld, Austria (2011)

xv. **Christin David** and F. Javier García de Abajo. Spatial Nonlocality in the Optical Response of MNPs, talk, 3rd International Workshop TaCoNa-Photonics, Bad Honnef, Germany (2010)

xvi. **Christin David** and F. Javier García de Abajo. Spatial Nonlocality in the Optical Response of Metal Nanoparticles, poster, poster, DIPC Passion for Knowledge, San Sebastian, Spain (2010)

xvii. **Christin David** and F. Javier García de Abajo. Spatial Nonlocality in the Optical Response of Metal Nanoparticles, talk, Ultrafast Nanooptics, UNO-2, Bad Dürkheim, Germany (2010)

xviii. **Christin David** and F. Javier García de Abajo. Spatial Nonlocality in the Optical Response of MNPs, talk, Conferencia Española de Nanofotonica CEN2010, Segovia, Spain (2010)

Earlier publications originating in the work for my Diploma thesis are

8. **Christin David**, Marten Richter, Andreas Knorr, Inez M. Weidinger, and Peter Hildebrandt. Image dipoles approach to the local field enhancement in nanostructured Ag-Au hybrid devices. *The Journal of Chemical Physics*, 132(2):024712, 2010

9. Jiu-Ju Feng, U. Gernert, M. Sezer, U. Kuhlmann, D. H. Murgida, **Christin David**, Marten Richter, Andreas Knorr, Peter Hildebrandt, and Inez M. Weidinger. Novel Ag-Au Hybrid Device for Electrochemical SE(R)R Spectroscopy in a Wide Potential and Spectral Range. *Nano Letters*, 9 (1):298–303, 2009

leading to 2 oral presentations in 2009.

xix. **Christin David**, Marten Richter, Andreas Knorr, Peter Hildebrandt, and Inez M. Weidinger, Plasmonic Optical Enhancement in an Ag-Au Hybrid Device for Bio Sensors, talk, DPG Spring Meeting of the Condensed Matter Section, Dresden, Germany (2009)

xx. **Christin David**, Marten Richter, Andreas Knorr, Peter Hildebrandt, and Inez M. Weidinger, Plasmonic Optical Enhancement in Hybrid Devices for Bio Sensors, talk, International Conference on Physics of Optical Materials and Devices (ICOM), Herceg-Novi, Montenegro (2009)

Contents

List of Figures

List of Tables

Abbreviations

BEM boundary element method

DFT density functional theory

EBL electron beam lithography

FTIR Fourier transform infrared spectroscopy

FDTD finite difference time domain

GST $Ge_2Sb_2Te_5$

IBC integrated back contact

KKR Korringa-Kohn-Rostoker method

LIMA FP7-ICT-248909-LIMA (European Commission project)

LDOS local density of optical states

LSPR localized surface plasmon resonance

NSA nanosphere self-aggregation method

MNP metal nanoparticle

MEG multiple exciton generation

PPL plasmonic particle layer

PL photoluminescence

PS polystyrene

PV photovoltaic

REBL random electron beam lithography

SEM scanning electron microscopy

SERS surface enhanced Raman scattering

SPP surface plasmon polariton

SRM specular reflection model

(TD)LDA (time dependent) local density approximation

1 Motivation

> Whenever we proceed from the known to the unknown we may hope to understand, but we may have to learn at the same time a new meaning of the word "understanding".
>
> *(W. K. Heisenberg)*

Nanophotonics comprises the science and technology of confined light and electron waves, investigating opto-electronical properties within nanoscale structures. Spatial confinement of photons has a crucial impact on the propagation of light and light-matter interaction that opens up exciting branches in optics.[11–13] In particular, metal nanostructures display unique properties of light concentration and local field enhancement due to electron excitation at interfaces and in small particles. The systematic generation and processing of light, its engineered absorption and emission in various structured devices and designs is studied and exploited for telecommunications, data storage and routing, energy harvesting, bio-sensing, and medical applications ranging from imaging to actual surgery.[14–20] A variety of nanostructures has been designed to address different tasks in light management in the spectral regimes of interest between the ultraviolet (UV) to the near-infrared (NIR), about 100 nm to 2000 nm.[21–24] The large field enhancement observed at roughened metal surfaces can be used for instance to unveil the presence of minute concentrations of biomolecules, which one may then detect optically, with a sensitivity that goes down to the single-molecule level, mainly via surface enhanced Raman scattering (SERS).[9,10,14,25]

Plasmons are the quasi-particles formed by the collective excitation of electrons in metal nanostructures and particles (MNPs). They allow us to design opto-electronical elements with dominant surface effects and a strong concentration of electromagnetic radiation, which can be used to modify the transition rates of nearby scatterers, e. g. molecules and quantum dots. Plasmons are very sensitive to the permittivity of their environment, which enables plasmon based sensor technology. The number of applications seems endless and novel concepts for light emitting devices,[26,27] ultrasensitive spectral analysis,[9,10,14] enhanced light harvesting mechanisms[28–30] and nonlinear processes[31–34] on the nanoscale are all building bricks for future photonic circuitry merging electronics and photonics.

The present doctoral thesis dives into two particular topics of (a) nonlocal phenomena in nanoplasmonic devices, where the dynamics of free electrons in metal nanostructures is of special interest,[1,4,7] and (b) collective effects with emphasis on the study of optical near-fields[3] and next generation photovoltaics.[2,5,6,35]

1.1 Nonlocal effects

Finite size effects in the optical response of metal nanoparticles are long since known and exploited in arts and technology, see Fig. 1.1 (a). A sizeable spectral shift in both gold and silver nanoparticles is found upon decreasing their sizes. The central inset in Fig. 1.1 (a) shows the spectral range covered by both Au and Ag colloids dispersed in water for sizes between 20 nm – 200 nm. Optical effects from transmitted and scattered light as observed in the coloring of stained glass windows have been phenomenologically attributed to a reduced mean free path length between scattering events of electrons in nanostructures.[36] Moreover, the large-k response that originates in the sub-wavelength oscillations of plasmonic excitations is an inherent prerequisite for many intriguing wave phenomena such as perfect imaging and the epsilon-near-zero regime.[37,38] While there is no upper wavelength cut-off within the local response approximation of the plasma polarization, nonlocal dynamics suppresses response beyond ω/v_F, where v_F is the Fermi velocity of the electron gas.

Light-matter interaction involves processes within the electron subsystem in solids, crystals and molecules. Classically, electrons in solid matter when exposed to an electromagnetic field display a polarization field expressed in terms of the permittivity ϵ of the bulk material. Boundaries between regions of different material composition are usually described as abrupt interfaces and two-dimensional surface charges are induced, see illustration in Fig. 1.2, while the presence of electrons beyond that interface is neglected.

However, electrons are themselves waves characterized by the de Broglie wavelength[39] $\lambda_e = \frac{h}{\sqrt{2m_e E}}$ where $h = 2\pi\hbar = 6.63\times10^{-34}$ Js is Planck's constant,[40] $m_e = 9.1\times10^{-31}$ kg is the electron (effective) mass depending on the bulk material and E is the energy of the electron wave. Typically, this wavelength is about 7.5 nm in solids at room temperature $T = 300$ K, where $E = k_B T$ and $k_B = 1.38\times10^{-23}$ J/K is the Boltzmann constant.

Inhomogeneities on this length scale produce scattering and interference effects of electrons which mutually interact with the incoming light. The surface of metal nanostructures is the main source of electron scattering, where the surface-to-volume ratio indicates the importance of scattering events at the surface. The common local approximation of material parameters does suppress the impact from short-range electron-electron interactions giving rise to nonlocal effects.

A metal is composed of bound electrons attached to the positive atomic cores and the conduction band electrons that can freely move within the atomic crystal structure. At a realistic metal surface, free electrons extend into the surrounding vacuum or dielectric medium, see Fig. 1.1 (b). The smooth electron density distribution around metal interfaces can be found using *ab initio* methods, indicating that a nonvanishing contribution is still found at a distance of about 0.25 nm from the physical boundary, the jellium edge.[42,43] This is in

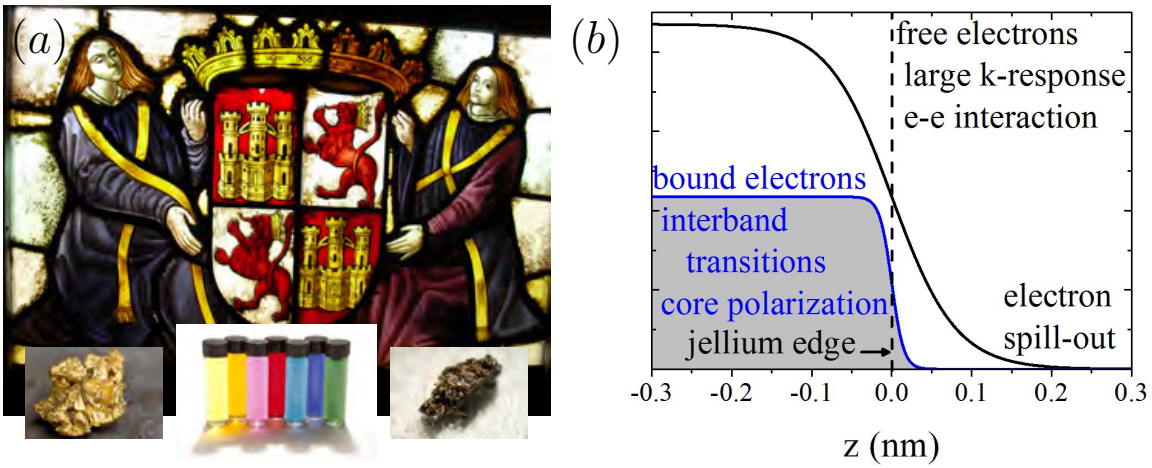

Fig. 1.1: **Finite size effects in metal nanoparticles in arts and technology.** (a) Scattered colors by MNPs of different sizes in ornamental glasses at the Alcázar of Segovia, Spain. Lower insets from left to right: Native gold, MNPs in solution advertised by *nanocomposix.com Europe* and native silver.[41] (b) Realistic metal surfaces consist of bound electrons and free conduction band electrons.

particular relevant where two metal interfaces are in close proximity to each other. An emitter placed in this region experiences an increased electron density and, moreover, plasmons can oscillate through a tunneling junction between particles and interfaces.[44,45]

Upon illumination, boundary charges are accumulated at the surface. While in a local theory this yields a delta-function-like surface distribution, see insets in Fig. 1.2, a nonlocal theory predicts a finite, extended distribution of the induced charges of characteristic penetration depth comparable to the electron spill-out.[42]

Electron confinement has mostly been studied in semiconductors and dielectrics since the 1970s. Size dependent absorption and emission spectra and transmission probabilities in e. g. semiconductor quantum dots are used to tune spectral parameters in lasers, emitters, switches, filters and electro-optical modulators.[11]

An accurate description of nonlocal electron-electron interaction in metals requires using first-principle methods, e. g. density functional theory (DFT).[43–47] Unfortunately, even when strong approximations are made, such as the (time dependent) local density approximation ((TD)LDA), these methods require extremely demanding computations, which limit their applicability to particles of a few nanometers in size using currently available computers.[48] Here, Schrödinger's equation is solved for a large, but finite number of electron wave functions from all atoms in the considered system which results in complex and time-consuming algorithms. The quantum optics of nanostructures provides a useful approach towards nonlocal phenomena and is used to engineer the local density of optical states (LDOS) of a nanostructure, the spontaneous emission and confined light-matter states in photonic crystals and microcavities.[49–51] A further significant advantage of first-principle methods is that they allow one to incorporate the effect of the spill-out of the electron density outside the metal surface,

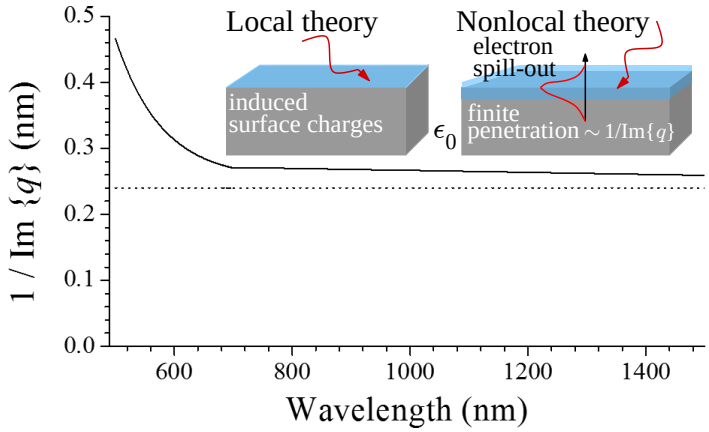

Fig. 1.2: **Penetration depth of the screening charge** (solid curve) and extension of the conduction electron density profile outside the surface of gold[42] (broken line). The insets represent the finite penetration of the induced charge inside the metal due to nonlocal effects (right), in contrast to the surface-delta-function distribution predicted by local theory (left).

see Figs. 1.1 (b) and 1.2. The density profile extends 0.20—0.25 nm outside the metal[42] (i. e. outside the jellium edge, which is customarily chosen at half an interlayer distance outside the outermost atomic layer) and thus contributes with tunneling currents to the response of surfaces in close proximity. Recent progress in this direction has been made by describing conduction electrons in dimers,[44] rods,[49] and planar surfaces[52] as a jellium and deriving the optical response from a (TD)LDA formalism. A conclusive solution to this problem might ultimately involve some kind of hybrid formulation in which short distances are described *ab initio* while larger distances are handled by using a classical formalism.

Efforts to extend the classical Mie theory[53] to incorporate collective effects of the conduction band electrons are made since the 1980s.[54–62] Further advanced material models can be derived from perturbative theories[63] or by separating the free electron dynamics from the core electron polarization via the hydrodynamic equation for an electron plasma.[4,7,64–78] An increased interest in nonlocal effects and their theoretical description has taken place during the past few years, partly due to improved theoretical approaches and the increased ability of fabricating structures to directly or indirectly observe these quantum effects.[79–81]

Effects due to freely moving yet confined electrons in plasmonic nanostructures and particles form the first main part of this thesis. We hereby employ the mentioned hydrodynamic approach to study finite size effects, identifying limits where the local approximation is no longer valid. Nonlocal response has previously been found to pose limitations to field-enhancement phenomena and a variety of nanoparticles and plasmonic structures are investigated. More importantly, we explore the possibility of describing a metal-dielectric interface within this semi-classical approach not only for sharp, i. e. abrupt interfaces, but also for realistic, smoothly changing electron densities, extending into the dielectric surrounding. Electron density profiles are taken from *ab initio* calculations.[42] The nonlocal theory developed for

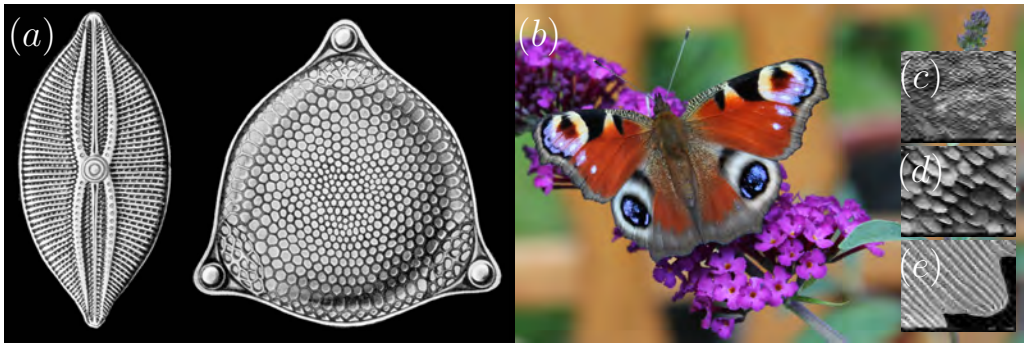

Fig. 1.3: **Periodic structures in nature.** (a) Examples of diatom water plants. (b) The wings of butterflys are formed by nano scales leading to interferential coloring. The explicit periodic nanostructure is revealed by SEM graphs with (c) 50, (d) 100 and (e) 5000-fold magnification.

sharp interfaces is used in a transfer matrix approach to also describe metal surfaces characterized by smooth electron density profiles. Interestingly, such a smooth interface leads to similar results when described both with local and nonlocal material parameters, dominated more by profile smoothness than nonlocal effects.

Developping our nonlocal methodology in these two steps, allows us to clearly distinguish between nonlocal bulk and nonlocal edge effects and discuss the impact of smooth interfaces on the optical response independently of the influence of nonlocal effects.

1.2 Collective effects

Light incident on a layer of a periodic particle array or grating is sensitive to inhomogeneities in space, i. e. of the permittivity ϵ. Multiple, coherent scattering and interference phenomena occur that lead to unique optical properties in such periodic structures. This involves resonance conditions determined by the geometry of the nanostructure and its environment. Already known from classical electrodynamics since Newton[82] (interference phenomena) and Lord Rayleigh[83] (reflection bands in periodically layered media), light wave confinement in these photonic crystals is in complete analogy to electron confinement and Bloch waves in solids. A periodic potential gives rise to a specific bandstructure defining frequency ranges of allowed and forbidden particle wave propagation. In photonic crystals, standing wave solutions define bands and only evanescent waves are found within band gaps (reflection bands). This effect is used e. g. for cut-off filters for UV light. The tunable optical near-fields in such systems open up a number of optical media storage solutions.[84–93] Artificially designed metamaterials are exploited in photonic circuitry, designing optical cavities and compact waveguides. The symmetries in photonic crystals allow for different theoretical approaches from plane-wave solutions to multiple scattering theory.

Interestingly, an inspiring source of concepts of photonic crystals in science and technology

is given by nature herself, with a sometimes surprising ingenuity and a number of elaborate designs found in natural structures, including animate beings. Evolution led to surfaces optimized for the interplay with light such as anti-reflection coatings or interferential coloration for shells, wings of insects or feathers of birds, Fig. 1.3. This absorptionless coloration technique does not undergo heating nor photobleaching with time. A further example are the iridescent colors in gem opals and other pearls. A periodic, but porous topology in plants or corals enables feasible physio-chemical exchange processes, e. g. for light harvesting, and from a mechanical point of view an often high durability is given due to the optimal combination of weigth and hardness. Interestingly, diatom water plants (Fig. 1.3 (a)) can actually be used as photonic crystal fibers and are applicable for laser experiments.[94]

In the second part of this thesis, we investigate the pattern formation on photosensitive thin films induced by laser irradiation of a regular monolayer of dielectric colloids. The wealth of produced features and the periodicity of the imprinted near-field intensity can be used for large area nanoprocessing.

Light propagation in non-periodic structures, such as in randomly distributed particle arrays or rough surfaces, equally obeys the propagation laws given by Maxwell's equations (1861, 1862). It can be seen as the light scattering analogue to diffuse electron transport, where multiple scattering events, despite random features, allow for theoretical investigations to some extent. Roughened metal surfaces are used to enhance the signal in SERS[9,10] and for other spectral measurement methods. Random particle layers show some advantages over regular arrays and vice versa, depending on the application.

Nanotechnology for photovoltaic devices

The development of efficient devices for energy harvesting from regenerative energy sources is of utmost importance to face the future energy needs of our society. The increasing green awareness has led to a number of political changes in the past years towards the application of energy friendly technologies in everyday life, e. g. in domestic appliances. This "energy revolution" needs reliable and environmentally friendly energy sources, of which the renewable energies are of utmost significance.

Energy source	Electricity generating costs in $ per kWh
Nuclear power	0.050 - 0.137
Black coal	0.085 - 0.110
Wind energy	0.090 - 0.261
Hydro-electric	0.074 - 0.459
Photovoltaic	0.287 - 0.616

Table 1.1: Electricity generation costs from different energy sources for the OECD region.[95]

Solar energy remains one of the most attractive energy sources of our planet, but its generation is still more expensive than electricity extracted from carbon, gas or nuclear power. We compare the costs for generating a kWh of electricity from different sources in table 1.1.[95] The

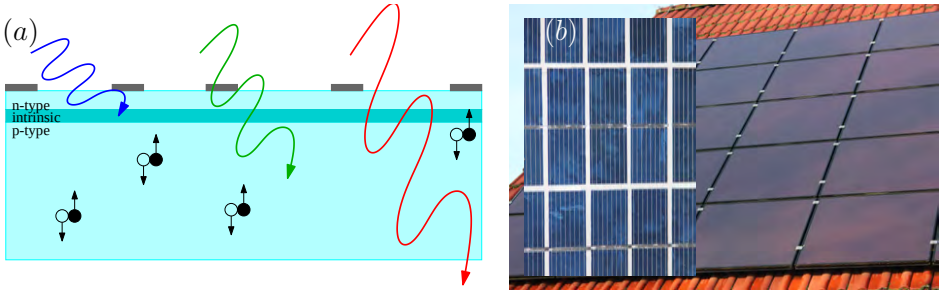

Fig. 1.4: **Introducing nanophotonics for photovoltaics.** (a) A conceptual sketch of carrier separation in a standard pnp-type solar cell. Low energy light components benefit from the plasmon assisted increase of the optical interaction time associated with scattering. (b) Commercial solar cells for private households are mostly based on large scale multicrystalline Si-wafer technology.

basic idea behind solar energy harvesting is the separation of carriers, electrons and holes, in a photoactive medium with excitation energies within the solar spectrum, see Fig. 1.4 (a). To become more competitive and widespread, solar cell technology has to face several aspects that keep it at relatively low conversion efficiencies, such as recombination and reflection losses. Also, referring to material and fabrication costs in terms of yield losses, a minimum cell thickness is needed in order to equally absorp light of different wavelengths.

Despite lab prototypes being close to the theoretical efficiency limits (31% in the classical Shockley Queissler limit), the exploitation of quantum effects, in particular light driven processes such as multiple exciton generation (MEG)[96,97] and secondary radiation such as photoluminescence (PL),[98] could lead to efficiencies as high as 70%.

State-of-the-art solar cells,[99] often based on indirect band gap materials - Si and gallium compounds - achieve between 18.5% (multicrystalline) and 22.4% (large crystalline) conversion efficiency for terrestial modules under laboratory conditions. This is to put it into perspective with other cell technologies, such as organic, photochemical or two-terminal technology which are summarized in table 1.2.

In 3rd generation photovoltaics, nanostructures are exploited to significantly enhance the light absorption efficiency in solar cells. As part of the LIMA project to "Improve Photovoltaic efficiency by applying novel effects at the limits of light to matter interaction", we were leading a specific workpackage to develop a plasmonic particle layer (PPL) on top of the solar cell structure to increase light management in the device.[5,6,8,100,101]

Plasmonics for solar cells is a promising concept to achieve this, since MNPs enhance light coupling in solar cells by means of efficient scattering,[102–104] making them well suited to 3rd generation photovoltaic devices and enabling cost reduced thin film cell technology.[104–110] More generally, plasmon-assisted efficiency enhancement of solar cells may involve two classes of phenomena: (a) Resonant, collective effects with strong local fields in the vicinities of the MNPs that can be used to amplify not only photon absorption, but also MEG and PL effects. (b) For all frequencies, scattering effects based on a weak coupling within the periodic structure are observed which increase the optical path length. Furthermore, nanopar-

Module type	Measured efficiency	Date
Si (multicrystalline)	$18.5 \pm 0.4\%$	01/12
Si (large crystalline)	$22.4 \pm 0.6\%$	08/12
GaAs (thin film)	$24.1 \pm 1.0\%$	02/13
Organic polymer (thin film)	$10.7 \pm 0.3\%$	01/13
Dye sensitized (photochemical)	$11.9 \pm 0.4\%$	09/12
InGaP/GaAs/InGaAs (2-terminal)	$37.9 \pm 1.2\%$	02/13

Table 1.2: Overview of several state-of-the-art solar cell efficencies.[99]

ticle assisted absorption enhancement is a compatible technology for the usage with other nanoscale concepts such as photoluminescent nanocrystals.[8,98] The usage of anti-reflection coatings has improved the internal quantum efficiencies alongside with the continuous development of advanced cell technologies.[111–116] Various design principles have been formulated.[6,18,22,103,117–129] Fundamental properties and efficiencies of devices using both regular and random arrays[6,8,98,110,129] of a great variety of metal and dielectric[108,114,115,120] nanostructures on the front or rear[122,128] side of future solar cells have been actively studied both in theoretical and experimental.

As part of the this thesis, we study both regular and random arrays of MNPs as additional layers for photovoltaic devices (see final part of the present work).

2 Theoretical foundations

If you have bought one of those T-shirts with Maxwell's equations on the front, you may have to worry about its going out of style, but not about its becoming false. We will go on teaching Maxwellian electrodynamics as long as there are scientists.

(Steven Weinberg)

2.1 Classic electrodynamics

The propagation of light in free space as well as in the presence of single scatterers and complex structures obeys the fundamental laws given by Maxwell's equations (1861, 1862) that constitute a close relationship between the electric field $\mathbf{E}$, the magnetic field $\mathbf{H}$, the displacement current $\mathbf{D}$ and the magnetic induction $\mathbf{B}$. They include that charge ρ and current $\mathbf{j}$ density distributions are the source of electromagnetic fields. We assume harmonic time-dependence $\sim e^{-i\omega t}$ of the fields with frequency ω and use Gaussian units throughout this work, thus that Maxwell's equations read

$$\nabla \times \mathbf{E} = ik\mathbf{H}, \qquad \nabla \times \mathbf{H} = \frac{1}{c}\left(-i\omega\mathbf{D} + 4\pi\mathbf{j}\right), \tag{2.1}$$

$$\nabla\mathbf{B} = 0, \qquad \nabla\mathbf{D} = 4\pi\rho. \tag{2.2}$$

The wave number of the propagating fields is $k = \omega/c = 2\pi/\lambda$, with $c = 299.792.458\,\mathrm{m/s}$ being the velocity of light and λ the corresponding wavelength. The charge density ρ and the current density $\mathbf{j}$ are connected via the continuity equation $\nabla\mathbf{j} = i\omega\rho$ implied by the above set of equations. Another consequence lies in the existance of an electric scalar ϕ and a magnetic vector $\mathbf{A}$ potential constituted by

$$\mathbf{E} = -\nabla\phi + i\frac{\omega}{c}\mathbf{A}, \qquad \mathbf{B} = \nabla \times \mathbf{A}, \tag{2.3}$$

which are useful in the description of electromagnetic fields. In particular, near-field effects, where retardation due to short distances $\mathbf{r}$ (obeying $kr \ll 1$) can be neglected and the electric and magnetic fields decouple, are well described in the electrostatic limit $\mathbf{E} = -\nabla\phi$.

Fields inside solid materials are described by two additional equations, the constitutive relations, connecting the electric vector fields via a material and shape dependent complex

permittivity ϵ and the magnetic vector fields via the permeability μ of a given material.

$$\mathbf{D} = \mathbf{E} + 4\pi\mathbf{P}, \qquad \mathbf{P} = \chi_e\mathbf{E}, \qquad \epsilon = 1 + 4\pi\chi_e, \tag{2.4}$$

$$\mathbf{B} = \mathbf{H} + 4\pi\mathbf{M}, \qquad \mathbf{M} = \chi_m\mathbf{H}, \qquad \mu = 1 + 4\pi\chi_m. \tag{2.5}$$

Here, we introduced the macroscopic polarization $\mathbf{P}$ and the magnetization $\mathbf{M}$ which describe the optical response of the material to an incident electromagnetic field via the susceptibilities χ_e, χ_m and the resulting permittivity ϵ and permeability μ, respectively. In general, both the permittivity ϵ and the permeability μ are second order tensors, containing nonlinear, nonlocal and anisotropic properties of the material. In this work, we concentrate exclusively on nonlocal features of the electron-electron interaction in solids.

Note that eqs. (2.2), the Coulomb law (Gauss law for magnetism) in the absence of free, external charges $\nabla\mathbf{D} = 0$ ($\nabla\mathbf{B} = 0$), yield a linear relation between the fields for a material response that depends solely on frequency

$$\mathbf{D} = \epsilon(\omega)\mathbf{E}, \qquad \mathbf{B} = \mu(\omega)\mathbf{H}. \tag{2.6}$$

In the more general case of a complex position dependence in the permittivity (permeability), the displacement current (magnetic induction) is the solution to the integral expression

$$\mathbf{D} = \int d\mathbf{r}'\epsilon(\mathbf{r}, \mathbf{r}', \omega)\mathbf{E}(\mathbf{r}', \omega), \qquad \mathbf{B} = \int d\mathbf{r}'\mu(\mathbf{r}, \mathbf{r}', \omega)\mathbf{H}(\mathbf{r}', \omega). \tag{2.7}$$

In homogeneous materials the interaction distance is of importance, rather than the explicit position of single electrons, i.e. $\epsilon(\mathbf{r}, \mathbf{r}', \omega) \to \epsilon(\mathbf{r} - \mathbf{r}', \omega)$ and likewise $\mu(\mathbf{r}, \mathbf{r}', \omega) \to \mu(\mathbf{r} - \mathbf{r}', \omega)$, permitting us to write a local solution in reciprocal (Fourier) space

$$\mathbf{D} = \epsilon(\mathbf{k}, \omega)\mathbf{E}(\mathbf{k}, \omega), \qquad \mathbf{B} = \mu(\mathbf{k}, \omega)\mathbf{H}(\mathbf{k}, \omega). \tag{2.8}$$

Local dielectric functions $\epsilon(\omega)$ are effectively used for insulators, resonances from intraband transitions and core polarizations in the bulk material. An accurate description of nonlocal effects in metal nanostructures is given by the complex permittivity $\epsilon(\mathbf{k}, \omega)$ of a material that contains all information of a material's optical response. It becomes important for the understanding of optical phenomena induced by the interacting free electron gas, where the involved evanescent fields are especially sensitive to $\mathbf{k}$-dependent nonlocal effects. We discuss this in more detail in the next section.

The electric and magnetic dipole moments $\mathbf{p}, \mathbf{m}$ of a particle are given as its optical response to an applied electric or magnetic field $\mathbf{p} = \alpha^E\mathbf{E}^{\text{ext}}$ and $\mathbf{m} = \alpha^M\mathbf{H}^{\text{ext}}$. The polarizabilities can be derived analytically from Mie theory[53] for homogeneous spheroidal particles an involve in general higher order multipoles. A fundamental aspect in the optical response of

nanostructures are in this context the optical extinction and scattering cross sections[130]

$$\sigma_{\text{ext}} = 4\pi k \sum_l \text{Im}(\alpha_l^E + \alpha_l^M), \tag{2.9}$$

$$\sigma_{\text{scatt}} = \frac{k^4}{6\pi} \sum_l (|\alpha_l^E|^2 + |\alpha_l^M|^2), \tag{2.10}$$

where $k = \sqrt{\epsilon}\,\omega/c$ is the wave number in the medium and $\alpha_l^E(\alpha_l^M)$ denote the l-th order electric (magnetic) polarizability. Moreover, a scattering matrix t_l^ν ($\nu = \{E, M\}$) for an individual particle can be found by solving usual boundary conditions (introduced in section 2.1.2) for electric and magnetic fields at the surface of a particle. For the lowest order (dipolar) excitation it is connected to the polarizability via[130]

$$\alpha_1^\nu = \frac{3}{2} \frac{1}{k^3 \sqrt{\epsilon_0}} t_1^\nu, \tag{2.11}$$

where ϵ_0 denotes the permittivity of the surrounding medium. From the quasistatic (Rayleigh) limit, it is known that $\alpha_1^E \sim a^3$ and $\alpha_1^M \sim a^5$ for particles of radius a. Indeed, in most metal nanomaterials, the magnetic response can be neglected.

For more complex structures, where the scattering matrix cannot be found analytically, numerical methods such as the boundary element method (BEM)[131,132] offer a feasible way to retrieve the components of the related scattering matrix. From this, optical properties of arbitrarily shaped particles can be investigated.

We derive extended, nonlocal Mie coefficients including both electric and magnetic scattering matrices in section 3.1.2, where we investigate nonlocal response in materials employing the hydrodynamic framework discussed in the next sections.

2.1.1 Optical response of a free electron plasma

Freely moving electrons in a metal crystal lattice undergo collisions with a characteristic rate of $\gamma_p = 1/\tau_{\text{coll}}$. Each electron under the influence of an external electric field with amplitude $\mathbf{E}_0$ obeys thus the equation of motion

$$\frac{d^2}{d_t^2}\mathbf{x} + \gamma_p \frac{d}{d_t}\mathbf{x} = \frac{\mathbf{F}}{m_e} = -\frac{e}{m_e}\mathbf{E}_0 e^{-i\omega t}, \tag{2.12}$$

where the exerted force $\mathbf{F}$ is proportional to the elementary charge $e = 1.609 \times 10^{-19}$ C. The electron position $\mathbf{x}$, solution of eq. (2.12), enters in the macroscopic polarization

$$\mathbf{P} = -en\mathbf{x} = -\frac{e^2}{m_e} \frac{n}{\omega(\omega + i\gamma_p)} \mathbf{E}_0 e^{-i\omega t}, \tag{2.13}$$

where $n = N/V$ is the conduction electron density of the material per unit volume. We find the dielectric function of a metal in Drude approximation from eqs. (2.4)

$$\mathbf{D} = \mathbf{E} + 4\pi\mathbf{P} = \left(1 - \frac{e^2}{m_e}\frac{4\pi n}{\omega(\omega + i\gamma_p)}\right)\mathbf{E}_0 e^{-i\omega t},$$

$$\Rightarrow \epsilon(\omega) = 1 - \frac{e^2}{m_e}\frac{4\pi n}{\omega(\omega + i\gamma_p)} = 1 - \frac{\omega_p^2}{\omega(\omega + i\gamma_p)}, \tag{2.14}$$

and introduce the plasma frequency $\omega_p^2 = 4\pi e^2 n/m_e$. In the tables 6.1 and 6.2, we give an overview of all permittivities and material parameters used in the different parts of this work with their respective sources.

Most reported electromagnetic simulations involving nanostructures rely on the use of local, frequency-dependent dielectric functions,[133] which neglect spatial dispersion and should strictly speaking be reserved for insulators and core-polarization in metals.[134] The Drude model of metals eq. (2.14) can be seen as the $\mathbf{k} \to 0$ limit of the valence electron contribution. A phenomenological extension to include finite size effects is given by an additional damping term accounting for a reduced mean free path length[135] of the electrons $\gamma = \gamma_p + A\frac{v_F}{a}$ in a particle of radius a substituting

$$\epsilon_{\mathrm{loc}}(\omega) \longrightarrow \epsilon_{\mathrm{loc}}(\omega) + \frac{\omega_p^2}{\omega(\omega + i\gamma_p)} - \frac{\omega_p^2}{\omega(\omega + i\gamma_p + A\frac{v_F}{a})}, \tag{2.15}$$

where A is a constant fitting parameter.[136] The metal ionic background is already contained in the measured, local bulk dielectric function $\epsilon_{\mathrm{loc}}(\omega)$. This discription is very limited. It results in reasonable agreement with experiments on nanospheres with respect to plasmon broadening, but it underestimates the blue shift for noble metals noted in the introduction.[137] Delocalized valence electrons exhibit significant $\mathbf{k}$-dependence which is completely neglected in this customary approach.

An advanced material model is given by the Lindhard dielectric function as the result of a perturbation approach exploiting the random phase approximation (RPA).[63,138] It provides an analytical expression for the important case of the free electron gas. This expression was extended by Mermin to include electron–motion damping selfconsistently in $\epsilon_M(\mathbf{k}, \omega)$.[138] It containes a finite damping without net electron loss and the Drude-model is still recovered in the $\mathbf{k} \to 0$ limit. This dielectric function then replaces the local Drude function providing a good description of nonlocal bulk properties

$$\epsilon = \epsilon_{\mathrm{loc}}(\omega) + \epsilon_M(\mathbf{k}, \omega) - \epsilon_D(\omega). \tag{2.16}$$

We exploit this approach in the framework of the specular reflection model (SRM), yielding a first model for nonlocal effects in the nonretarded-limit in section 3.1.1.

Another semi-classical approach towards nonlocality is given by the hydrodynamic model

of the free electron plasma.[139,140] This involves the separation of the dynamics of bound electrons described with a complex background dielectric function $\epsilon_b(\omega)$ from the conduction band electrons of a metal. The background permittivity then arises from interband transitions and is particularly important in noble metals (e.g. $\epsilon_b \approx 9$ for gold, see also appendix 6.1). The continuous bounded electron gas evolves according to the (here linearized) hydrodynamic equation for the induced electron density $\rho^{\text{ind}} = -en$

$$(\partial/\partial t + \gamma_p + \mathbf{v}\cdot\nabla)\, m_e n\mathbf{v} = -\nabla p - en\mathbf{E}, \tag{2.17}$$

where $\mathbf{v}$ is the electron velocity, γ_p is the intrinsic inelastic damping rate, p is the induced hydrodynamic pressure, and $\mathbf{E}$ is the total electric field. The electromagnetic field enters via the Lorentz force density $f = \rho^{\text{ind}}(\mathbf{E} + \frac{\mathbf{v}}{c}\times\mathbf{B})/m_e$ where the second term vanishes on linearizing. We work in the limit of linear response, so that the disturbance in the induced electron density $n - n_0$ is assumed to be small compared with the unperturbed density n_0. Neglecting higher-order terms and focusing on monochromatic components of frequency ω, we find for the related induced current density $\mathbf{j}^{\text{ind}} = \rho^{\text{ind}}\mathbf{v}$

$$\mathbf{j}^{\text{ind}} = \frac{i}{\omega + i\gamma_p}\left(\frac{\omega_p^2}{4\pi}\mathbf{E} - \nabla(\beta^2\rho^{\text{ind}})\right). \tag{2.18}$$

The pressure $p/m_e = \beta^2\rho^{\text{ind}}$ is assumed to be linear in the induced density through the hydrodynamic parameter β, which indicates the strength of nonlocality. A classical calculation of the pressure obtained from the variation of the kinetic energy of a non-interacting electron gas with respect to volume yields[141] $\beta = v_F/\sqrt{3}$, see appendix section 6.2, where the Fermi velocity v_F depends on the unperturbed density n_0 as $v_F = (\hbar/m_e)(3\pi^2 n_0)^{1/3}$. We instead use the value $\beta = v_F\sqrt{3/5}$, which is defining the pressure of a fully degenerated electron gas subject to Coulomb interaction and agrees with the low-momentum dispersion of the Lindhard formula.[142,143] Equation (2.18) has to be solved self-consistently together with the continuity equation and the wave equations for both the electric field and the electron density, which demands an additional boundary condition, derived and discussed in the next section.

2.1.2 Wave equations and boundary conditions

To yield solutions of the optical response of a given structure, wave equations derived from Maxwell's equations (2.1) are solved.

$$\nabla\times\nabla\times\mathbf{E} = ik\nabla\times\mathbf{H} = \frac{ik}{c}\left(-i\omega\epsilon_b\mathbf{E} + 4\pi\mathbf{j}^{\text{ind}}\right),$$
$$\nabla\times\nabla\times\mathbf{E} - k^2\epsilon_b\mathbf{E} = \frac{4\pi ik^2}{\omega}\mathbf{j}^{\text{ind}},$$

which becomes

$$\nabla^2\mathbf{E} + k^2\epsilon_\perp\mathbf{E} = 4\pi\left(\frac{1}{\epsilon_b} - \frac{k^2\beta^2}{\omega(\omega+i\gamma)}\right)\nabla\rho^{\text{ind}}, \tag{2.19}$$

where the transversal dielectric function is defined as $\epsilon_\perp = \epsilon_b - \frac{\omega_p^2}{\omega(\omega+i\gamma_p)}$. It should be noted that, in a homogeneous medium (uniform n_0 and $\epsilon_b(\omega)$), the solution of the above equations in momentum space yields a dielectric displacement $\mathbf{D} = \epsilon_\parallel\mathbf{E}_\parallel + \epsilon_\perp\mathbf{E}_\perp$, in terms of electric field components parallel and perpendicular to the propagation direction $\mathbf{k}$, respectively, where the permittivity for the parallel component is

$$\epsilon_\parallel(k,\omega) = \epsilon_b - \frac{\omega_p^2}{\omega(\omega+i\gamma_p) - \beta^2k^2}. \tag{2.20}$$

A nonlocal correction using a hydrodynamic dielectric function of this type has been widely used to study nonlocal reponse in metal spheres,[54,55,61] shells, nanowires,[64,66,68] triangles,[66,68] waveguides, nanotips[73,144] and its suitability for usage within transformation optics has been demonstrated.[50]

In a nonlocal metal, the electric field couples to the induced current $\mathbf{j}^{\text{ind}}$ and the charge density ρ^{ind}. A fully retarded solution would have to investigate eq. (2.19) which is our starting point to derive nonlocal Mie coefficients in section 3.1.2 as well as Fresnel's equations for nonlocal media in section 3.1.3. However, as we are mostly interested in short-range effects and near-field optical response, we derive the equivalent Poisson's equation for the electric potential by inserting the electrostatic field $\mathbf{E} = -\nabla\phi$ into the Coulomb law. After rearranging, we obtain

$$\nabla^2\phi = -\frac{4\pi}{\epsilon_b}\rho^{\text{ind}}. \tag{2.21}$$

In order to find a solution to the inhomogeneous part constituting an additional driving field due to the free electron dynamics, we derive a wave equation for the conduction band electrons from the divergence of the hydrodynamic equation (2.18) exploiting the continuity

$$\nabla\mathbf{j}^{\text{ind}} = i\omega\rho^{\text{ind}} = \frac{i}{\omega+i\gamma}\left(\frac{\omega_p^2}{4\pi}\nabla\mathbf{E} - \nabla^2(\beta^2\rho^{\text{ind}})\right)$$

which results in

$$\nabla^2\rho^{\text{ind}} = -\frac{\epsilon_\perp}{\epsilon_b}\omega(\omega+i\gamma)/\beta^2\rho^{\text{ind}}. \tag{2.22}$$

This defines additional pressure waves with a longitudinal character that are not found in the

common local approximation. We denote the longitudinal wave vector $\mathbf{q} = (\mathbf{k}_\parallel, \pm q_0)/|\mathbf{q}|$ with

$$q_0^2 = q^2 - k_\parallel^2 \beta^2 = \frac{\epsilon_\perp}{\epsilon_b}\omega(\omega + i\gamma)/\beta^2 - k_\parallel^2 \beta^2, \tag{2.23}$$

where $\mathbf{k}_\parallel = (k_x, k_y)$, which is later on used to describe nonlocal response at planar interfaces. The total nonlocal wave vector reads

$$q = \sqrt{\frac{\epsilon_\perp}{\epsilon_b}\omega(\omega + i\gamma)}/\beta. \tag{2.24}$$

Note that q is also derived from the condition $\epsilon_\parallel(q, \omega) = 0$. In contrast to the local theory, eq. (2.24) predicts a finite extension of the screening charge, which can also be understood as a finite penetration of the induced charges inside the material by a distance approximately given by $1/\mathrm{Im}\{q\}$, which is plotted for gold parameters in Fig. 1.2 and compared to the value found in literature of the electron spill-out of 0.24 nm.[42] The calculated penetration depth reaches a maximum value near the plasmon edge (~ 0.5 nm at $\lambda = 560$ nm) and then goes down to ~ 0.25 nm over the red and near infrared parts of the spectrum. The insets in this figure schematically represent this finite penetration of the surface-induced charge in the nonlocal theory, not accounted for in local descriptions, for which the induced charge is a surface delta function. As a consequence of the electron spill-out, the effective surface from the optical point of view is displaced towards the vacuum with respect to the jellium-edge. This is important to describe molecules in close proximity to a metal surface. *Ab initio* calculations for particle dimers of sizes <2 nm have clearly identified the effect of overlapping density profiles.[44,49] We discuss in section 3.2 the possibility to extend the semi-analytical hydrodynamic approach to describe nonlocal response including smooth electron density profiles modeling realistic metal surfaces.

A general solution to an electric field in a nonlocal structure is then given as a superposition of the solution $\mathbf{E}_0$ (ϕ_0) to the homogeneous wave equation of the transversal electric field (potential) and the solutions ρ^{ind} related to eq. (2.22) in the general form of $\mathbf{E} = \mathbf{E}_0 + \mathbf{B}^E \rho^{\mathrm{ind}}$ and $\phi = \phi_0 + B\rho^{\mathrm{ind}}$. The coefficients can be derived by inserting into eqs. (2.19) and (2.21), respectively, which yield similar expressions

$$\mathbf{B}^E \rho^{\mathrm{ind}} = -\frac{4\pi}{\epsilon_\perp \omega(\omega + i\gamma)} \nabla(\beta^2 \rho^{\mathrm{ind}}), \qquad B = \frac{4\pi\beta^2}{\epsilon_\perp \omega(\omega + i\gamma)}. \tag{2.25}$$

Finally, to find the optical response of individual geometries, which we discuss in the next chapters, boundary conditions are needed to describe the evolution of the fields from different regions in space. For bounded media, $\epsilon_b(\omega)$ is customarily chosen to be confined within a region extending half an inter-atomic plane beyond the outer-most plane.[43] This adds a sharp dielectric background edge, which requires imposing the continuity of $\mathbf{E}_\parallel, (\phi)$ and $\epsilon_b \mathbf{E}_\perp, (\epsilon_b \partial_\perp \phi$, where $\partial_\perp$ denotes the normal derivative) in order to avoid unphysical divergences in eqs. (2.19) and (2.21), respectively. These are the usual boundary conditions imposed by Maxwell's equations already in the local approximation. The important aspect

here is the necessity of an additional boundary condition to accompany the hydrodynamic equation. Equation (2.18) imposes the continuity of the pressure $\beta^2\rho^{\text{ind}}$, whereas the continuity equation demands the continuious connection of the current $\mathbf{j}^{\text{ind}}$ itself at each boundary. This means, for any sharp metal-to-dielectric interface $\mathbf{j}_\perp^{\text{ind}} = 0$, since no current density due to free electrons is found in the dielectric medium. The current is not trespassing the boundaries and we assume that no induced charge singularities are present. Evaluating the boundary conditions for each interface in a structure allows us to calculate the optical coefficients in that system.

2.1.3 Local density of optical states

In photonics, the local density of optical states (LDOS) is a space-resolved measure of quantum states that can be occupied by a photon. From the LDOS, we can deduce the spontaneous emission rate of a closeby scatterer, e. g. a molecule or a quantum dot. In practice, it can be measured by fluorescence, near-field scanning or cathodoluminescence techniques. Theory places a probe emitter at a desired position and calculates induced fields to estimate the LDOS of a structure.

Here, we place a dipole emitter close to a metal surface and investigate the induced electric potential. This leads straightforwardly to the corresponding reflection coefficients for geometries with sharp interfaces, shown in appendix 6.4 for nonlocal material response, with the local limit found by setting $k_\parallel \to 0$. A general expression for the LDOS induced by a dipole moment $\mathbf{d}$ is given by[145]

$$\Gamma = \frac{2}{\hbar}\text{Im}\{\mathbf{E}\mathbf{d}^*\} + \Gamma^0,$$

where the free space LDOS Γ^0 is given by

$$\Gamma^0 = \frac{4\pi^2\omega|\mathbf{d}|^2}{\hbar}\rho^0, \quad \text{and} \quad \rho^0 = \frac{\omega^2}{3\pi^2c^3}, \tag{2.26}$$

which results in an expression for the induced part of the LDOS

$$\Gamma - \Gamma^0 = \frac{4\pi^2\omega|\mathbf{d}|^2}{\hbar}\rho_{\text{ind}}^{\text{LDOS}}.$$

When investigating planar structures, it is convenient to align a unit dipole along the z direction, i. e. $\mathbf{d} = \hat{\mathbf{z}}$ and $|\mathbf{d}| \equiv 1$. Furthermore, we develop $\rho_{\text{ind}}^{\text{LDOS}}$ into components of parallel momentum, which allows us to study $k_\parallel$-resolved (dispersion) spectra

$$\rho_{\text{ind}}^{\text{LDOS}} = \int d^2k_\parallel \rho_{k_\parallel}(\omega) = 2\pi \int_0^\infty dk_\parallel k_\parallel \rho_{k_\parallel}(\omega),$$

which in planar geometries results in

$$\rho_{k_\parallel}(\omega) = \frac{1}{2\pi^2\omega}\mathrm{Im}\{E_z^{\mathrm{ind}}(\mathbf{k}_\parallel,\omega)\} = \frac{1}{2\pi^2\omega}\mathrm{Im}\{-\partial_z\phi^{\mathrm{ind}}(\mathbf{k}_\parallel,\omega)\}. \tag{2.27}$$

Hereby, the dependence on $\mathbf{k}_\parallel$ in the electric potential is only explicit for the case of nonlocal material properties, for instance compare with appendix 6.4. This approach to investigate the optical response is exploited in section 3.2, where we discuss the impact of nonlocality and the employment of smooth interfaces in detail.

2.2 Collective excitations at metal surfaces

The unique properties of metal nanostructures and the increasing ability to fabricate particles and structures with nanoscale resolution has made the design and characterization of a wide range of nanostructured materials an attractive field to achieve new solutions towards total light control. Light can be confined within volumes hundreds of times smaller than the free-space wavelength by using the excitation of surface plasmons in metallic structures.

Confinement in nanostructures is used in the creation, guidance and processing of light and electron waves. Nanoplasmonics allows converting photon energy and momentum into electronic signals and vice versa, thus enabling the generation and routing of signals on the nanoscale. On the other hand, plasmonics is exploited to yield strong local field enhancements and increased absorption of light to enhance energy conversion in light harvesting devices or improve the signal-to-noise ratio in sensing and detection applications.

The interaction between an incident light field and the electron gas of a metal can lead to interesting interface induced effects, in particular, to the formation of different kinds of plasmons. These collective electron plasma oscillations lead to a trapped electromagnetic surface mode with fastly decaying normal components. This mode confinement yields high local fields limited to the proximity of the surface. Enhancement effects due to improved light-matter interaction mediated by plasmonic excitations open up many opportunities for applications in nano-optics, as discussed in the introductory section 1, and nonlinear optics, such as light controlled second harmonic generation.

In general, the bulk or volume plasmon given by the plasma frequency ω_p is shifted towards lower energies from typically UV energies to the VIS for light confined in finite metal nanostructures.

2.2.1 Surface plasmon polaritons

Surface plasmons are guided electromagnetic waves confined at the interface between a metal and a dielectric, which originate from collective interaction of light and free conduction electrons. At planar interfaces these waves are polarized and delocalized along the propagation

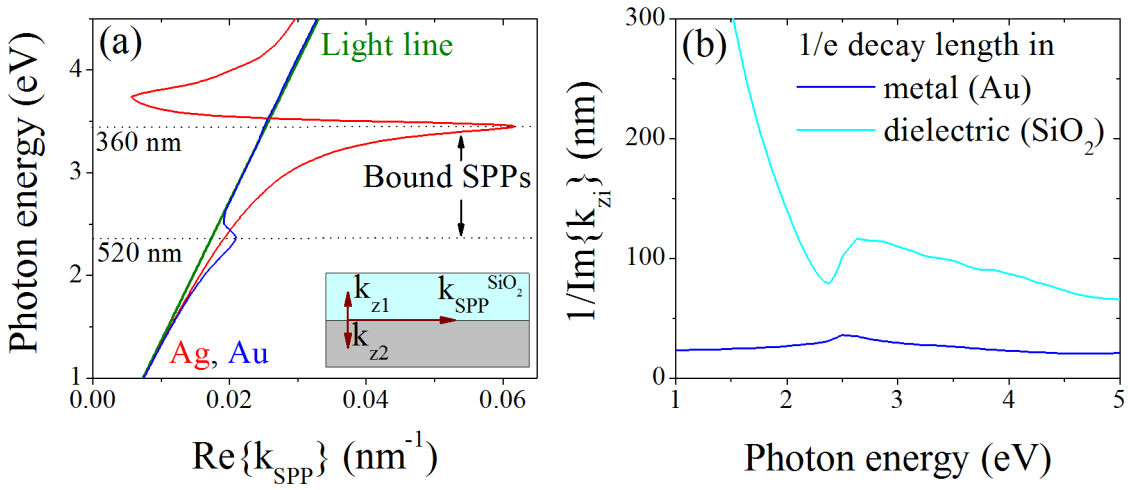

Fig. 2.1: **Fundamental optical properties of surface plasmon polaritons.** (a) Dispersion law for surface plasmon polaritons for gold and silver[146] on SiO_2 ($\epsilon_2 = 2.1$). The inset depicts the planar structure investigated and the components of the wave vectors. (b) Amplitude decay length to $1/e$ for the evanescent electric fields normal to the interface.

direction. Surface plasmon polaritons (SPPs) obey the dispersion law $k_{\mathrm{SPP}} = \frac{\omega}{c}\sqrt{\frac{\epsilon_1\epsilon_2}{\epsilon_1+\epsilon_2}}$, at an interface separating two media of permittivity ϵ_1 (metal) and ϵ_2 (dielectric), respectively. This yields solutions propagating along the interface for $\epsilon_1\epsilon_2 < 0$, while $|\epsilon_1| > \epsilon_2$, which is achieved by many metals in the VIS or NIR spectral regions. The dispersion relation is shown in Fig. 2.1 (a) for gold and silver[146] with realistic damping parameters. For frequencies below the material dependent surface plasmon resonance $\omega_{\mathrm{SPP}} = \frac{\omega_p}{\sqrt{\mathrm{Re}\{\epsilon_b\}+\epsilon_2}}$, determined by the condition $\epsilon_1 + \epsilon_2 \equiv 0$, the momentum k_{SPP} lies always below the light line indicating the bound character of these modes. The inverse of the wave vectors for the normal components $k_{zi} = \frac{\omega}{c}\sqrt{\frac{\epsilon_i^2}{\epsilon_1+\epsilon_2}}$, where $i = \{1, 2\}$ gives a measure for the penetration or skin depth in the metal and dielectric semi-infinite media. Fig. 2.1 (b) depicts this for a gold - SiO_2 interface. Note, that the mode confinement inside the metal is much stronger than towards the dielectric side.

Coupling plasmons from two planar surfaces, either in a finite metal slab or in a metal-dielectric-metal structure, results in the splitting of the surface plasmon polariton (SPP) into a symmetric and an assymmetric mode that are associated to the SPPs at the opposite surfaces. In the limit of large film and gap thicknesses, we again observe the SPP for a single interface due to the short-range mode extension normal to the surface.

2.2.2 Localized surface plasmons

In contrast, nanoparticles, corrugated metals and edges generate optical fields confined in all three dimensions: the localized surface plasmons (LSPs). The spectral response of LSPs can be controlled and tuned by engineering the shape and size of the nanoparticles, as well as the

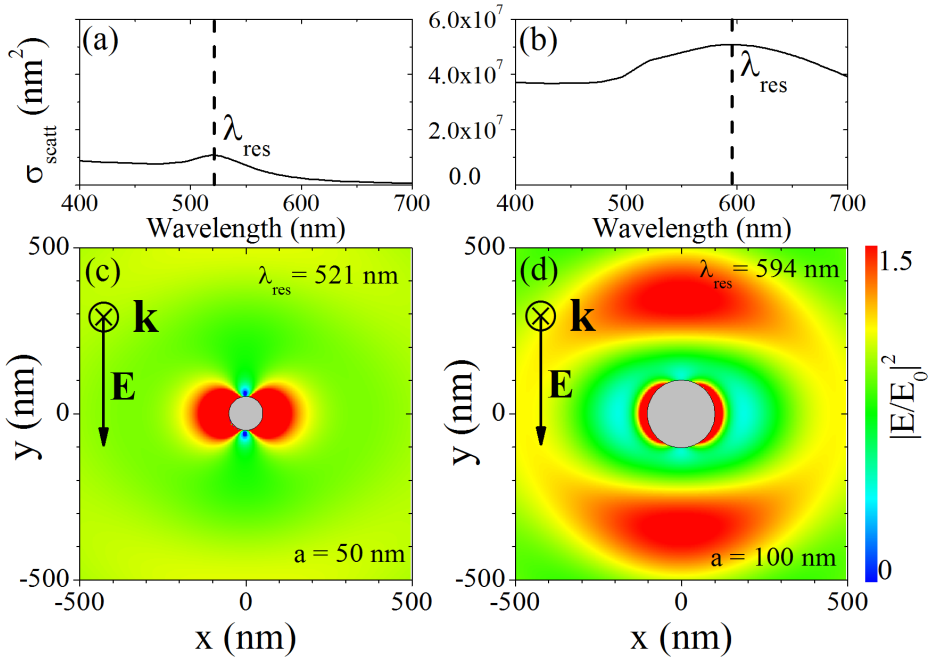

Fig. 2.2: **Fundamental optical properties of metal nanoparticles, near-field enhancement.** For two gold particle radii (a), (c) $a = 50\,\text{nm}$ and (b), (d) $a = 100\,\text{nm}$, we show (a), (b) radiation scattering spectra and (c), (d) near-field calculations at the localized plasmon resonance.

material parameters of the surrounding structure. In Fig. 2.2 the radiation scattering σ_{scatt}, eq. (2.9), is presented for two particle sizes. At the corresponding localized surface plasmon resonance (LSPR), the normalized near-field intensity $|\mathbf{E}/\mathbf{E}_0|^2$ is calculated to demonstrate the dipolar pattern observed at short distances relative to the nanoparticle surface. At larger distances an interference pattern is observed. The typical increase of the LSPR with particle size can be used to fabricate nanoparticles with predetermined spectral features, cp. Fig. 1.1 (a).

The formation of hot-spots, i. e. strongly localized fields, at edges or in small gaps between particles is of special interest in e. g. medical imaging and enhancement of photoluminescence and fluorescence in light emitting diodes. Layers of regularly or randomly distributed metal nanoparticles are exploited for large-scale enhancement effects in biological sensors, for SERS and light harvesting devices in photovoltaics and photocatalytics.

2.2.3 Plasmonic excitations in particle arrays

An important aspect in the optical response of metal nanoparticles is the large optical cross section that they feature. An incoming electric field bends towards the nanoparticle, as shown in Fig. 2.3 (a). This effect can be optimized to produce total field absorption. Particle arrays are a great candidate to achieve this goal. In Fig. 2.3 (b), we extract from the optical cross section, eq. (2.9), a corresponding lattice parameter b that yields maximum absorption

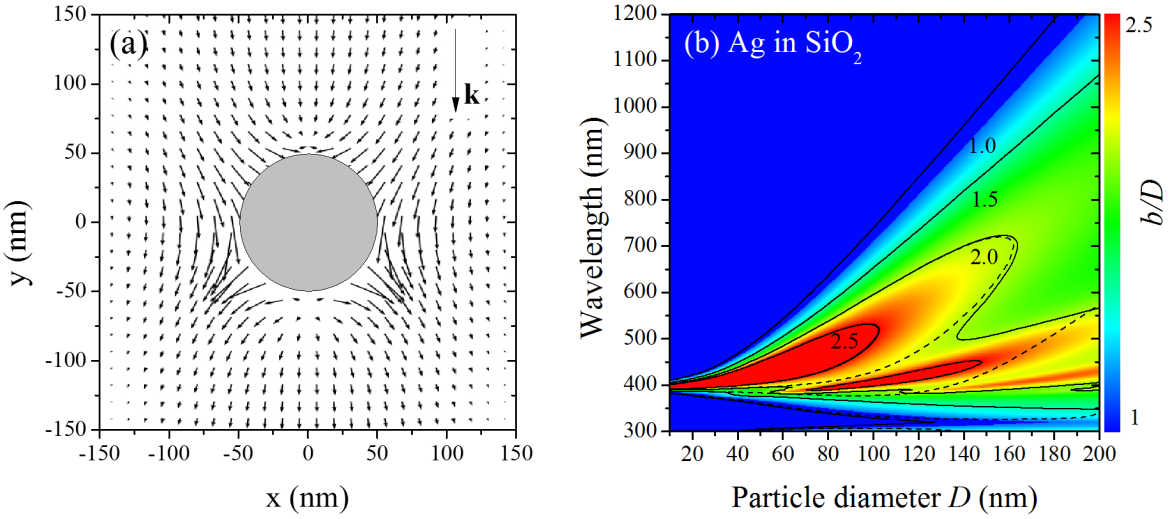

Fig. 2.3: **Fundamental optical properties of metal nanoparticles, absorption.** (a) In-plane electric field distribution around a gold nanoparticle of $a = 50\,\mathrm{nm}$ and (b) scattering cross section for a Ag particle in SiO_2 in terms of an effective lattice parameter $b/D = b/(2a)$ for a hexagonal Ag lattice. We depict contour plots for analytical (dipolar, dashed) and numerical (multipolar, $l_{\max} = 10$, solid) calculations. Strong absorption is expected for spectral regions where $b/D > 1$.

for spherical particles with diameter D by comparing to the geometrical cross section for a hexagonal lattice $\sigma_{\mathrm{geo}} = \frac{\sqrt{3}}{2} b^2$. In spectral regions where the effective lattice parameter $b/D > 1$, the plasmonic excitations in a related particle array would yield total absorption with physically realizable systems.

The optical response of regular arrays of nanoparticles can be calculated from different methods, exploiting the symmetries in the system.[145,147] In chapter 4, we rely on numerical methods such as the layer-Korringa-Kohn-Rostoker method (KKR),[132,148–150] and multiple scattering theory[132] which is also exploited for randomly distributed particle arrays. For the latter, we derive and exploit analytical expressions for the scattering matrices of nanoparticles as indicated in eq. (2.11).

To obtain simple analytical expressions, we employ the self-consistent description of the electric and magnetic dipole moments $\mathbf{p}, \mathbf{m}$ given by the polarizability of each single particle and the total field, consisting of the external field plus the scattered field. The scattered field includes the back-action of the surrounding particles arising from their electric and – where aplicable – magnetic contributions. In this way, each particle contributes to the optical properties of the whole array

$$\mathbf{p} = \alpha^E \mathbf{E}^{\mathrm{tot}} = \alpha^E (\mathbf{E}^{\mathrm{ext}} + \mathbf{E}^{\mathrm{scat}}) = \alpha^E (\mathbf{E}^{\mathrm{ext}} + G^{\mathrm{EE}}\mathbf{p} + G^{\mathrm{EM}}\mathbf{m}), \tag{2.28}$$

$$\mathbf{m} = \alpha^M \mathbf{H}^{\mathrm{tot}} = \alpha^M (\mathbf{H}^{\mathrm{ext}} + \mathbf{H}^{\mathrm{scat}}) = \alpha^M (\mathbf{H}^{\mathrm{ext}} + G^{\mathrm{MM}}\mathbf{m} + G^{\mathrm{ME}}\mathbf{p}). \tag{2.29}$$

For particles with negligible magnetic response, this reduces to the convenient form

$$\mathbf{p} = \alpha^E \mathbf{E} = \alpha^E (\mathbf{E}^{\text{ext}} + G^{\text{EE}} \mathbf{p}) \qquad \Rightarrow \qquad \mathbf{p} = \frac{1}{1/\alpha^E - G^{\text{EE}}} \mathbf{E}^{ext}. \tag{2.30}$$

Hereby, the electromagnetic Green's tensor

$$G = \begin{pmatrix} G^{\text{EE}} & G^{\text{EM}} \\ G^{\text{ME}} & G^{\text{MM}} \end{pmatrix} \tag{2.31}$$

describes the dipole-dipole interaction and aforementioned back-action of all other dipoles. For a monolayer of particles, we can assume $\mathbf{p}_j, \mathbf{m}_j \sim e^{i\mathbf{k}_\parallel \mathbf{R}_j}$ as a consequence of the Bloch theorem, where $k_\parallel = (k_x, k_y)$ is the in-plane wave vector, with the particles being placed at positions $\mathbf{R}_j$ in the $x-y-$plane. The diagonal entries of the Green's tensor are defined by the wave equation for the electromagnetic field

$$G^{\text{EE}} = G^{\text{MM}} = \left(\mathcal{I} k^2 + \nabla \cdot \nabla \right) \frac{e^{ikr}}{r} \tag{2.32}$$

and the off-diagonal terms are found via evaluating

$$G^{\text{EM}} = -G^{\text{ME}} = (-ik\nabla\times) \frac{e^{ikr}}{r}. \tag{2.33}$$

Note that symmetry dictates $G^{\text{EE}} = G^{\text{MM}}$ and $G^{\text{ME}} = -G^{\text{EM}}$.

It is possible to partially evaluate the entries of G in terms of analytical expressions for low multipole orders.[145,147] This is a versatile approach that we exploit later on for both regular and irregular particle arrays, accouting also for magnetic contributions. For random particle arrays, the optical properties of a large sheet of particles is calculated with multiple scattering theory and afterwards the approach discussed above allows studying a regular array of this random area used as a supercell.

3 Part I - Nonlocal effects

> By convention there is colour, by convention sweetness, by convention bitterness, but in reality there are atoms and space.
>
> *(Democritus, 400 BC)*

Experimental access to particle sizes and interparticle spacings below 10 nm is currently available for metallic dimers,[80,151] tips and nanostars,[152] and shell structures,[153,154] in which spatial dispersion (nonlocality) in the materials response is known to play an important role.[36,155] However, most electromagnetic calculations of metal nanostructures rely on local, frequency-dependent dielectric functions,[133] sometimes incorporating the phenomenological damping of eq. (2.15) to account for finite-size effects.[135]

Ab initio methods, such as DFT and (TD)LDA[43–47,49,156] allow for an acurate description of the electron density in nanoparticles. Due to the vast computational effort involved, semi-classical theories towards a description of nonlocal effects are of great importance.

In recent years, a great effort has been made to theoretically[4,7,49,50,54–74,77,78,157–159] describe and subsequently to experimentally[79–81] verify the effect of spatial dispersion in metals. Hereby, it is important to note that in any experimental situation no difference can be made between nonlocal bulk and edge effects, as both phenomena are complement in nanostructures. However, a theoretical approach allows distinguishing different contributions arising from nonlocal properties of the uniform free electron density in the bulk and, separately, including the electron spill-out.

In this chapter, our work related to nonlocal effects is presented and we discuss in particular the following topics.

3.1.1 We briefly introduce the specular reflection model (SRM)[7,63] as a non-retarded approach to nonlocality relying on the k-dependent Mermin dielectric function.[138]

3.1.2 Extended Mie scattering coefficients for metal spheres and nanoshells are derived using the hydrodynamic model for the electron gas.[139,140] This includes retardation effects and we perform the non-retarded limit to directly compare the obtained expressions of nonlocal permittivies in this limit with the SRM.[7]

3.1.3 The nonlocal analogue to Fresnel's coefficients are shown. The presence of additional pressure waves results in supplementary optical coefficients for the longitudinal contributions arising from nonlocal properties.[6]

3.2.1 Including the electron spill-out, we derive a transfer matrix approach to describe smooth surfaces in terms of realistic electron density profiles. These profiles are taken from

original DFT results. Here, we discuss a variety of planar structures.[1,42]

3.2.3 We show that this approach is able to describe smooth surfaces using local material parameters independently of nonlocal interactions in the electron gas.[1]

3.2.4 The introduced framework is extended to account for the local density of optical states (LDOS) placing a probe emitter close to a smooth metal surface.[1]

An accurate description of nonlocal properties of metal nanostructures is important to predict the optical response of molecules in close proximity to metal surfaces, resulting field enhancements and its impact on nonlinear effects.

3.1 Nonlocal bulk effects

Here, we discuss two different approaches to account for bulk nonlocality in metal nanostructures: (i) the non-retarded specular reflection model (SRM),[63,160] where we incorporate the nonlocal Mermin dielectric function,[138] and (ii) the retarded hydrodynamic model.[139,140] We present results that go beyond existing material models by incorporating microscopic elements of the nonlocal response in combination with a reliable description of macroscopic retardation. We derive an analytical solution for the response of spheres incorporating nonlocal effects that constitutes an extension of the well-known Mie theory.[53] This allows us to study nonlocality in metal nanospheres, dimers and nanoshells. Both semi-classical theories are compared in the non-retarded limit. A wide range of geometrical parameters for which nonlocal effects coexist with significant retardation are found.

3.1.1 Specular reflection model

The specular reflection model (SRM) or semiclassical infinite barrier model (SCIB) solves the electric potential within a homogeneous medium in the presence of external charges. Auxiliary boundary charges $\sigma^{\pm}$ are defined on either side of the interface to guarantee the boundary conditions. In a first step, an expression for the boundary charge distribution $\sigma(\mathbf{r})$ and the induced potential[55,59] is seeked. In the quasistatic limit

$$4\pi\sigma(\mathbf{r}) = \nabla\mathbf{D}(\mathbf{r},t) = -\int_{-\infty}^{\infty} \mathrm{d}^3\mathrm{r}'\, \epsilon(\mathbf{r}-\mathbf{r}',t)\nabla^2\phi_{\mathrm{ind}}(\mathbf{r}',t),$$

which in Fourier space yields

$$\hat{\phi}_{\mathrm{ind}}(k,\omega) = \frac{4\pi\hat{\sigma}(\mathbf{k})}{k^2\epsilon(\mathbf{k},\omega)}. \tag{3.1}$$

The solution of the electric potential in real space is then obtained from eq. (3.1). The permittivity used has to be specified. At this stage, any theory for $\epsilon(\mathbf{k},\omega)$ can be used, including,

of course, local theories. We employ Mermin's dielectric function[63,138,140] as introduced in the previous chapter.

Spherical particle in the SRM

For a spherical particle of radius a, an expansion of the boundary charge into spherical functions $Y_L(\Omega)$ in real space with the short notation $j_L(kr) = j_{lm}(kr) = j_l(kr)i^l Y_L(\Omega)$ for the involved Bessel functions[130,161]

$$\sigma(\mathbf{r}) = \frac{1}{a^2}\sum_L \sigma_l Y_L(\Omega)\delta(r-a), \tag{3.2}$$

summing over the orbital momentum numbers l and $m \in \{-l, l\}$ in $L = \{l, m\}$. The exponential function expanded in spherical Bessel functions $j_l(kr)$ is

$$e^{-i\mathbf{kr}} = 4\pi\sum_L j_L(kr)Y_L(\Omega_k). \tag{3.3}$$

With this we find using the properties of Legendre functions[130]

$$\hat{\sigma}(\mathbf{k})_{\text{ind}} = 4\pi\sum_L \sigma_l Y_L(\Omega_k)(-i)^l j_l(ka). \tag{3.4}$$

Finally, we can write the potentials inside (II) and outside (I) the spherical particle

$$\phi_I = \sum_L \left(r^l - \frac{\alpha_l^E}{r^{l+1}}\right) Y_L = \sum_L r^l Y_L + 8\sum_L \sigma_l^+ Y_L(\Omega)\int_0^\infty dk \frac{j_l(kr)j_l(ka)}{\epsilon_0} \tag{3.5}$$

$$\phi_{II} = \sum_L A_l r^l Y_L = 8\sum_L \sigma_l^- Y_L(\Omega)\int_0^\infty dk \frac{j_l(kr)j_l(ka)}{\epsilon(\mathbf{k},\omega)} \tag{3.6}$$

For the local permittivity in the surrounding medium (I), the integral reduces to

$$\frac{1}{\epsilon_0}\int_0^\infty dk j_l(kr)j_l(ka) \overset{r\to a}{=} \frac{\pi}{2}\frac{1}{2l+1}\frac{1}{a}\frac{1}{\epsilon_0}, \tag{3.7}$$

while the integral depending on $\epsilon(\mathbf{k},\omega)$ needs to be evaluated numerically. Using the boundary conditions for a sphere, the continuity of both ϕ and $\epsilon\frac{\partial}{\partial r}\phi$, we find an expression for the nonlocal multipolar polarizability from eq. (3.5)

$$\alpha_l^E = -\frac{4\pi\sigma_l^+}{2l+1}a^l = a^{2l+1}\frac{l(\epsilon_l - \epsilon_0)}{(l+1)\epsilon_0 + l\epsilon_l} \tag{3.8}$$

similar to the local description with a modified dielectric function ϵ_l defined as[63]

$$[\epsilon_l]^{-1} = \frac{2a(2l+1)}{\pi}\int_0^\infty \frac{dk}{\epsilon(\mathbf{k},\omega)} j_l^2(ka). \tag{3.9}$$

The polarizability of a local spherical particle[130] is recovered for vanishing **k**-dependence, where $\epsilon_l \to \epsilon(\omega)$.

Planar geometries in the SRM

For a planar interface at position z_0 and with surface normal along the z-direction the induced boundary charge reads

$$\sigma(\mathbf{r}) = \delta(z - z_0)e^{i\mathbf{Q}_0\mathbf{R}}, \tag{3.10}$$

where $\mathbf{Q}_0$ is the in-plane wave vector with components in the boundary surface. We then find via Fourier transform

$$\hat{\sigma}(\mathbf{k}) = (2\pi)^2\delta(\mathbf{Q} - \mathbf{Q}_0)e^{-ik_z z_0}, \tag{3.11}$$

so that the induced potential resulting from eq. (3.1) becomes

$$\hat{\phi}_{\text{ind}} = 2e^{i\mathbf{Q}_0\mathbf{R}}\int_0^\infty dk_z \frac{e^{ik_z(z-z_0)}}{(k_z^2 + Q_0^2)\epsilon(\sqrt{k_z^2 + Q_0^2}, \omega)} \overset{\text{local}}{\to} 2e^{i\mathbf{Q}_0\mathbf{R}}\frac{\pi}{Q_0}\frac{e^{-iQ_0|z-z_0|}}{\epsilon(\omega)}. \tag{3.12}$$

Solving the equations obtained from the boundary conditions and defining – similar to the case for spherical geometry – the effective dielectric function

$$[\epsilon_s]^{-1} = \frac{Q_0}{\pi}\int_0^\infty dk_z \frac{e^{ik_z(z-z_0)}}{k^2\epsilon(k,\omega)}, \tag{3.13}$$

we obtain for the reflected (+) and transmitted (-) optical coefficients

$$\sigma^+ = \frac{\epsilon_0\epsilon_s - 1}{\epsilon_0\epsilon_s + 1}, \qquad \sigma^- = \frac{2\epsilon_0\epsilon_s}{\epsilon_0\epsilon_s + 1}. \tag{3.14}$$

This allows us to study the impact of nonlocality in non-retarded planar structures.[63]

Evaluation procedure

In the multiple elastic scattering of the multipole expansion (MESME) approach[132] the electric potential is governed by a scattering matrix t_l^E. The scattering properties of a cluster of arbitrary dielectric objects are reduced to the scattering by a single object and multiple elastic scattering between the components is carried out until convergence is achieved. The electromagnetic field is decomposed into multipoles and combined with the iterative multiple-scattering technique. This approach can be used for arbitrarly shaped objects for which the scattering matrices can be found numerically.

For spherical symmetries, the total field has to be a combination of planar partial incoming and outgoing waves, described by spherical Bessel and Hankel functions, respectively.[130,161]

Thus, they have to take the form

$$\phi = j_L(kr) + \sum_L t_l^E h_l^+(kr) i^l Y_L(\Omega) \tag{3.15}$$

outside the particle, which becomes in the non-retarded limit[130]

$$\phi = \left(\frac{(kr)^l}{(2l+1)!!} + t_l^E \frac{(2l-1)!!}{(kr)^{l+1}} \right) i^l Y_L(\Omega). \tag{3.16}$$

Comparing with the expression for the polarizablity eq. (3.5), we find the non-retarded scattering matrix from the polarizability as

$$t_l^E = \frac{l+1}{l} \frac{k^{2l+1}}{(2l+1)!!(2l-1)!!} \alpha_l. \tag{3.17}$$

Although retardation is incorporated in this formalism to describe the interaction between different particles (notice the k factors in t_l^E), the response of each particle is obtained in the electrostatic limit. The polarizability can be choosen to be local or nonlocal and is used in the next section to compare with results from the hydrodynamic model.

3.1.2 Mie scattering coefficients in the hydrodynamic model

We present a derivation of the nonlocal Mie scattering coefficients of individual spheres and nanoshells described with the hydrodynamic model. The resulting scattering matrices are used to investigate interacting spheres with the multiple scattering method discussed previously. Below we discuss that the blue shift and dramatic broadening observed in the plasmon bands of <10 nm noble metal particles are a manifestation of nonlocality, as already pointed out for spheres,[58] cylinders,[69] shells,[46,59] and dimers.[66] Note that our calculations are parameter-free, in which the nonlocal aspects of the metal response for the short distances involved in the interaction between the charges induced in small particles becomes the source of these effects, in contrast to the quantum-confinement picture.

The derivation of the nonlocal MIE coefficients for spherical geometries is based on eq. (2.19) which describes the evolution of the electric field, together with eq. (2.22), which is the wave equation for the induced charge. We abbreviate $4\pi\left(\frac{1}{\epsilon_b} - \frac{k^2\beta^2}{\omega(\omega+i\gamma)}\right) \equiv \eta$.

It is convenient to use an expansion of the electric field into scalar functions[162] as

$$\mathbf{E} = (1/k)\nabla\psi^L + \mathbf{L}\psi^M + \frac{\nabla \times \mathbf{L}}{ki}\psi^E, \tag{3.18}$$

where $\mathbf{L} = -i\hbar\mathbf{r} \times \nabla$ is the angular momentum operator, and the superscripts E, M, and L indicate electric, magnetic, and longitudinal components, respectively. The additional

boundary condition, eq. (2.18), becomes with $\hat{\mathbf{r}}\mathbf{j} = 0$

$$\beta^2 \frac{\partial}{\partial r}\rho^{\mathrm{ind}} = \frac{e^2 n_0}{m_e k}\left(\frac{\partial}{\partial r}\psi^L + \frac{1}{r}l(l+1)\psi^E\right) \tag{3.19}$$

in terms of the scalar functions and the angular momentum number l using the identity $-\mathbf{r}\cdot(\nabla\times\mathbf{L}) = (-i\mathbf{r}\times\nabla)\cdot\mathbf{L} = L^2 = l(l+1)$. The boundary conditions for the electric and magnetic field components result in the continuity of ψ^M, $(1 + r\frac{\partial}{\partial r})\psi^M$, $\psi^L + (1 + r\frac{\partial}{\partial r})\psi^E$, and $\epsilon\psi^E$ for the scalar functions.

The magnetic and electric scalar functions ψ^ν ($\nu = \{E, M\}$) obey a Helmholtz equation of the form $(\nabla^2 + k^2\epsilon_\perp)\psi^\nu = 0$ and can therefore be expanded in terms of spherical Bessel functions

$$\psi^\nu = \sum_L \psi^\nu_L j_L(k_\perp r).$$

Similarly, the electron density is expanded into

$$\rho^{\mathrm{ind}}(\mathbf{r},\omega) = \sum_L \rho_L j_L(qr),$$

with the longitudinal wave vector q given by eq. (2.24). The longitudinal scalar function satisfies a different wave equation, namely $\nabla^2\psi^L = -(4\pi k/\epsilon_b)$, which we find from the Coulomb law $\nabla\epsilon_b\mathbf{E} = -4\pi\rho^{\mathrm{ind}}$. Alternatively, we deduce from the wave equation (2.19)

$$\psi^L = \left(\frac{\eta k}{k_\perp^2 - q^2}\right)\rho^{\mathrm{ind}} = -\frac{4\pi k}{\epsilon_b q^2}\rho^{\mathrm{ind}}. \tag{3.20}$$

The above analysis is useful inside the metal. Outside the particle, we can safely set the longitudinal scalar function to zero because there are no induced charges. In that region, we only need to consider electric and magnetic components. The scattering coefficients t_l^ν fully contain the optical response of the particle for an external observer and are derived for spherical nanoparticles and nanoshells in appendix section 6.3. Note, that for all geometries, the magnetic scattering matrix is unchanged with respect to the local theory, indicating that magnetic modes are not sensitive to the nonlocal effects. The additional longitudinal modes enter, however, in the resulting electric scattering matrices.

The scattering matrix for the electric scalar function is more complicated than in the local approximation due to the appearance of ψ^L in the metal region that contains information on the nonlocal response. The local scattering matrix is extended by a nonlocal parameter

$$g_l = \frac{l(l+1)j_l(\theta_\perp)j_l(qa)}{qaj_l'(qa)}\left(\frac{\epsilon_\perp}{\epsilon_b} - 1\right) \tag{3.21}$$

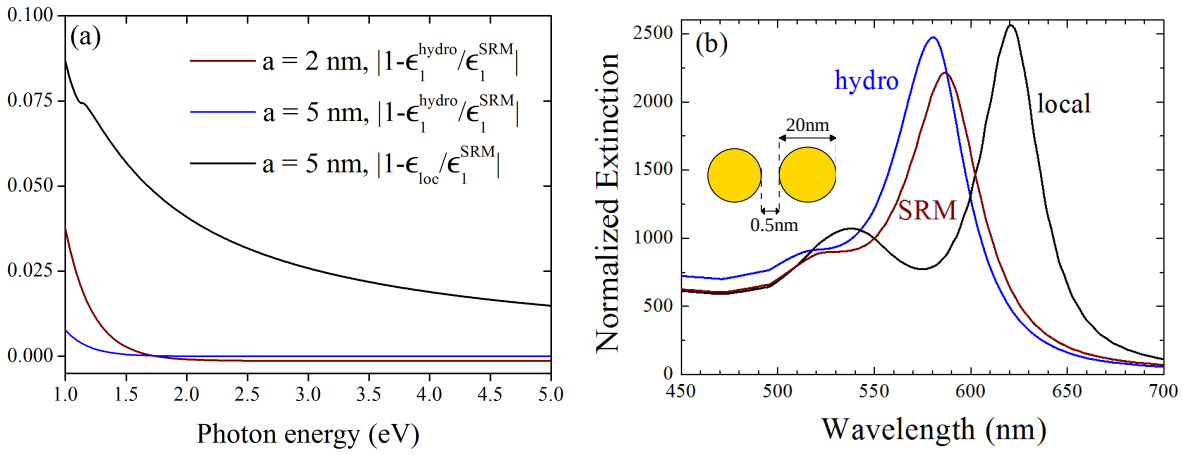

Fig. 3.1: **Comparison of nonlocal semi-classical models in the non-retarded limit.** Relative difference in ϵ_l calculated with the specular-reflection model, the hydrodynamic model, or the local theory for $l = 1$ in gold spheres of different radii. (b) Extinction spectra for a dimer formed by two 20 nm gold spheres separated by 0.5 nm and immersed in water. The external field is normal to the gap. Local and nonlocal calculations are compared. The latter are performed with (hydro) and without (SRM) inclusion of retardation.

and becomes with $\theta_0 = ka\sqrt{\epsilon_0}$ and $\theta_\perp = ka\sqrt{\epsilon_\perp}$

$$t_l^E = \frac{-\epsilon_\perp j_l(\theta_\perp)[\theta_0 j_l(\theta_0)]' + \epsilon_0 j_l(\theta_0)([\theta_\perp j_l(\theta_\perp)]' + g_l)}{\epsilon_\perp j_l(\theta_\perp)[\theta_0 h_l^+(\theta_0)]' - \epsilon_0 h_l^+(\theta_0)([\theta_\perp j_l(\theta_\perp)]' + g_l)}, \tag{3.22}$$

where the primes indicate differentiation with respect to the θ variables.

Note that the nonlocal parameter vanishes under the assumption of local response ($\beta \to 0 \Rightarrow g_l \to 0$) fully recovering the original Mie coefficients.[53,130] This allows us to study nanoparticles with only a small correction in available numerical procedures.

Likewise, for a nonlocal metal nanoshell the magnetic response is insensitive to the nonlocal properties of the material, see appendix 6.3. The electric part, however, mixes with the longitudinal components from the two interfaces of the metal intermediate layer. For the magnetic (electric) scalar functions, we obtain a linear system of four (six) equations that we solve with linear algebra in practice.

Comparison of nonlocal semi-classical models

We are interested in examining what differences there are in the description of nonlocal effects between the specular-reflection model and the hydrodynamic approach. Since the former is obtained from the non-retarded limit, we have chosen to take the $c \to \infty$ limit in the hydrodynamic scattering coefficients, in particular eq. (3.22), for the sake of comparison. In this limit, the magnetic coefficient vanishes, whereas we find for the electric one the polarizability

for a single nanosphere in the same form as eq. (3.8) substituting the expression for ϵ_l with

$$\epsilon_l^{\text{hydro}} = \frac{\epsilon_\perp}{1 + g_l(2l+1)!!/(\theta_\perp^l(l+1))}, \tag{3.23}$$

instead of, cp. eq. (3.9),

$$\epsilon_l^{\text{SRM}} = \left[\frac{2a(2l+1)}{\pi}\int_0^\infty \frac{dk}{\epsilon(\mathbf{k},\omega)} j_l^2(ka)\right]^{-1}. \tag{3.24}$$

Despite their different functional form, these two expressions yield very similar values over the VIS and NIR spectrum, which are in turn far from the values of the corresponding local permittivity. We illustrated this in Fig. 3.1 (a) for the $l = 1$ coefficient (dipole scattering) of gold spheres of two different radii. Differences in the presented semi-classical theories become, however, more apparent, when the fully retarded hydrodynamic model is used and the nanostructures become more complex. For larger particles, the skin depth additionally yields non-vanishing contributions as a consequence of the interplay with retardation. This is shown in Fig. 3.1 (b) for a dimer structure with 20 nm particles and a gap size of 0.5 nm.

To make predictions that can be compared to experiments, we use these expressions to obtain the extinction cross section of an individual sphere as

$$\sigma_{\text{ext}} = \frac{2\pi}{k^2\epsilon_0}\sum_l (2l+1)\text{Im}(t_l^E + t_l^M). \tag{3.25}$$

The values of the scattering coeffients t_l^E, t_l^M obtained from the SRM and the hydrodynamic approach are introduced in this equation to compute the extinction.

Discussion of results

We first explore the combined effects of nonlocality and retardation in individual gold spheres. Figure 3.2 (a) presents extinction spectra calculated for a wide range of particle diameters from the retarded hydrodynamic model. The maximum of the dipole plasmon peak and its half-maximum contour are indicated by the gray and brown curves, respectively. The dipole resonance is clearly broadened for particles above 10 nm due to retardation. It is also significantly broadened for sizes below 1 nm due to nonlocal effects. Retardation is producing a red shift of the dipole peak that grows with particle size as a result of the longer time needed by opposite parts of the particle to interact electromagnetically when the diameter is comparable to the wavelength. The skin depth also plays a role for particles >10 nm. In contrast, nonlocality gives rise to a small blue shift, which comes from the effective reduction in the magnitude of the permittivity because the induced charges penetrate inside the particle by an amount that is not negligible compared to the diameter.

The spectra derived from the two presented nonlocal models are compared with local theory and with related experiments in Fig. 3.2 (b) and (c) for gold spheres of two different sizes. The local description clearly fails, especially for the smaller particle. In contrast, the SRM and the

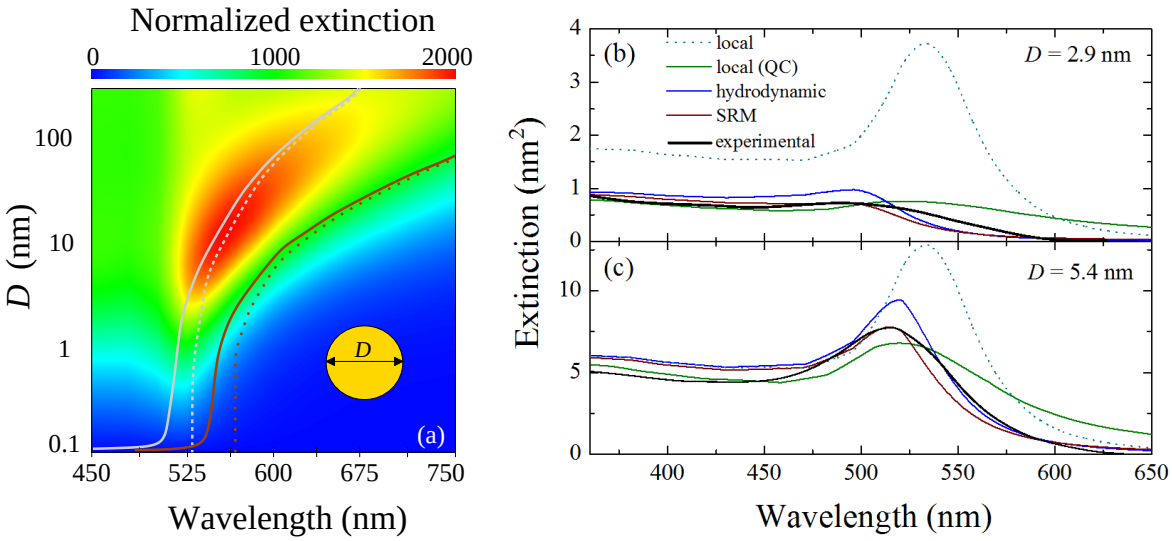

Fig. 3.2: **Combined effect of retardation and nonlocality in individual metal nanoparticles.** (a) Extinction spectra of spherical gold particles in water over a wide range of diameters D as calculated from the hydrodynamic model including nonlocal and retardation effects. The plasmon peak wavelength is shown as a solid gray curve. The contour corresponding to half the maximum extinction for each value of D is also shown (solid brown curve). For comparison, we include the corresponding contours calculated in the retarded, local approximation (broken curves). The color scale for the extinction cross section is normalized to the projected area of the sphere. (b) Gold particles surrounded by glass of permittivity $\epsilon_0 = 2.3$. Comparison between experiment[36] (black curve) and theory using different models for the particle response: local response using tabulated optical data,[146] modified local response incorporating quantum-confinement (QC) in a phenomenological way (eq. (2.15)); fully retarded hydrodynamic model, including nonlocal effects; and nonretarded, nonlocal specular reflection model (SRM).

hydrodynamic model produce results that are in good agreement with the measurements in both the position of the plasmon peak and the shape of the spectra. Finally, the phenomenological quantum-confinement model (local QC, see eq. (2.15)) improves the local description but deviates considerably from nonlocal theories and experiment in both the plasmon peak and the longwavelength spectral profile. It is clear that the two presented parameter-free nonlocal descriptions are better capturing the effects of spatial dispersion, which are absent in all other models. The similarity between the SRM and the hydrodynamic model in Fig. 3.2 (b) and (c) indicates that the two approaches provide an equivalent description of spatial dispersion in the small-particle limit, without retardation effects. In fact, as shown before, the single sphere polarizability in the hydrodynamic model reduces to the expression found for the SRM eq. (3.8) and (3.17) in that limit, with a different expression for ϵ_l given by eq. (3.23). We compare this formula with the SRM in Fig. 3.1 (a) and find just small numerical differences between them.

Equation (3.25) applies to many other geometries on replacing the scattering matrix ob-

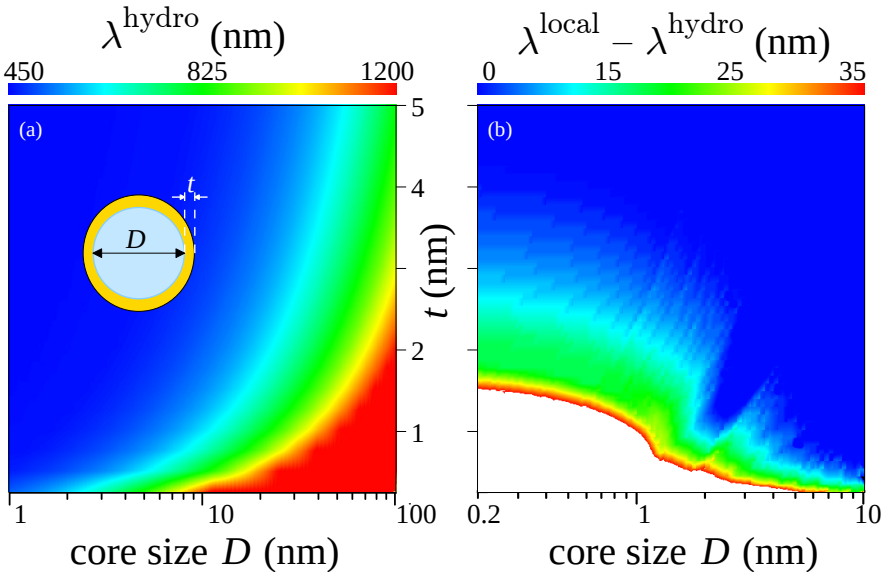

Fig. 3.3: **Core size D and thickness t dependence of nonlocal and retardation effects in individual nanoshells.** (a) Resonance wavelength of silica spheres coated with gold and immersed in water, as obtained from the fully retarded, nonlocal hydrodynamic model. (b) Shift of the plasmon wavelength in the hydrodynamic model relative to the local theory.

tained either from analytical evaluations or from e. g. boundary element method (BEM) calculations. For nonlocal metal nanoshells the scattering coefficients become more involved as discussed previously and shown in the appendix section 6.3, but are still analytical. In Fig. 3.3 (a) we show the dependence of the lowest-energy plasmons on coating thickness and core diameter for silica spheres coated with gold. A strong red shift is observed with increasing particle size due to retardation and also with decreasing coating thickness due to plasmon hybridization.[153] Nonlocal effects produce dramatic blue shifts in the plasmon wavelength compared to the local description for thin coatings, as we show in Fig. 3.3 (b). These effects are somehow reduced when the particle size increases, possibly as an indication that plasmon motion becomes less confined along surface directions.

Moreover, the single-particle scattering coefficients provide all of the necessary information to characterize the optical response to either multiple external sources or the fields scattered by other neighboring particles. We use a multiple elastic scattering of the multipolar expansions (MESME) method[132] allowing us to compute the scattering of aggregated particles, including dimers and antenna structures. We show in Fig. 3.1 (b) extinction spectra of a gold dimer calculated with local and nonlocal theories. Here both nonlocal descriptions predict slightly different plasmon resonance positions. The differences in the two nonlocal approaches become more obvious because the hydrodynamic model includes retardation, its results hold also for larger structures, in contrast to the nonretarded SRM theory. The difference between both nonlocal curves is however small compared to the deviation from the local one. Clearly, the local theory overestimates the red shift of the prominent gap mode due to particle interaction

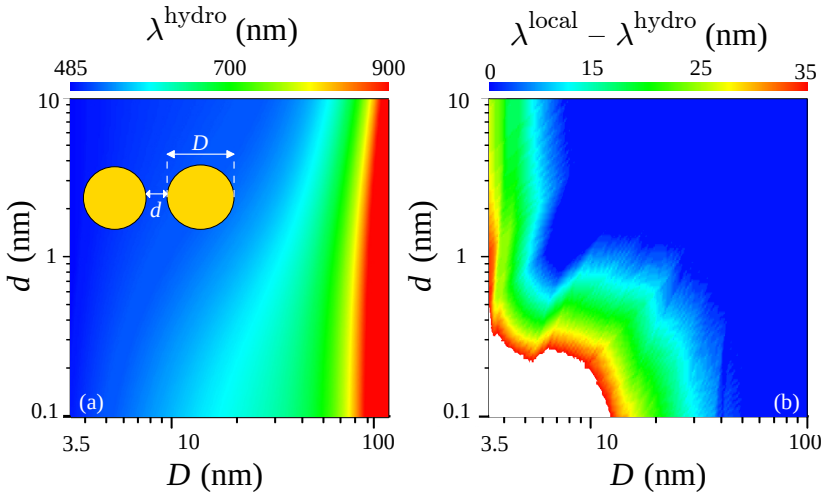

Fig. 3.4: **Size D and spacing d dependence of nonlocal and retardation effects in particle dimers.** (a) Wavelength dependence of the lowest-order longitudinal plasmon on d and D, as obtained from the fully retarded, nonlocal hydrodynamic model for gold spheres in water. (b) Displacement of the plasmon wavelength in the hydrodynamic model compared to local theory.

with narrow gaps, even when the size of the particles is large enough to prevent nonlocal effects in the isolated particles (see Fig. 3.2 (a)).

We present in Fig. 3.4 a detailed analysis of the combined effects of retardation and nonlocality in dimers. The gap plasmon is red-shifted with increasing particle size or decreasing gap separation, Fig. 3.4 (a). The shift produced by nonlocality compared to the local theory, Fig. 3.4 (b), is more pronounced for small spheres, but also for small separations below 1 nm even in relatively large particles >20 nm.

The effect of nonlocality is even stronger when more particles are involved, as in particle arrays or in the Yagi-Uda nanoantenna considered in Fig. 3.5. Similar structures have been recently used to pattern the angular distribution of emission from single molecules. The difference between local and nonlocal descriptions is clearly observed in the spectra of Fig. 3.5 (a), showing a significant plasmon shift, especially if one relates it to the distance between the emission peak wavelength and the gold plasmon threshold ~ 20 nm. But the difference is even more striking when we examine the angular distribution of emission, showing a mismatch of the emission direction and an overall reduced emission when accounting for nonlocal properties of the metal nanoparticles.

3.1.3 Nonlocal Fresnel's coefficients

In this section, we further investigate planar plasmonic systems when taking into account the effects of nonlocality with the hydrodynamic model including retardation. Our aim is to look at basic building blocks and their striking functionalities and to demonstrate how their properties are altered implementing the nonlocal nature within the dielectric response,

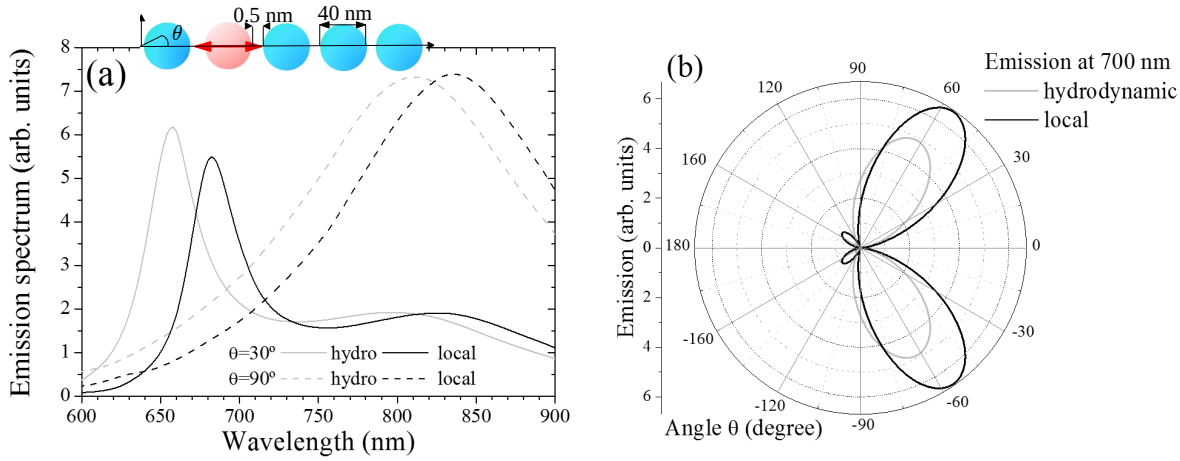

Fig. 3.5: **Angular dependent emission from local and nonlocal Yagi-Uda nanoantennas.** (a) Emission spectrum from the antenna depicted in the inset for gold particles of 20 nm radius spaced by 1 nm. The emitting dipole is taken at the center of the second sphere and aligned along the particle array. The emission is collected along a direction perpendicular to the array axis. (b) Angular dependence of the emission at a wavelength of 700 nm.

see Fig. 3.6 (a). To investigate bulk nonlocality in such systems, it is desirable to derive the nonlocal analogue to Fresnel's coefficients.[4] We provide a tutorial and entirely analytical insight into planar plasmonic structures with illustrative examples studying nonlocal response for single interfaces, finite metal slabs and gap geometries. Solving the respective boundary value problems, we arrive at analytical optical coeffcients for abrupt interfaces, i. e. a uniform electron distribution inside the metal, which neglects the effect of the electron spill-out. This results in additional longitudinal modes not present in the local approximation. Differences in the performance of plasmonic devices compared to the local approximation are discussed on the basis of this analytic study together with the results obtained for the extended hydrodynamic model to additionally include the effect of the electron spill-out in the next section.

Fresnel's optical coefficients describe the behaviour of electromagnetic waves crossing a planar interface between media of differing refractive indices. We derive these coefficients in single slab environments consisting of nonlocal metal films or metal-insulator-metal structures. We choose the surface normal parallel to the propagation direction $\hat{\mathbf{z}}$, such that field components along the interface propagate with $e^{i\mathbf{k}_\parallel \mathbf{R}}$, with $\mathbf{R} = (x, y)$. The electric field in nonlocal media consists of transversal and longitudinal components in contrast to the local approximation, where only transversal waves are reflected and transmitted at a metal to dielectric interface. This leads to the wave numbers $k_{z_0}^2 = \frac{\omega^2}{c^2}\epsilon_0 - k_\parallel^2$, $k_{z_1}^2 = \frac{\omega^2}{c^2}\epsilon_\perp - k_\parallel^2$ associated to light propagation in the dielectric and to transversal waves in the metal, respectively. Note that all wave numbers obey $\mathrm{Im}\{k_{z_i}\} > 0$. The inhomogeneous solution to the electric field wave equation (2.19), eq. (2.25), determines the longitudinal modes, which propagate with $e^{\pm i q_0 z}$, where q_0 is given by eq. (2.23) and we demand $\mathrm{Im}\{q_0\} > 0$ here, too.

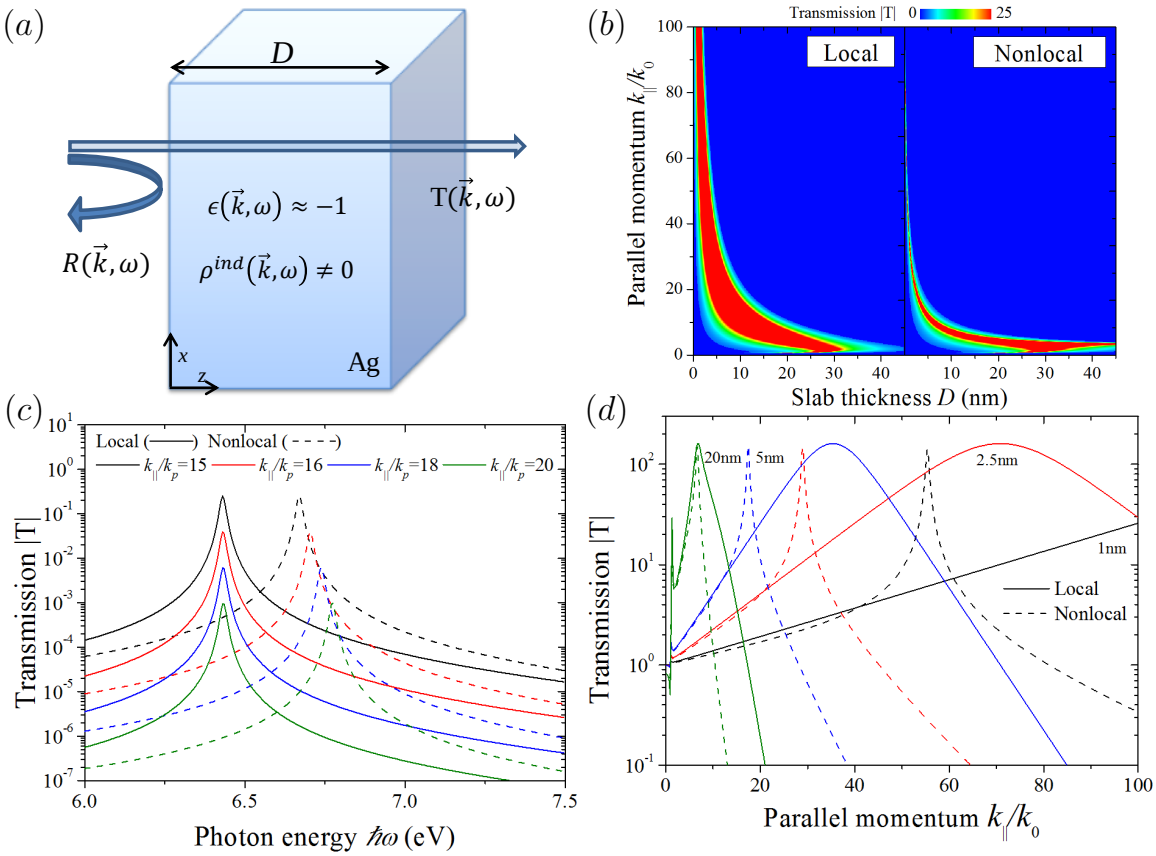

Fig. 3.6: **Optical properties of a silver slab at $\omega = \omega_p/\sqrt{2}$ in the local approximation and with nonlocal response.** (a) Illustration of the setup under consideration using a silver slab with Drude response and $\omega_p = 9.1$eV and $\gamma_p = 0.02$eV. (b) Transmission $|T|$ as a function of parallel momentum $k_\parallel$ and slab thickness D including realistic damping γ_p. (c) At specific parallel momenta $k_\parallel$ we plot $|T|$ as a function of photon energy $\hbar\omega$ for $D = 10$nm. The values chosen are normalized by $k_p = \omega_p/c$. (d) For various slab thicknesses we plot $|T(k_\parallel)|$ at the frequency $\omega = \omega_p/\sqrt{2}$.

We solve for the coefficients of reflection r and transmission t of a single metal-dielectric interface by evaluating the retarded Maxwell's equations together with the linearized hydrodynamic equation. The boundary conditions[72,163] given by $\hat{\mathbf{z}} \cdot \mathbf{j}^{\text{ind}} = 0$, $\hat{\mathbf{z}} \times \delta\mathbf{E}_\parallel = 0$ and the continuity of $\epsilon_b \hat{\mathbf{z}} \cdot \mathbf{E}_\perp$ lead to a set of three equations for the metal-dielectric interface. We restrict ourselves to incident p-polarization (TM) waves and note that the classical Fresnel equations do not change in case of s-polarization, assuming non-magnetic media with permeability $\mu = 1$.

Note, that the incident wave is always considered to be transversal. However, on entering a nonlocal metal both transversal and longitudinal polarizations are excited. Considering multiple reflections inside a metal slab, the case of a longitudinal wave incident on a metal-to-dielectric interface has to be regarded, too. This results in three sets of optical coefficients. At a dielectric-to-metal interface the following transversal (index p) and longitudinal (index

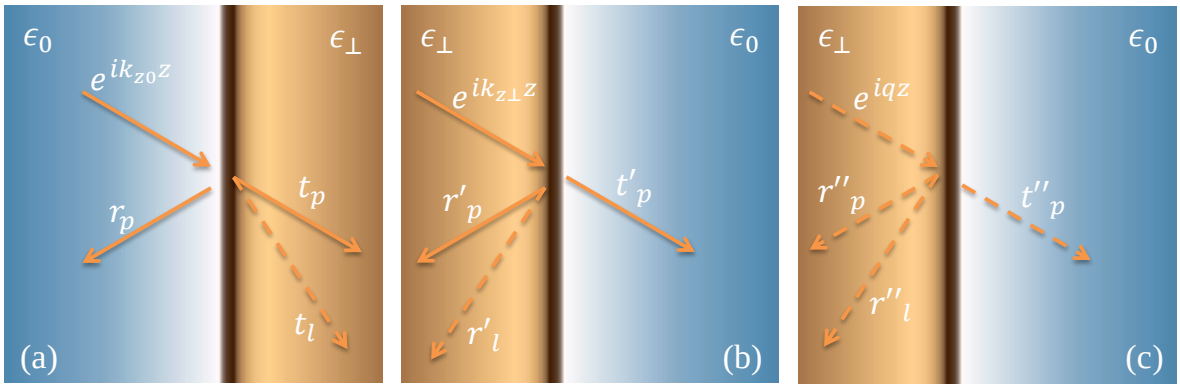

Fig. 3.7: **Illustration of excited transversal and longitudinal waves at planar interfaces.** (a) A transversal wave incoming from the dielectric side excites both transversal and longitudinal transmitted waves. Within the dielectric only a transversal component is reflected. (b) A transversal wave incoming from the metal side excites both transversal and longitudinal reflected waves. On the dielectric side only a transversal component is transmitted. (c) A longitudinal wave incoming from the metal side excites both transversal and longitudinal reflected waves. On the dielectric side only a transversal component is transmitted. Dashed optical components are uniquely found in the nonlocal description. In the local approximation, they all vanish and the case (c) does not occur.

l) modes are found for p-polarization, illustrated in Fig. 3.7

$$r_p = \frac{k_{z_0}\epsilon_\perp - k_{z_1}\epsilon_0(1+g)}{k_{z_0}\epsilon_\perp + k_{z_1}\epsilon_0(1+g)}, \tag{3.26a}$$

$$t_p = \frac{2k_{z_0}\sqrt{\epsilon_0\epsilon_\perp}}{k_{z_0}\epsilon_\perp + k_{z_1}\epsilon_0(1+g)}, \tag{3.26b}$$

$$t_l = F_l t_p = \frac{k_\parallel (k_\parallel^2 + q^2)^{1/2}}{qk\sqrt{\epsilon_\perp}} \left(\frac{\epsilon_\perp}{\epsilon_b} - 1\right) t_p. \tag{3.26c}$$

Likewise, for a transversal wave incident on a metal-to-dielectric interface, Fig. 3.7 (b), we have

$$r'_p = \frac{k_{z_1}\epsilon_0(1-g) - k_{z_0}\epsilon_\perp}{k_{z_0}\epsilon_\perp + k_{z_1}\epsilon_0(1+g)}, \tag{3.27a}$$

$$t'_p = \frac{2k_{z_1}\sqrt{\epsilon_0}\epsilon_\perp/\sqrt{\epsilon_\perp}}{k_{z_0}\epsilon_\perp + k_{z_1}\epsilon_0(1+g)}, \quad r'_l = F_l(1+r'_p). \tag{3.27b}$$

Finally, for the case of a longitudinal wave incident on a metal-to-dielectric interface, Fig. 3.7 (c), we find

$$r''_p = \frac{2kk_\parallel\epsilon_0\sqrt{\epsilon_\perp}/(q^2+k_\parallel^2)^{1/2}}{k_{z_0}\epsilon_\perp + k_{z_1}\epsilon_0(1+g)}, \tag{3.28a}$$

$$t''_p = \frac{2kk_\parallel\epsilon_\perp\sqrt{\epsilon_0}/(q^2+k_\parallel^2)^{1/2}}{k_{z_0}\epsilon_\perp + k_{z_1}\epsilon_0(1+g)}, \quad r''_l = F_l r''_p + 1. \tag{3.28b}$$

Without loss of generality, these expressions also include intrinsic material losses via the complex permittivity of the materials. The overall form of the transversal modes is similar to the local Fresnel coefficients, but the resonance structure now depends on the parallel momentum via the additional, nonlocal term

$$g = \frac{k_\parallel^2}{q k_{z_1}} \left(1 - \frac{\epsilon_\perp}{\epsilon_b}\right). \tag{3.29}$$

In the local limit ($k_\parallel \to 0$), the usual optical coefficients are recovered, and the additional longitudinal contributions, not present in the local case, vanish as $g \to 0, F_l \to 0$. For a metal slab or an metal-insulator-metal (MIM) structure, we need to consider multiple reflections in the inner layer. In contrast to the local approximation, additional contributions from scattered longitudinal waves are found and we therefore need to sum all components to arrive at the overall expressions for the transmittance and reflectance.

Fig. 3.6(b) shows the transmission versus slab thickness and parallel momentum (normalized by $k_0 = \omega/c$) at imaging conditions, i. e. $\omega = \omega_p/\sqrt{2}$, including intrinsic resistive losses for a silver slab in an air environment. We predict a reduction in the momentum bandwidth for the presented nonlocal case, which is a direct consequence of additional loss channels introduced by the augmented sensitivity with parallel momentum via eq. (3.29). The coupling to the longitudinal modes, not present in the local approximation, results in sharpened resonances shifted towards lower parallel momenta as seen in Fig. 3.6 (d). For increasing slab thicknesses the nonlocal results converge to the local limit. In all cases however, both for the local and nonlocal examples, as expected, we find transmissions exceeding unity due to the amplification of evanescent waves. Spectrally, as illustrated in Fig. 3.6 (c), we reconfirm that optical modes become dependent on $k_\parallel$ in nonlocal theories both for their resonance position and width. The resultant blueshift leads to a reduction in the transmission for increasing spatial dispersion. In other words, a local metal slab shows resonances independent with parallel momentum (for high enough $k_\parallel$), while in the nonlocal case a frequency mismatch is observed that depends crucially on the parallel momentum.

The electrostatic limit for the optical coefficients is obtained from the above equations (3.26a) - (3.28b), as well as for the nonlocal parameter, eq. (3.29), in a straightforward manner by replacing $k_z \to ik_\parallel$. In the next section, we use the above equations for sharp interfaces in the static (and also local) limit to compare with results for the extended nonlocal theory including the electron spill-out using smooth electron density profiles.

3.2 Nonlocal edge effects

The hydrodynamic model is able to combine both bulk and edge effects on investigating smoothly changing electron density profiles in eqs. (2.18) and (2.21), see Fig. 3.8. We extend the hydrodynamic model to describe such metal surfaces with an abrupt jellium edge displaced at a position $z_b \leq 0$ inside of the metal region and solve for optical coefficients in such systems using a transfer matrix approach along the direction of the density profile. Interestingly, this approach also allows us to study systems with local response, yet including the aspect of smooth electron density profiles. The impact of this is discussed carefully in the final sections of this chapter.

A variety of plasmonic devices is investigated comparing local and nonlocal response, as well as sharp and smooth interfaces on their performance and properties. We demonstrate that the hydrodynamic model can reasonably well describe the nonlocal effects that arise from collective electron quantum interactions in metal surfaces and narrow gaps between metals including the spill-out of conduction band electrons. Within this approach, we are capable of reproducing experimentally determined plasmon blueshifts in noble metals. Systems involving small gaps display a regime of tunneling electrons, which is partially captured in this semi-classical picture by overlapping electron densities. The formation of tunnel junctions leads to further, classically unexpected observations. Electron tunneling is not only a nonlinear effect, but it is also remarkably enhanced by nearby molecules. The presence of charge transfer plasmons (CTPs) in narrow gaps completely alters the optical response of the whole structure, which has been demonstrated with numerical *ab initio* methods.[44,45,47,49,80] We apply our method to planar structures, thin films and metal-insulator-metal waveguides which allows us to describe charge transfer plasmons and other nonlocal effects allowing for rapid evaluations of various compositional parameters.

3.2.1 The transfer matrix approach for smooth surfaces

Realistic metal interfaces, as depicted in Figs. 1.1 (b) and 3.8 (a) and (b), consist of a rather sharp jellium edge and a smooth distribution of conduction band electrons allowing for a spill-out of electrons into the surrounding medium. We distinguish between nonlocal bulk effects, that are subject to the uniform electron distribution inside the metal structure, and edge effects, which are dominated by the smoothly changing electron distribution around the interface. The former have been studied separately in the previous sections.

Here, we demonstrate that the hydrodynamic model can be exploited to describe the effects connected to the electron spill-out in addition to nonlocal bulk properties. In our approach, we exploit the common transfer matrix approach to obtain the optical response of one dimensional

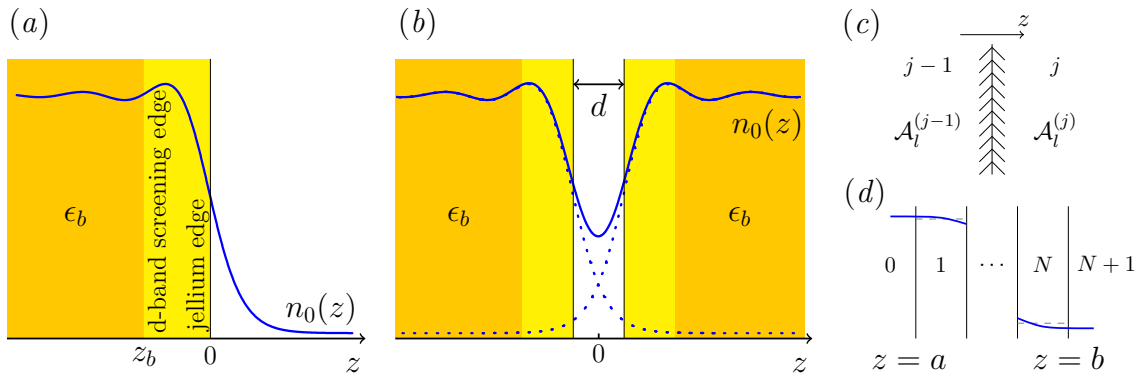

Fig. 3.8: **Illustration of smooth electron density profiles and discretization method used to simulate their optical response.** (a) Density profile for a single gold interface (blue curve, taken from Ref.[42]) relative to the positions of the jellium edge ($z = 0$) and the outermost atomic plane ($z = z_b \approx -0.118\,\mathrm{nm}$). (b) Same as (a) for a gap of jellium-to-jellium distance d. (c), (d) Discretization along the normal direction z and relevant parameters used in the numerical procedure.

structures described by a smoothly changing electron density.[42]

Solving the present problem with a transfer matrix approach has several advantages. The numerical procedure converges for a few hundred slices for each interface and all expressions used for the matrix multiplication are analytical. No additional fitting parameter is needed. In contrast to first-principle calculations, such as DFT and (TD)LDA, this approach allows for rapid evaluation of different structures and materials, and it allows including a vast number of metal surfaces, since the electron density profile can be arbitrarly defined. We focus on surfaces, gaps, and thin films that comprise smooth planar interfaces and are homogeneous along planes normal to the z direction. All physical quantities can then be expressed as a sum over wave vector components $\mathbf{k}_\parallel$ and the dependence on $\mathbf{R} = (x, y)$ comes through an implicitly understood $e^{i\mathbf{k}_\parallel \mathbf{R}}$ factor. This allows us to make the substitution $\nabla \to (i\mathbf{k}_\parallel, \partial_z)$. We adapt eqs. (2.22) and (2.21) to this situation and obtain

$$\left(\beta^2 \rho^{\mathrm{ind}}\right)'' + q_0^2 \beta^2 \rho^{\mathrm{ind}} = \frac{-e^2}{m_e} \left(\frac{n_0}{\epsilon_b}\right)' \left(\epsilon_b \phi'\right), \tag{3.30}$$

$$\phi'' - k_\parallel^2 \phi + \frac{\epsilon_b'}{\epsilon_b} \phi' = -\frac{4\pi}{\epsilon_b} \rho^{\mathrm{ind}}, \tag{3.31}$$

where the prime denotes differentiation with respect to z. Interestingly, this expression involves the local transversal permittivity $\epsilon_\perp(z)$, which depends on the plasma frequency $\omega_p(z)$ defined now in terms of a z-dependent unperturbed electron density n_0, depicted in Fig. 3.8 (c) and (d).

Our strategy to model a nonlocal medium that is inhomogeneous along the z direction consists in describing it as a concatenation of uniform layers j of vanishing thickness $\Delta z_j \to 0$. We thus need to have the solution of the above equations for nonlocal homogeneous media, as well as the reflection and transmission at sharp interfaces separating the different layers.

Homogeneous medium

The right hand side of eq. (3.30) vanishes in a homogeneous medium j, so that we can write the induced electron density ρ^{ind} as a combination of two waves propagating towards positive and negative z directions,

$$\rho^{\text{ind}} = \mathcal{A}_1^{(j)} e^{iq_0^{(j)} z} + \mathcal{A}_2^{(j)} e^{-iq_0^{(j)} z}, \tag{3.32}$$

where the coefficients $\mathcal{A}_l^{(j)}$ will be determined by the boundary conditions, that define the transfer matrix. Inserting eq. (3.32) into eq. (3.31), we can write the potential as

$$\phi = \mathcal{A}_3^{(j)} e^{-k_\parallel z} + \mathcal{A}_4^{(j)} e^{k_\parallel z} + B^{(j)} \rho^{\text{ind}}, \tag{3.33}$$

where $B^{(j)}$ is given by the particular solution to the electrostatic wave equation, presented in eq. (2.25). Obviously, these solutions depend on the properties of each medium j through n_0 and ϵ_b, which act as input parameters that determine other derived quanties such as β, q_0, and $\epsilon_\perp$.

Transfer-matrix approach

We intend to find a transfer matrix $\mathbf{T}^{(j,j-1)}$ that relates the coefficients $\mathcal{A}_l^{(j)}$ in medium j to those in medium $j-1$,

$$\mathcal{A}^{(j)} = \mathbf{T}^{(j,j-1)} \cdot \mathcal{A}^{(j-1)}. \tag{3.34}$$

The two media are separated by a sharp interface, as illustrated in Fig. 3.8 (c) and (d). Using eq. (3.32) and eq. (3.33) with the origins of the exponentials defined at the interface, we find $\mathbf{M}^{(j)} \cdot \mathcal{A}^{(j)} = \mathbf{M}^{(j-1)} \cdot \mathcal{A}^{(j-1)}$, where the rows of the matrix

$$\mathbf{M}^{(j)} = \begin{pmatrix} B^{(j)} & B^{(j)} & 1 & 1 \\ iq^{(j)}\epsilon_b^{(j)} B^{(j)} & -iq^{(j)}\epsilon_b^{(j)} B^{(j)} & -\epsilon_b^{(j)} k_\parallel & \epsilon_b^{(j)} k_\parallel \\ {\beta^{(j)}}^2 & {\beta^{(j)}}^2 & 0 & 0 \\ -C^{(j)} & C^{(j)} & \frac{e^2}{m_e} k_\parallel n_0^{(j)} & -\frac{e^2}{m_e} k_\parallel n_0^{(j)} \end{pmatrix} \tag{3.35}$$

are extracted from the boundary conditions ϕ, $\epsilon_b \partial_z \phi$, $\beta^2 \rho^{\text{ind}}$, and j_z^{ind} (i.e. the magnitudes that are continuous across the interface), where we have further defined for convenience

$$C^{(j)} = iq^{(j)} {\beta^{(j)}}^2 \epsilon_b^{(j)} / \epsilon_\perp^{(j)}.$$

When more interfaces are considered, it is convenient to choose the origins of the exponentials of eq. (3.32) and eq. (3.33) at the right end of each homogeneous layer, so that the transfer matrix $\mathbf{T}^{(j,j-1)}$ in eq. (3.34) must include the propagation across layer j of thickness Δz_j.

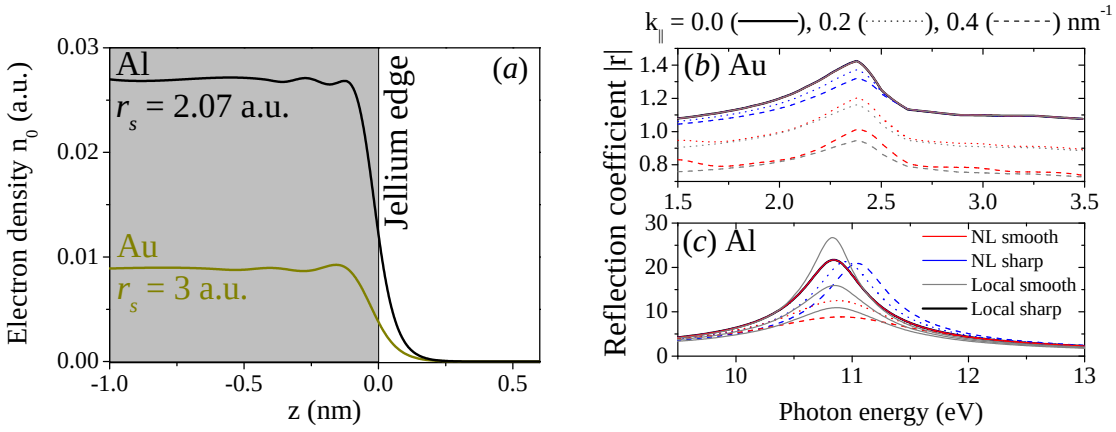

Fig. 3.9: **Smooth electron density profiles and reflection spectra for gold and aluminum.** (a) Gold and aluminium electron density profiles $n_0(z)$ in atomic units taken from Ref.[42] indicating the corresponding Wigner-Seitz radius r_s. (b) Au and (c) Al reflection spectra in the different theories for several parallel momenta.

This yields

$$\mathbf{T}^{(j,j-1)} = \mathbf{P}^{(j)} \cdot \frac{1}{\mathbf{M}^{(j)}} \cdot \mathbf{M}^{(j-1)},$$

where the corresponding propagators read

$$\mathbf{P}^{(j)} = \begin{pmatrix} e^{iq_0^{(j)}\Delta z_j} & 0 & 0 & 0 \\ 0 & e^{-iq_0^{(j)}\Delta z_j} & 0 & 0 \\ 0 & 0 & e^{-k_\parallel \Delta z_j} & 0 \\ 0 & 0 & 0 & e^{k_\parallel \Delta z_j} \end{pmatrix}. \tag{3.36}$$

Finally, for a smooth interface described by N films of media $j = 1, \ldots, N$, with medium $j = 0$ ($j = N+1$) to the left (right) end of the interface (see Fig. 3.8 (d)), the full transfer matrix reduces to

$$\mathbf{T} = \frac{1}{\mathbf{M}^{(N+1)}} \cdot \mathbf{M}^{(N)} \cdot \mathbf{T}^{(N,N-1)} \cdot \ldots \cdot \mathbf{T}^{(1,0)}$$

and the propagation across the full interface is expressed as

$$\mathcal{A}^{(N+1)} = \mathbf{T} \cdot \mathcal{A}^{(0)}. \tag{3.37}$$

Note that the z origin of the exponentials in medium $N+1$ must be reset to the left end of that medium. Matrix $\mathbf{T}$ propagates the coefficients of eqs. (3.32) and (3.33) from position $z = a$ at the $0|1$ interface to position $z = b$ at the $N|N+1$ interface (see Fig. 3.8 (d)).

In our simulations, we obtain full convergence with increasing N by setting all thicknesses $\Delta z_j \sim 0.001\,\text{nm}$. For a metal surface, only the varying part of the density profile near the

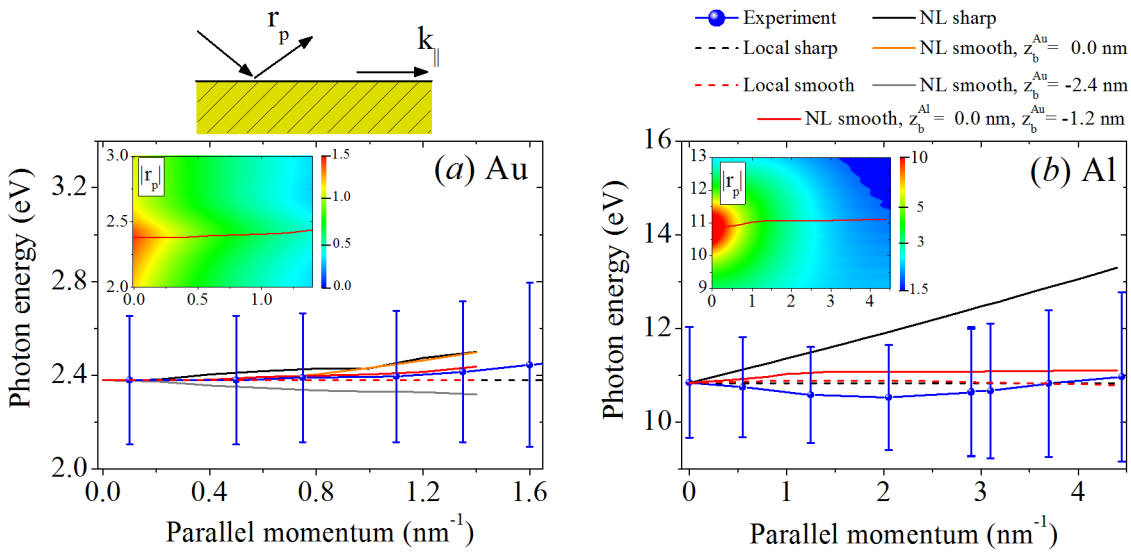

Fig. 3.10: **Surface plasmon dispersion in gold and aluminum.** We present results obtained from different models for the surface plasmon dispersion relation (see upper right legend), as compared with experimental data for (a) gold[164] and (b) aluminum.[165] The insets show the calculated reflection coefficient $|r_p|$ as obtained from the NL smooth theory. Different positions of the d–band background screening edge relative to the jellium edge are considered for gold.

interface has to be computed in this way. Propagation in the bulk of the material is simply described by eqs. (3.30) and (3.31). Incidentally, the last interface with a local medium (e. g. vacuum) has to be taken with care, and we obtain converged results in the limit when the local medium is simply approached by setting $n_0 \to 0$.

3.2.2 Nonlocal smooth reflection spectra

The impact of smooth electron density profiles and related nonlocal effects on the optical response of metal surfaces, dielectric gaps and thin metal films is discussed in depths. We present a range of surface and gap plasmon dispersions for varying geometrical parameters. Note, that we use permittivities of the noble metal Au and the simple metal Al according to the values and discussion in the appendix, section 6.1. We base our electron density profiles on findings from DFT calculations,[42] which include Friedel oscillations as depicted in Fig. 3.9 (a) and schematically in Fig. 3.8 (a) and (b).

In Fig. 3.9 (b) and (c), we give for both materials spectra of the single interface reflection coefficient $|r_p|$ calculated for local and nonlocal (abbreviated NL in the graphs) sharp interfaces as well as for local and nonlocal smooth interfaces for several parallel momenta. The thus extracted surface plasmon dispersion for Au and Al surfaces is depicted in Fig. 3.10, comparing available experiments[164,165] with our calculations on the different theories. The following important points can be noticed at this stage: (i) The local descriptions for both

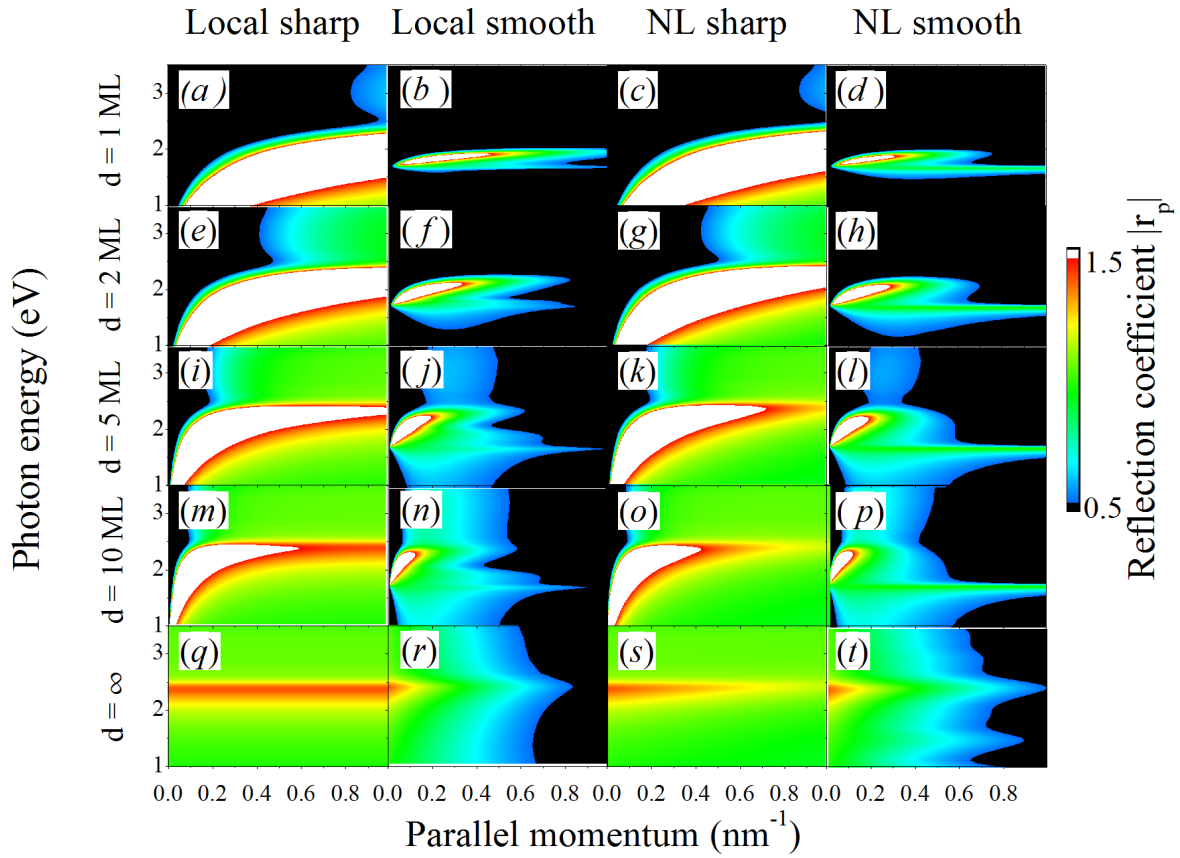

Fig. 3.11: **Plasmon dispersion in thin gold films, scattering.** We compare the momentum and energy dependence of the radiation scattering in terms of the reflection coefficient $|r_p|$ for a thin gold film of different numbers of (111) atomic layers (left labels), including the limit of the semi-infinte surface.

sharp and smooth interfaces agree in their peak position, i. e. a dispersionless surface plasmon resonance is found in the electrostatic limit, (ii) the local smooth spectra are attenuated with increasing parallel momenta in agreement with the NL smooth description and (iii) the observed spectral shift with increasing parallel momentum is larger in the NL sharp model than in the NL smooth, indicating that the impact of the smooth surface counteracts the previously found strong blueshifts in the case of implementing only nonlocal bulk properties. These observations hold for both presented metals and have significant implications on the optical response in various structures discussed in this work.

In the case of Au (Fig. 3.10 (a)), a blueshift similar to recent experiments[164] shows an overall excellent agreement when we account for a displacement of the *d*–band screening edge inside the metal by half the distance between atomic planes $z_b = 0.408\text{nm}/(2\sqrt{3}) \approx -0.118\,\text{nm}$.[166] On the other hand, using $z_b \equiv 0$ results in a redshift and displacing it too far into the metal region overestimates the noted blueshift, as the nonlocal bulk calculations for sharp interfaces do. This is in accordance to previous findings using *ab initio* methods.[43]

For the simple metal Al (Fig. 3.10 (b)), where no displacement of the *d*-band screening edge

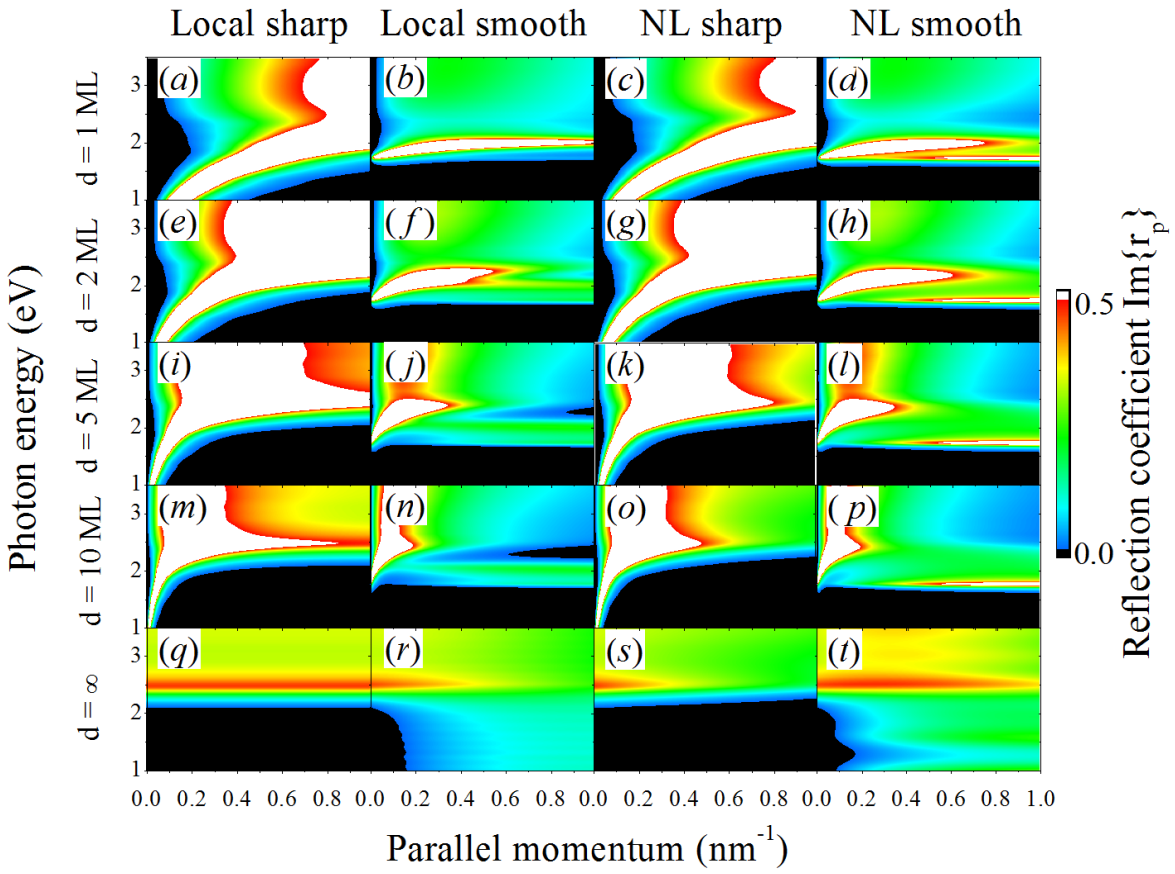

Fig. 3.12: **Plasmon dispersion in thin gold films, absorption.** The absorption is shown in terms of the imaginary part of the reflection coefficient $\mathrm{Im}\{r_p\}$ for the different theories (see upper labels) calculated for various film thicknesses including the limit of the semi-infinte surface.

is used ($z_b = 0\,\mathrm{nm}$), the experimental[165] results show a significant difference to both local and nonlocal sharp calculations. Although the nonlocal smooth theory does give a remarkable correction towards this, it is not capable to predict the initial redshift found in this simple metal. Note, that the only material parameter in our approach, that is not changed along the electron density profile, is the intrinsic damping γ_p. In the case of Al, this damping value is significantly larger than in the case of Au and its additional variation might yield the desired result.

For thin gold films we compare both radiation scattering and absorption extracted from reflection spectra in Figs. 3.11 and 3.12 for increasing slab thickness. In particular, we observe that the different theories tend to converge for increasing film thickness including the limit of a semi-infinite surface.

Interestingly, we observe the main differences not between local and nonlocal calculations, but between simulations of sharp interfaces and such involving the smooth electron density profile. While the nonlocal cases predict an additional, k-dependent damping mechanism, leading to a plasmon quenching for increasing parallel momenta, the impact of the smooth

electron density distribution is more severe and constitutes itself a source of plasmon quenching. We stress at this point, that the local smooth calculations display this attenuated behaviour, but show for all considered geometries the same plasmon dispersion as usual local calculations. This indicates, that the electron spill-out yields mainly additional damping, if k-dependent interaction between conduction band electrons is neglected.

3.2.3 The local smooth limit

We here briefly derive the local smooth limit that is able to demonstrate the influence of the extended electron density independently of the nonlocal response properties of the conduction band electrons and investigate for which conditions the local description is sufficient to describe optical resonances.

We obtain the local smooth description in two ways, as a limit of the nonlocal smooth theory, previously introduced, decreasing the hydrodynamic, nonlocal parameter β with a factor f as $f\beta^2 \to 0$ or by deriving similar expressions as in the main theory for the case of local materials. In this case, the hydrodynamic equation (2.18) reduces to ($\beta = 0$)

$$i(\omega + i\gamma)\mathbf{j}^{\mathrm{ind}} = \frac{e^2 n_0}{m_e}\nabla\phi, \tag{3.38}$$

which together with the continuity reads after elimination of $\mathbf{j}^{\mathrm{ind}}$

$$\rho^{\mathrm{ind}} = \frac{e^2}{m_e}\left[n_0'\phi' + n_0\phi''\right]/\omega(\omega + i\gamma). \tag{3.39}$$

Using $\epsilon_b - \epsilon_\perp = \omega_p^2/\omega(\omega + i\gamma)$ we obtain

$$\rho^{\mathrm{ind}} = \left[(\epsilon_b' - \epsilon_\perp')\phi' + (\epsilon_b - \epsilon_\perp)\phi''\right]/\omega(\omega + i\gamma). \tag{3.40}$$

This does not consitute a wave equation for the induced charge density as in the nonlocal theory, but a prescription that we directly insert into eq. (2.21). The modified local smooth model employing the hydrodynamic equation in absence of nonlocal parameters, but in presence of a smooth electron density reads

$$\phi'' - k_\parallel^2\phi + \frac{\epsilon_\perp'}{\epsilon_\perp}\phi' = 0. \tag{3.41}$$

Obviously, we regain the common local (electrostatic) wave equation. The hydrodynamic equation provides thus the substitution of $\epsilon_b \to \epsilon_\perp$ which corresponds to the local limit. This reduces the transfer matrix approach shown before to a single wave equation, 2×2 matrices and the usual boundary conditions at interfaces $j \to j + 1$.

We demonstrate the suitability of the nonlocal smooth approach to yield the local smooth limit in Fig. 3.13 for metal surfaces. The reflection coefficient is evaluated for resonance positions in Figs. 3.13 (a) and (b) for various values of f. Results for non-vanishing parallel

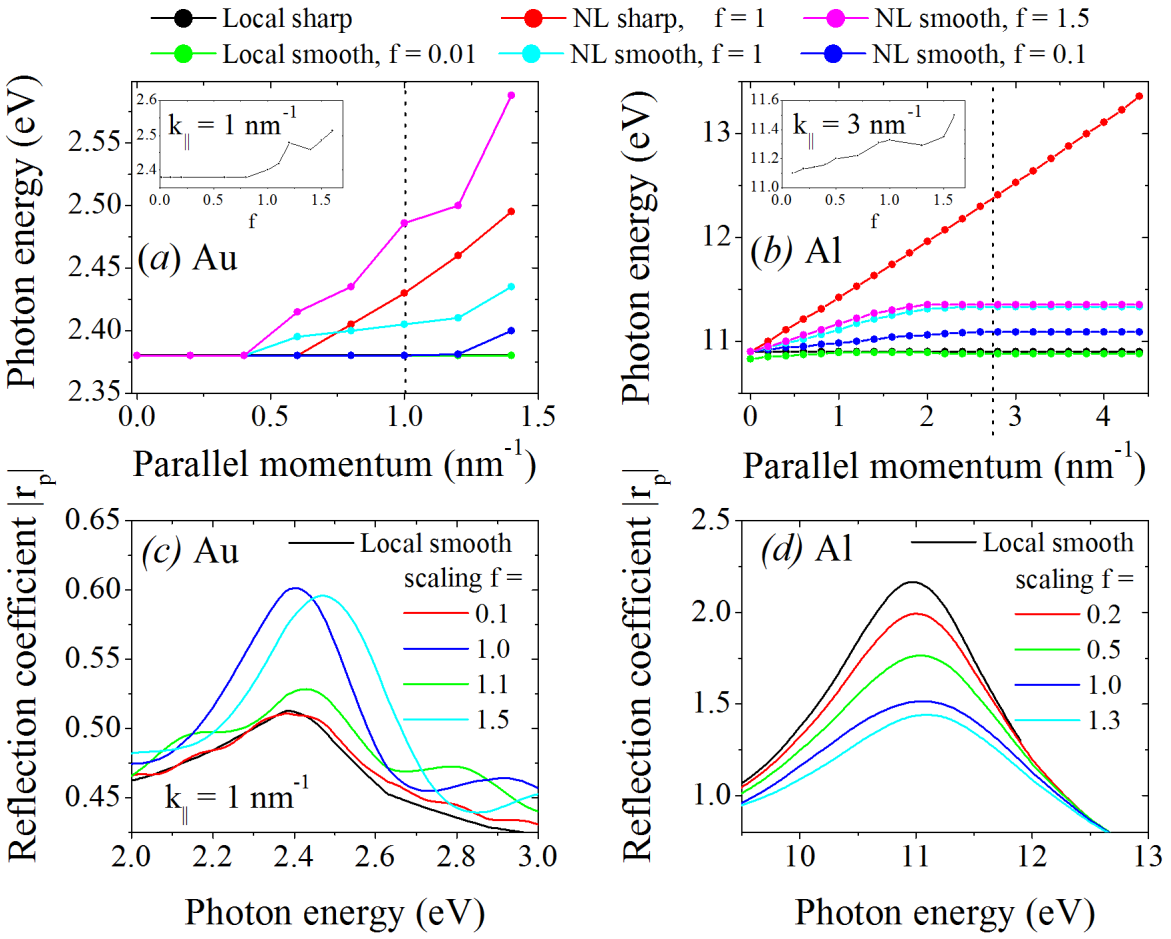

Fig. 3.13: **Transition from the NL smooth to the local smooth theory by scaling $f\beta^2 \to 0$.** For (a), (c) Au and (b), (d) Al surfaces we present (a), (b) dispersion relations for different values of f and compare the peak positions in the insets for a fixed parallel momentum of (a) $k_{\parallel} = 1$ nm^{-1} and (b) $k_{\parallel} = 3$ nm^{-1} (see dashed vertical line). Reflection peak positions of the local smooth calculations are in agreement with local sharp results. (c), (d) Reflection spectra for different values of f are given at $k_{\parallel} = 1$ nm^{-1}.

momentum beyond the local limit are presented in the insets to explicitly show the convergence towards the smooth local spectra and plasmon dispersion. For decreasing f to about 1/100, the local smooth limit is reached for both materials and peak positions in agreement with the local sharp model are found. Further augmentation of the nonlocal parameter β by scaling f yields an increasingly stronger blueshift for both materials considered, as shown in the insets of Figs. 3.13 (a) and (b).

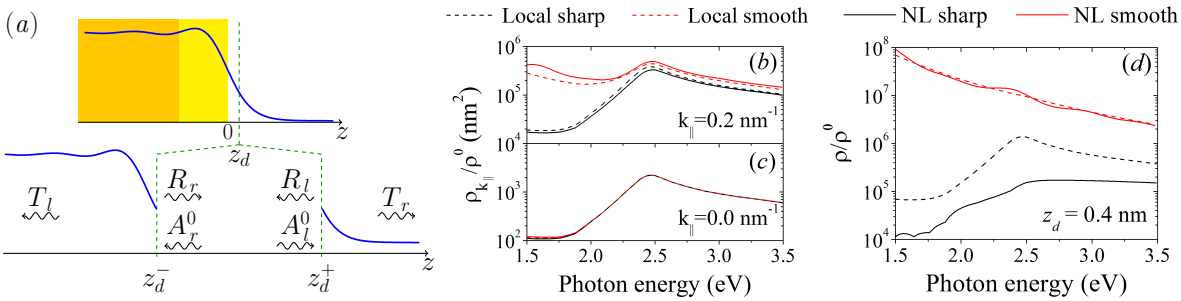

Fig. 3.14: **Local density of (optical) states (LDOS) near a metal interface.** (a) Reflection and transmission matrices involved in the calculation of the LDOS at a position z_d overlapping with the density profile. (b,c) Spectral dependence of selected $k_\parallel$ contributions to the LDOS. (d) Full LDOS obtained after integration over $k_\parallel$. Different models are considered, as shown in the upper legend. The LDOS is calculated at a distance $z_d = 0.4\,\mathrm{nm}$ relative to the jellium edge and normalized to the free-space projected LDOS ρ^0, eq. (2.26).

3.2.4 Local optical density of optical states calculations

We want to calculate the local density of optical states (LDOS) introduced in section 2.1.3 to evaluate and compare the optical properties of nonlocal smooth metal surfaces with the common local approximation. This is in particular relevant, where a molecule is placed in close proximity to a metal surface influencing e. .g its photoluminescence properties, decay rate of excited states or determining the local field enhancement exploited in biosensing, such as surface enhanced Raman scattering (SERS). First, we need to determine the electric potential at the position of the dipole emitter that we use as a field probe. With the above findings, an expression for the electric field is obtained from

$$E_z^{\mathrm{ind}}(z_d) = iq_0(z_d)B(z_d)(-\mathcal{A}_1 + \mathcal{A}_2) + k_\parallel(\mathcal{A}_3 - \mathcal{A}_4) - \left(\frac{1}{\epsilon(z_d)} - 1\right)\partial_z\phi^{\mathrm{ext}}, \tag{3.42}$$

for optical coefficients $\mathcal{A}_j$ and material parameters q_0, B defined at the dipole position z_d. Note that the external field does not enter this equation for z_d inside the dielectric region ($\epsilon = \epsilon_0 \equiv 1$), cp. appendix, section 6.4. However, the external potential is needed to compute the coefficients $\mathcal{A}_j$, as shown next.

Deriving optical coefficients

We derive the optical coefficients $\mathcal{A}_j$ from the scheme illustrated in Fig. 3.14 (a), i. e. we perform the transfer matrix calculations for the two regions $z = a \ldots z_d$ and $z_d \ldots z = b$. The corresponding two transfer matrices $T^{\mathrm{l}}, T^{\mathrm{r}}$, describing propagation just left and right from

the dipole position, obey

$$T^{\mathrm{l}}\begin{pmatrix}0\\ \mathcal{A}_2^{\mathrm{out}}\\ 0\\ \mathcal{A}_4^{\mathrm{out}}\end{pmatrix}=\begin{pmatrix}\mathcal{A}_1\\ \mathcal{A}_2^{0}\\ \mathcal{A}_3\\ \mathcal{A}_4^{0}\end{pmatrix},\qquad T^{\mathrm{r}}\begin{pmatrix}\mathcal{A}_1^{0}\\ \mathcal{A}_2\\ \mathcal{A}_3^{0}\\ \mathcal{A}_4\end{pmatrix}=\begin{pmatrix}\mathcal{A}_1^{\mathrm{out}}\\ 0\\ \mathcal{A}_3^{\mathrm{out}}\\ 0\end{pmatrix}. \tag{3.43}$$

Hereby, the amplitudes of waves propagating away from the system $\mathcal{A}_j^{\mathrm{out}}$ are not of interest. Instead, we want to find a closed expression for the internal reflection coefficients $\mathcal{A}_j$ as a function of the external dipole parameters, which are discussed later on. For T^{l} we can extract the two equations

$$R_{\mathrm{l}}\equiv\begin{pmatrix}\mathcal{A}_1\\ \mathcal{A}_3\end{pmatrix}=\begin{pmatrix}T_{01}^{\mathrm{l}} & T_{03}^{\mathrm{l}}\\ T_{21}^{\mathrm{l}} & T_{23}^{\mathrm{l}}\end{pmatrix}\begin{pmatrix}\mathcal{A}_2^{\mathrm{out}}\\ \mathcal{A}_4^{\mathrm{out}}\end{pmatrix}\equiv S_1^{\mathrm{l}}A_{\mathrm{out}}^{+}, \tag{3.44}$$

$$\begin{pmatrix}\mathcal{A}_2^{0}\\ \mathcal{A}_4^{0}\end{pmatrix}=\begin{pmatrix}T_{11}^{\mathrm{l}} & T_{13}^{\mathrm{l}}\\ T_{31}^{\mathrm{l}} & T_{33}^{\mathrm{l}}\end{pmatrix}\begin{pmatrix}\mathcal{A}_2^{\mathrm{out}}\\ \mathcal{A}_4^{\mathrm{out}}\end{pmatrix}\equiv S_2^{\mathrm{l}}A_{\mathrm{out}}^{+}, \tag{3.45}$$

thus that the reflection coefficients can be evaluated via the matrix

$$\mathcal{R}^{\mathrm{l}}=S_1^{\mathrm{l}}(S_2^{\mathrm{l}})^{-1}. \tag{3.46}$$

For T^{r} we likewise find

$$\begin{pmatrix}T_{11}^{\mathrm{r}} & T_{13}^{\mathrm{r}}\\ T_{31}^{\mathrm{r}} & T_{33}^{\mathrm{r}}\end{pmatrix}\begin{pmatrix}\mathcal{A}_2\\ \mathcal{A}_4\end{pmatrix}=-\begin{pmatrix}T_{10}^{\mathrm{r}} & T_{12}^{\mathrm{r}}\\ T_{30}^{\mathrm{r}} & T_{32}^{\mathrm{r}}\end{pmatrix}\begin{pmatrix}\mathcal{A}_1^{0}\\ \mathcal{A}_3^{0}\end{pmatrix}\equiv S^{\mathrm{r}}{}_2R_{\mathrm{r}}=-S^{\mathrm{r}}{}_1A_{\mathrm{r}}^{0}, \tag{3.47}$$

thus that the reflection coefficients can be evaluated via the matrix

$$\mathcal{R}^{\mathrm{r}}=-(S_2^{\mathrm{r}})^{-1}S_1^{\mathrm{r}}. \tag{3.48}$$

Note that a second equation for T^{r} is found, which is redundant for this study. Furthermore, the matrix inverses can be build analytically, but in practice, numerical procedures are employed at this stage.

Those reflection matrices are valid at the dipole position z_d. Neglecting the small phase shift due to small step sizes Δz, we perform multiple reflections in the interval $(z_d, z_d+\Delta z)$ to finally yield the coefficients $\mathcal{A}_j$ for the electric potential of smooth metal interfaces at the dipole position. They are given by

$$A_{\mathrm{r}}=(\mathcal{I}-\mathcal{R}_{\mathrm{l}}\mathcal{R}_{\mathrm{r}})^{-1}(A_{\mathrm{r}}^{0}+\mathcal{R}_{\mathrm{l}}A_{\mathrm{l}}^{0}),\qquad A_{\mathrm{l}}=(\mathcal{I}-\mathcal{R}_{\mathrm{r}}\mathcal{R}_{\mathrm{l}})^{-1}(A_{\mathrm{l}}^{0}+\mathcal{R}_{\mathrm{r}}A_{\mathrm{r}}^{0}). \tag{3.49}$$

This is a very handy expression entirely built upon the entries of the two transfer matrices obtained on the left and right hand side of the dipole position. It remains to determine the coefficients from the external potential, A_{l}^{0} and A_{r}^{0}.

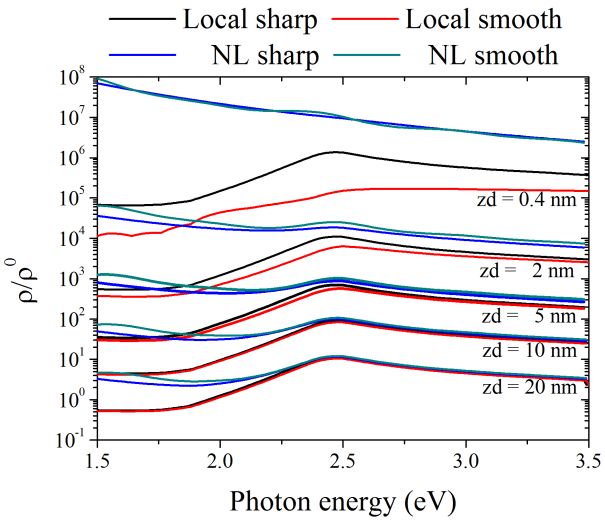

Fig. 3.15: **Local density of optical states (LDOS) near a metal interface, long distance limit.** For increasing distance z_d from the surface, we show the development of the LDOS in the different theories. All theories converge for distances of the dipole $> 5\,\mathrm{nm}$.

Contributions from the external potential

We have to bear in mind the presence of the smooth electron density in close proximity to the metal surface that we investigate. Therefore, we cannot rely on the analytical expression for the external potential, provided in the appendix for sharp interfaces, eq. (6.19). We expect nonlocal contributions to arise from this excitation in the external potential at the dipole position z_d.

For a given external charge density ρ^{ext}, the hydrodynamic framework predicts an infinitesimal change in both the electric potential and the induced nonlocal component

$$\partial_z^2\phi + k_\parallel^2\phi = -\frac{4\pi}{\epsilon_b}\rho^{\mathrm{ext}} \qquad \Rightarrow \qquad \delta\phi' = -\frac{4\pi}{\epsilon_b}, \tag{3.50}$$

$$\partial_z^2\rho + q_0^2\rho = \frac{\omega_p^2}{\epsilon_b\beta_0^2}\rho^{\mathrm{ext}} \qquad \Rightarrow \qquad \delta\rho' = \frac{\omega_p^2}{\epsilon_b\beta_0^2}. \tag{3.51}$$

Considering first a single point charge, we use the next results to obtain an expression for the dipole contribution. At the charge position, outgoing waves are of interest

$$\begin{aligned} \rho_1 &= A_2^0 e^{-iq(z-z_d)} & \phi_1 &= B\rho + A_4^0 e^{k_\parallel(z-z_d)} & (z < z_d),\\ \rho_2 &= A_1^0 e^{iq(z-z_d)} & \phi_2 &= B\rho + A_3^0 e^{-k_\parallel(z-z_d)} & (z \geq z_d). \end{aligned}$$

For a single charge at z_d, we can write the external electron density as

$$\rho^{\mathrm{ext}} = \int \frac{d^2Q}{(2\pi)^2} e^{i\mathbf{QR}}\delta(z - z_d).$$

Evaluating the continuity of ρ and ϕ and the above conditions, eqs. (3.50) and (3.51), for their first derivatives results in

$$A_1^0 = A_2^0 \qquad \Rightarrow \qquad A_3^0 = A_4^0 \tag{3.52}$$

$$iq(A_1^0 + A_2^0) = \frac{\omega_p^2}{\epsilon_b \beta_0^2} \qquad \Rightarrow \qquad A_1^0 = A_2^0 = \frac{\omega_p^2}{2iq\epsilon_b\beta_0^2} \tag{3.53}$$

$$iqB(A_1^0 + A_2^0) - k_\parallel(A_3^0 + A_4^0) = -\frac{4\pi}{\epsilon_b} \qquad \Rightarrow \qquad A_3^0 = A_4^0 = \frac{2\pi}{\epsilon_\perp k_\parallel} \tag{3.54}$$

For the dipole with two charges separated by a distance Δ, the external charge density takes the form

$$\rho^{\text{ext}} = \int \frac{d^2Q}{(2\pi)^2} e^{i\mathbf{QR}} \frac{\delta(z-(z_d+\Delta)) - \delta(z-(z_d-\Delta))}{2\Delta} \tag{3.55}$$

and we simply find the coefficients from the above by noting, that this describes a centered derivation, such that

$$\lim_{\Delta\to 0} \rho_1(z_d) = iqA_2^0, \quad \lim_{\Delta\to 0} \rho_2(z_d) = -iqA_1^0, \tag{3.56}$$

and likewise $A_3^0 \to k_\parallel A_3^0, \quad A_4^0 \to -k_\parallel A_4^0$. We therefore find the incoming waves traveling to the left and right, cp. Fig. 3.14, excited by the external, nonlocal potential

$$A_{\text{r}}^0 = \begin{pmatrix} A_1^0 \\ A_3^0 \end{pmatrix} = \begin{pmatrix} -\frac{\omega_p^2}{2\epsilon_b\beta_0^2} \\ \frac{2\pi}{\epsilon_\perp} \end{pmatrix} \qquad A_{\text{l}}^0 = \begin{pmatrix} A_2^0 \\ A_4^0 \end{pmatrix} = \begin{pmatrix} \frac{\omega_p^2}{2\epsilon_b\beta_0^2} \\ -\frac{2\pi}{\epsilon_\perp} \end{pmatrix}. \tag{3.57}$$

Note that $2\pi/\epsilon_\perp$ is the amplitude of the external potential that coincides with the local contribution of the analytics. If the dipole is being placed in the dielectric side, the nonlocal contribution of the external potential is going to be small.

We demonstrate the suitability of this approach to the LDOS of a smooth electron density profile in the limit of large distances from the surface in Fig. 3.15. Slowly increasing the distance from the surface, all theoretical models converge. While LDOS spectra calculated with the NL sharp theory begin to differ from the common local approximation for distances beneath 5 nm, both smooth description are very similar for all distances shown. We conclude from this, that nonlocal effects from the bulk material are not of importance in comparison to effects induced by the smooth electron density profile. The differences between the four presented material models become more and more apparent the closer to the surface the LDOS is evaluated. This has a crucial impact on e. g. a molecule placed close to a metal surface. The extended, smooth surface provides a broader spectrum and higher density of optical modes than what is expected from the local approximation using sharp interfaces. This is observed independently from nonlocal material properties. In contrast, a nonlocal theory using abrupt metal interfaces predicts a reduction in the LDOS due to an overall attenuation of the observed modes with increasing parallel momentum.

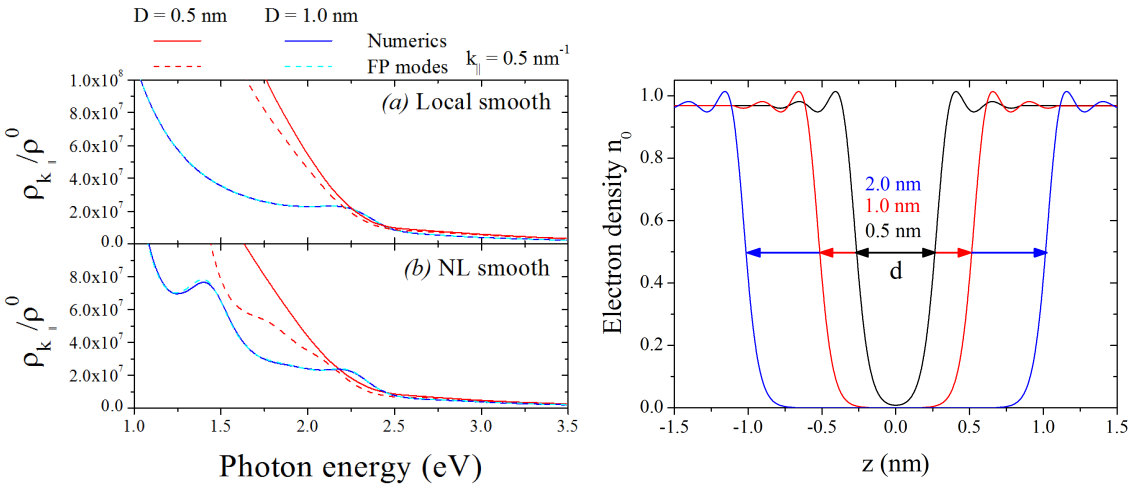

Fig. 3.16: **Dielectric gaps with smooth electron density profiles.** (a), (b) Comparing the numerical evaluation of the optical response for the gap profile with corresponding calculations for Fabry-Pérot modes for two gap distances (see upper labels). (c) Smooth gap profiles for different gap sizes demonstrating that for $d = 0.5\,\mathrm{nm}$ the density at the gap center is not completely vanished.

3.2.5 Further results and discussion

Calculations for the local density of (optical) states (LDOS) close to a metal surface are given in Fig. 3.14 (b)-(d). We show both, the $k_\parallel$-resolved LDOS contribution $\rho_{k_\parallel}(\omega)$ in (b) and (c) for two specific values of the parallel momentum, and the integrated result ρ, cf. section 2.1.3, for a dipole at a distance of 0.4 nm from the surface using ρ^0, eq. (2.26), for normalization. In particular, the case of vanishing parallel momentum (Fig. 3.14 (c)) demonstrates how all presented theories coincide in the local limit. On increasing the parallel momentum, we perceive the following trends: (i) In the nonlocal sharp theory, the increase of parallel momentum opens up additional damping channels in the longitudinal excitation which results in an overall reduction of the LDOS with increasing parallel momentum and compared to the local sharp model. (ii) In contrast, both the local smooth and nonlocal smooth show a much broader spectrum of optical states supported by the finite volume around the interface built by the smoothly changing electron density. This setup facilitates a much higher number of photonic states in layers of different depths compared to the induced surface charges in case of sharp interfaces, especially when high parallel momenta are involved. These findings are also reflected in the integrated results. On increasing the distance of the dipole from the surface, we observe a large distance limit, where again all theories start to coincide.

For dielectric gap geometries, where two facing metal surfaces are in close proximity, local theories commonly allow obtaining overall optical coefficients from the single interface coefficients considering multiple reflection paths inside the strucutre. Here, we investigate for such

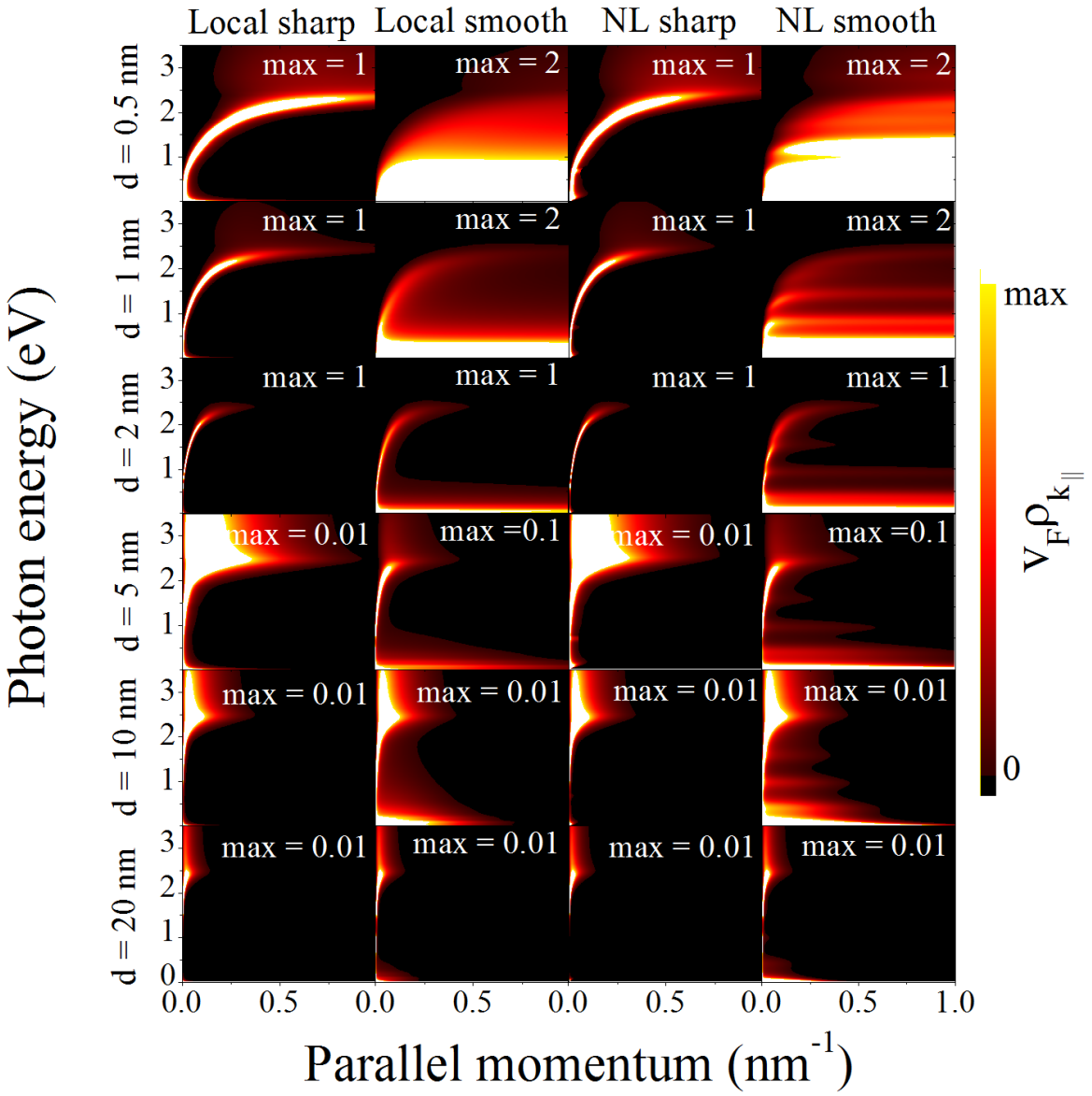

Fig. 3.17: **Plasmon dispersion relation in the gap between two gold surfaces of various sizes.** We represent the $k_{\|}$ and energy dependence of the LDOS at the centers of gaps of various separations (see left labels) for smoothly changing electron density profiles, see Fig. 3.8 (b). Different models for the response are considered, as indicated in the upper labels. These results are calculated from the Fabry-Pérot resonances in the structure using the single surface reflection for gap sizes $> 1\,\mathrm{nm}$.

a metal-insulator-metal structure with metal surfaces described by smooth electron density profiles the possibility to calculate the optical modes as obtained from a Fabry-Pérot (FP) resonator. We compare therefore the numerical calculation for the LDOS using a gap profile with modes calculated inside the composed structure as

$$r_p^{\mathrm{FP}} = \frac{2r_p e^{-k_{\|}d}(1 - r_p e^{-k_{\|}d})}{1 - r_p^2 e^{-2k_{\|}d}}, \tag{3.58}$$

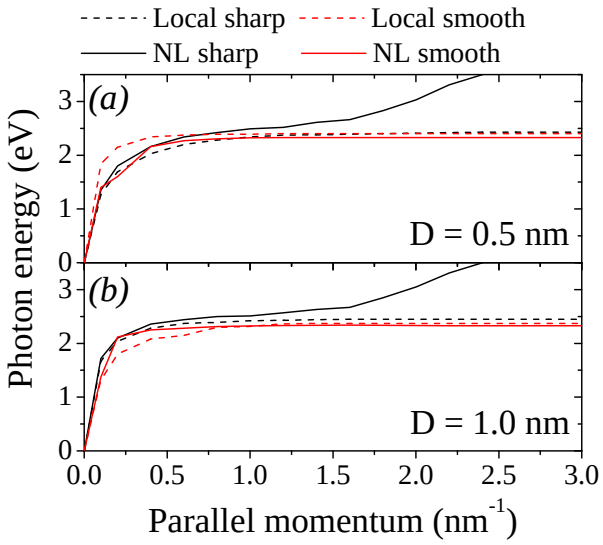

Fig. 3.18: **Direct comparison of the plasmon dispersion for dielectric gaps.** For two gap sizes, (a) $d = 0.5\,\text{nm}$ and (b) $d = 1\,\text{nm}$, we directly compare the plasmon dispersion as extracted from 3.17.

where d is the physical distance between the jellium edges and r_p is the reflection coefficient obtained from the corresponding single, smooth metal surface. In Fig. 3.16 (a) and (b), we compare spectra obtained from the numerical calculation for the gap profile and for the FP approach. Interestingly, at a distance of already 0.5 nm, we still observe slight differences between these two ways of calculating the optical response of dielectric gaps. As can be seen from the related density profiles presented in Fig. 3.16 (c), the electron density at the gap center has not yet fully dropped to zero and is thus building a conductive junction between the metal surfaces yielding different optical spectra than in the FP approach.

For a large range of gap sizes, using the FP approach of eq. (3.58), we show in Fig. 3.17 the plasmon dispersion in terms of the integrated LDOS in the different theories for increasing gap sizes. The contours show the plasmon dispersion in terms of the $k_{||}$ dependent LDOS which is multiplied to the material dependent Fermi velocity v_F of here gold to obtain a dimensionless quantity. The differences in the plasmon modes between the smoothly changing surface and the abrupt local and nonlocal theories is remarkable. Above a gap size of 5 nm the models converge as expected. Clearly, the smooth density profiles behave completely different from the sharp interfaces and effects due to bulk nonlocality loose importance. The plasmon dispersion of the two smallest gap sizes considered in Fig. 3.17 are evaluated and directly compared in Fig. 3.18. The nonlocal sharp theory predicts a strong blueshift for larger parallel momenta that is not observed in any of the other theories. In particular the nonlocal smooth model does not show this behaviour, despite nonlocal features of the bulk being incorporated.

An important question arising when studying (nonlocal) metal waveguides is the dependence of the gap plasmon with decreasing gap size, which is shown in Fig. 3.19 in terms of

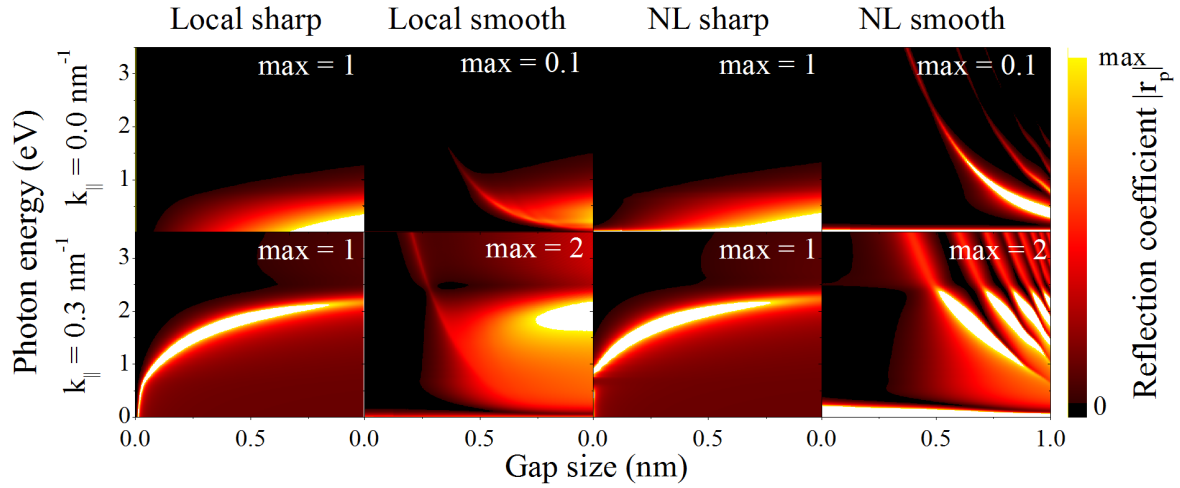

Fig. 3.19: **Gap plasmon dependence on gap size.** We represent the $k_{\parallel} = 1\,\mathrm{nm}^{-1}$ component of the LDOS as a function of gap size d and photon energy for different response models (see upper labels).

the reflection coefficient calculated in the different models as a function of the gap size at two distinct, parallel momenta of $k_{\parallel} = 0\mathrm{nm}^{-1}$ and $k_{\parallel} = 0.3\mathrm{nm}^{-1}$. We explicitely look at a regime, where both theories with sharp interfaces converge showing equal plasmon modes. While these models display a monotonous redshift with decreasing gap size as expected from the classical theory, the presented approach accounting for smooth electron density profiles show a blueshift already at vanishing parallel momenta. While the local smooth model clearly starts with a mode redshifting as in the classical theories, it exhibits a sudden blushift when the gap size decreased to about 0.5 nm. Such a mode is known from *ab initio* calculations on spherical dimers[44,80] to emerge as soon as a tunneling junction is formed. Therefore, this type of plasmon is called charge transfer plasmon (CTP). Indeed, this is the distance where we expect the electron density profiles to overlap effectively forming such a junction allowing for a plasmon mode to form that spreads across both metal regions including the gap. For the nonlocal smooth theory we find an even more dramatic change. A number of distinct blueshifting modes is observed that show a minute inner structure of maximum values overall following the monotonous redshift.

In contrast to spherical dimers,[45] where the particles have to be almost touching to emerge to a saturated plasmon mode at the common localized surface plasmon resonance (LSPR), in planar waveguides tunneling is provided not only at a finite circular intersection, but at an infinite, rectangular area. We conclude from this observation, that the blueshifted modes in planar waveguides achieve a stronger tunneling current at already lower electron densities in the tunneling junction. Therefore, the blushifted modes reach the expected saturation at the single surface SPP at larger separations of about d =0.3 nm, and are strongly broadened and attenuated for lower gap sizes.

3.3 Summary

In this first main part of the present thesis, we investigated the fundamental concept of nonlocal optical response of the free electron gas in metals. A rigorous formulation of nonlocal effects is important to provide an understanding of plasmons in nanostructured environments. However, most quantum *ab initio* methods are tedious, accompanied with vast computational effort and therefore restricted to structures involving as much as several thousand atoms.

We presented several classical routes, exploiting quantum mechancial principles and results, to obtain semi-classical wave equations for the electric field and the electron density induced at a finite surface volume. In particular, we studied spherical particles and nanoshells with the specular reflection model and the hydrodynamic model yielding extended, nonlocal Mie coefficients with direct applicability to established evaluation methods. These two parameter-free models provide a solid description of nonlocal effects and despite their very different nature, they produce similar results in the case of small structures for which retardation can be neglected. Some minor differences between both models are identified through analytics for small spheres, but the main qualitative conclusions are the same. Additionally, the hydrodynamic model allows us to simultaneously incorporate retardation and nonlocal effects, which turn out to produce important corrections in the plasmon wavelength of large particles separated by narrow gaps.

Likewise, we derived the nonlocal analogue for Fresnel's coefficients for planar structures. Again, we were able to identify simple nonlocal expressions vanishing in the local limit, that allow for a straightforward extension of known procedures. With an extension of the hydrodynamic model to account for smoothly changing electron density distributions, we can reproduce nonlocal and other effects observed in experiment and so far only predicted by first-principle methods. The presented approach uses a common transfer matrix approach to calculate optical properties of one dimensional strucutres by dividing the smoothly changing material functions at metal surfaces into a large number of slices. The impact of smooth electron density profiles and related nonlocal effects on the optical response of metallic surfaces, dielectric gaps and thin metal films was discussed in depths. We presented a range of surface and gap plasmon dispersions for varying geometrical parameters. In particular, we discuss the local smooth limit demonstrating the influence of the extension of the electron density independently of the nonlocal properties of the conduction band electrons and investigate for which conditions the local description is sufficient to describe optical resonances.

In conclusion, the main differences between the local sharp and the numerical evaluation of nonlocal smooth electron densities for different types of basic plasmonic building blocks lies within the smooth density itself and not in the influence of nonlocal phenomena in this description. Local smooth and nonlocal smooth descriptions show similarities in all investi-

gated geometries and differ significantly from the optical response found in the common local approximation and also from a nonlocal model assuming sharp interfaces. Effects of bulk nonlocality are thus counterbalanced by the smooth interface. A smooth interface, however, which can be seen from comparing the local sharp and smooth theories, leads already to plasmon quenching and broadening, but not to a shift in peak positions. Here it becomes very apparent, that additional longitudinal waves originating in the nonlocal contributions and formed by the coupling of the conduction band electrons, are the source of observed frequency shifts for SPPs at semi-infinite surfaces as well as in small dielectric gaps.

In summary, we demonstrated that the hydrodynamic model can well describe the nonlocal phenomena that arise from the quantum nature of the free electrons. It promises physical insight and rapid evaluation of systems involving nanostructures and does not involve free parameters. This study is particularly relevant for broad, active areas involving applications of local field enhancement to biosensing and nonlinear optics. Our results pave the way toward a comprehensive, computationally affordable description of nonlocality for arbitrary nanometallic morphologies.

Future research based on these findings has to involve curvilinear geometries. An adaption of the transfer matrix approach to obtain optical coefficients in the presence of smooth electron density profiles to describe radial symmetry may be readily obtained. On the other hand, adiabatic approaches using directly the results for planar structures could as well be feasible.

4 Part II - Collective phenomena

Nature, when left to universal laws, tends to produce regularity out of chaos.

(Immanuel Kant)

A regular array of particles or any structure with periodically changing refractive index can act for an incident electromagnetic wave as a periodic potential for moving quantum particles. Such a photonic crystal is characterized by its band structure for light waves by means of interference and the support of standing waves inside the crystal structure.[167] Moreover, tunable band gaps, where no propagating electromagnetic fields are sustained, allow for the controlled manipulation of light guidance in resonant, coupled modes. These modes are geometrical (lattice) resonances influenced by the surrounding medium. Changing the geometric parameters enables to adjust the resonant response, create specific near fields and thus to achieve a specified light managing result. Depending on the geometrical parameters, weak and strong coupling regimes can be distinguished, reflected in the intensity of local near-fields.[17,20,24]

In this chapter we present our work related to collective effects in regular and random monolayers of particles and discuss the following topics.

4.1.1 A regular monolayer of dielectric micrometer-sized spheres is used to achieve a nanoimprint of optical near-field patterns into a thin film via ablation through short laser pulses. We study the influence of various illumination conditions and setup parameters and the nanometer-sized imprinted features that can be realized. Our calculations using the Korringa-Kohn-Rostoker method (KKR) for regular, layered homogeneous materials show excellent agreement with related experiments.[3]

4.1.2 We discuss how to improve the performance of photovoltaic devices by exploiting plasmonic particles. Using regular particle arrays, we demonstrate total light absorption in the Salisbury screen setup translated into the visible spectrum and an overall improvement of the absorption by up to 20%. This study is done analytically to a large extent allowing for rapid evaluation of different material compositions and geometrical setups.[2]

4.2.2 Scattering enables thin film technology by increased optical path lengths inside the solar cell structure. This also allows random particle layers to become competitive, where strong coupling is difficult to achieve on a large scale, but light scattering is supported over an even broader spectral range than in case of an ideal, regular particle array. In related experiments, scattering effects (weak coupling) rather than collective resonances

(strong coupling) are exploited. The developed theory to describe the optical response of random nanoparticle layers uses statistical data of the particle size distribution of fabricated samples to set up comparable numerical, quasi-random samples. A generally good description of optical properties is thus provided.[5,6,100]

For random particle layers, the particle size distribution and statistical characteristics for cost efficient, self-assembled samples rather then lattice parameters allow for tuning resonances. Both approaches exhibit unique advantages and disadvantages, which we discuss in the forthcoming sections.

4.1 Regular particle arrays

Thanks to advanced fabrication techniques, e. g. electron beam lithography (EBL) or deposition of colloidal suspensions, regular particle arrays can be fabricated with nanometer resolution and a high degree of control over the shape, size, pitch and position of the desired particles.[24,100] These techniques further provide good reproducibility and timely production processes. The systematic study of the influence of parameters in the arrangement and composition of such layers is thus enabled and allows for adjusting the optical properties to some extent. Particle arrays usually show narrow spectral resonances with strong local field enhancement. They are efficient subwavelength scatterers and can interact with light from a large angular range. With such optical properties, particle arrays are attractive elements for a wide range of photonic applications and optical engineering.[18,22,103]

4.1.1 Imprinting optical near-fields of colloidal dielectric monolayers

The amorphous state of the material $Ge_2Sb_2Te_5$, commonly known as GST, can be induced through laser irradiation from the crystalline face-centered cubic (fcc) material, effectively mapping complex intensity patterns for varying illumination conditions with great detail.[168–171] We explore in this section the near-field nanopatterning obtained by irradiation of hexagonal monolayers of micron-sized polystyrene (PS) spheres on photosensitive, chalcogenide $Ge_2Sb_2Te_5$ (GST) films. Several patterns are produced demonstrating the uniqueness of each of them under changes of the illumination conditions, as well as the size of the spheres and even rotations of the hexagonal lattice with respect to the horizontal axis, see Fig. 4.1 (e). Multiple scattering effects and particle interaction are an important aspect to describe the resulting patterns[172] and in particular to explain the observed robustness of the imprinted patterns even in the presence of small misalignments or imperfections of single colloids in this monolayer of touching particles. This method enables the design and experimental verification of patterns with multiple focii per particle and complex shapes, which can be directly implemented for large scale fabrication on different substrates. Recent FDTD simulations for periodic boundary conditions in a Si particle monolayer have been used to identify optimum

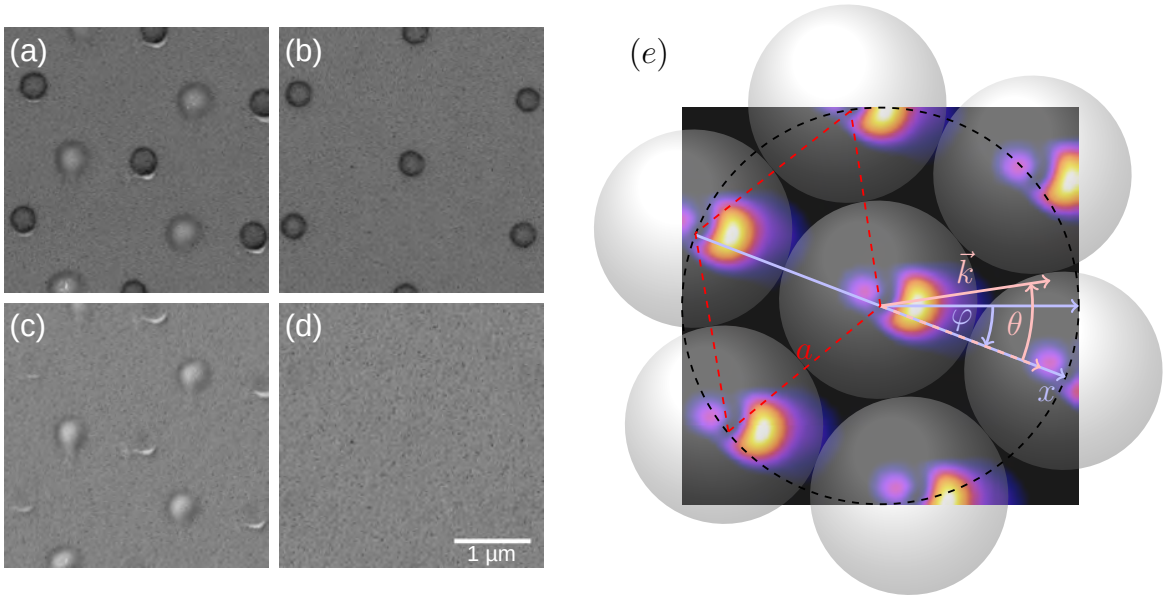

Fig. 4.1: **SEM images of irradiated (a,c) and pristine (b,d) regions.** Images in the upper (lower) part were recorded using the inlens detector (a sideways detector for secondary electrons). (e) Schematic of a colloidal dielectric monolayer and its imprinted optical near-field. The calculated pattern assumes a p-polarized incoming field with $\lambda = 900$ nm, $\theta = 29.5°$ and a lattice rotation of $\varphi = 21.0°$. The particle size and lattice parameter are $a = 1730$ nm (touching particles regime).

particle array and irradiation parameters for maximum field enhancement at the substrate surface near the contact point with the particle.[173] Chalcogenide phase-change substrates, such as GST, are used to record and subsequently image the near-field light intensity with subwavelength resolution.[168] Engineered structures exploiting the focal points of the colloids become realizable in practice by angular beam scanning.[174]

Experiments on colloidal dielectric monolayers

Experiments were performed by Paul Kühler and Jan Siegel at the Instituto de Óptica (CSIC) in Madrid, Spain. Our simulated setups are in agreement with measured characteristics of the samples, in particular the lattice rotation and illumination settings, see Fig. 4.1 (e). The laser beam was focused onto the sample at an angle of incidence $\theta = 52.2°$ adjusted to $\lambda = 799$ nm. A single pulse was selected from a 100 Hz pulse train by means of an electromechanical shutter to irradiate the targeted area. The particles themselves are either pulled off the surface on laser irradiation for high enough fluences or removed with a scotch tape. The phase transition induced is also accompanied by a change in material density, topography, and electric conductivity, which makes SEM a suitable high-resolution read-out technique.[175] Experimental images, see examples in Fig. 4.1, were taken in-situ with an inlens SEM mode detector, which allows for a precise determination of the particle postions as dark spots. Images acquired with the inlens detector (Fig. 4.1 (a) and (b)) clearly show the

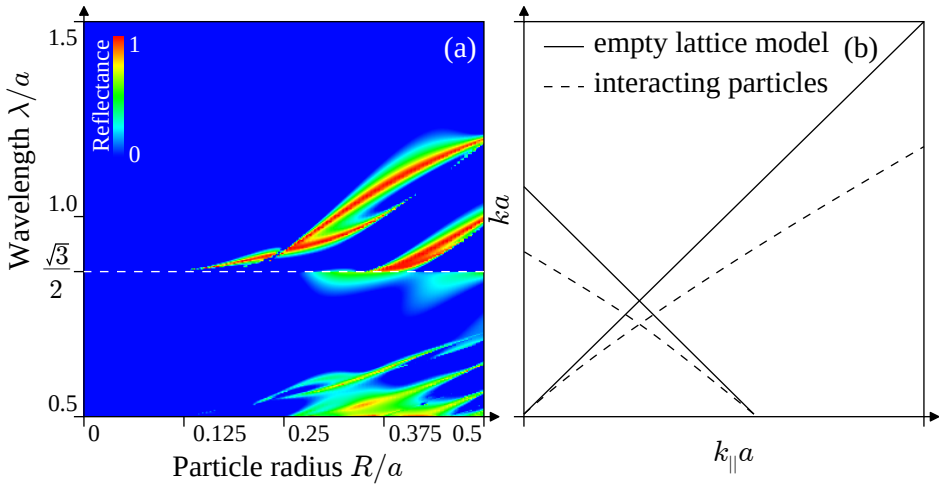

Fig. 4.2: **Differences between the calculated band structures of *empty* and *filled* lattices.** (a) Reflectance of a hexagonal lattice as a function of wavelength and particle radius, both normalized to the lattice parameter. The minimum value for a hexagonal lattice at $k_{||} = 0$ is $|ka| \geq 4\pi/\sqrt{3}$ (white dashed line). (b) Characteristic band structure for empty (solid lines) and filled (dashed lines) lattice models in comparison.

former contact points of the PS particles with the GST substrate. This allows identifiying the positions of the particles in the hexagonal array. In contrast, a sideways detector for secondary electrons (Fig. 4.1 (c) and (d)) enables us to analyze the imprinted nanostructures independently of the contact positions. In the following, calculated graphs contain the contact points as grey circles for better orientation and light is incident from the left in all presented figures.

The complex index of refraction $(n + i\kappa)$ of the involved materials at the experimental laser wavelength is summarized in table 6.2. Closed-packed monolayers of spherical polystyrene (PS) particles with different diameters were self-assembled on a water surface and then deposited onto the substrate. An illustration of the setup is given in Fig. 4.1 (e). Given their large Mie parameter $\frac{2\pi}{\lambda}\frac{n_{PS}d}{2} \gg 1$, each particle produces collimating lensing, involving the participation of many multipoles up to a high order. In the touching particle regime, we assume the lattice constant to be equal to the particle size which allows measuring the center-to-center distance in the experimental setups rather than extracting directly the particle diameter.

Theoretical aspects

We perform multiple scattering calculations using a layer-KKR method[148–150] for periodic particle arrays on top of a GST substrate. Properties of the regular lattice in the reciprocal space are exploited to yield a rapid evaluation of the optical properties of the system under consideration. The simulations are converged with respect to both the number of multipoles $l_{\max}$ used for each sphere and the number of reciprocal lattice vectors $g_{\max}$ in the layer-substrate coupling. Those calculations lead to a great agreement with the imprinted near-field

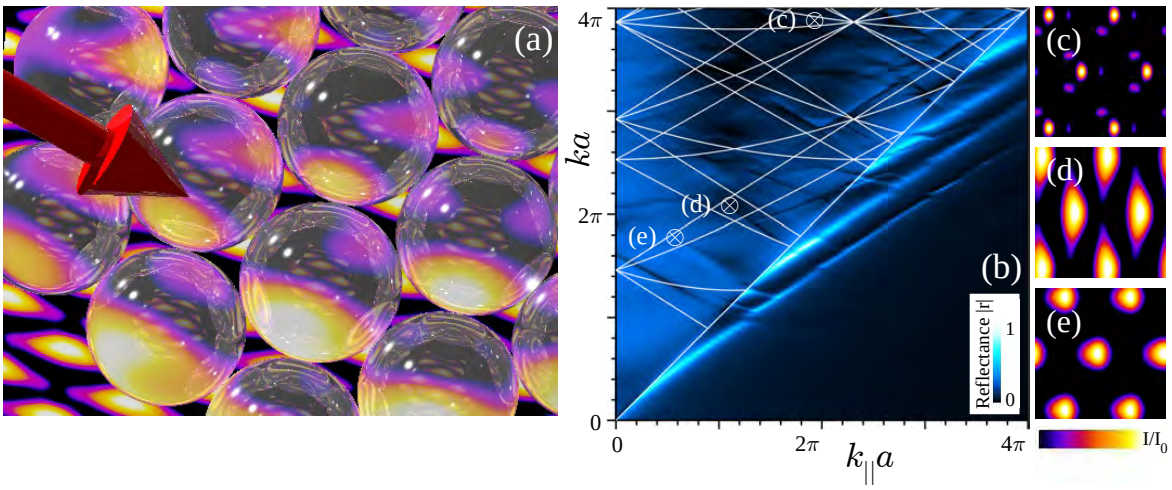

Fig. 4.3: **(a) Hexagonal lattice of polystyrene spheres with an underlying calculated near-field pattern, which is imprinted into a GST substrate.** The calculation details are as in (d) (see below). The incident light is p-polarized and has wave vector along a nearest-neighbours bond direction, $\varphi = 0°$. (b) Dispersion diagram showing the reflection coefficient $|r|$ of a closed-packed monolayer of polystyrene spheres on an fcc GST planar substrate. (c)-(e) Near-field associated with specific points in the dispersion diagram for $a = 817$ nm (see corresponding symbols in (b)). Wavelengths and angles of incidence used: (c) $\lambda = 409\,\text{nm}$, $\theta = 40.8°$; (d) $\lambda = 799\,\text{nm}$, $\theta = 52.2°$; (e) $\lambda = 925\,\text{nm}$, $\theta = 30.0°$.

patterns found for various fabricated samples as discussed in the next sections. Additionally, we present analytical calculations of the band structure that mark the resonant modes of the structure in the limit of small particles (*empty* lattice model), which we briefly discuss here.

The lattice constant is denoted a and the tilt against the x-axis is φ, which we identify with the lattice rotation with respect to the plane of incidence, see Fig. 4.1 (e). The real space lattice vectors for a hexagonal lattice with $\alpha = 60°$ and calculated from those the unit cell vectors in reciprocal space are

$$\mathbf{a}_1 = a\begin{pmatrix}\cos\varphi\\ \sin\varphi\end{pmatrix},\ \mathbf{a}_2 = a\begin{pmatrix}\cos(\varphi+\alpha)\\ \sin(\varphi+\alpha)\end{pmatrix},\ \mathbf{g}_1 = \frac{2\pi a}{V}\begin{pmatrix}\sin(\varphi+\alpha)\\ -\cos(\varphi+\alpha)\end{pmatrix},\ \mathbf{g}_2 = \frac{2\pi a}{V}\begin{pmatrix}-\sin(\varphi)\\ \cos(\varphi)\end{pmatrix},$$

which span the reciprocal space with in-plane vectors $\mathbf{G}_{nm} = n\mathbf{g}_1 + m\mathbf{g}_2$.

The *empty* lattice band structure is given by the resonance condition $|\mathbf{k}_{||} - \mathbf{G}_{nm}| = |\mathbf{k}|$. The band structure inside a homogeneous material of permittivity ϵ results upon choosing $k = \sqrt{\epsilon}\,\omega/c$. With $\mathbf{k}_{||} \equiv 0$, this leads to a minimum at $|ka| \geq \frac{4\pi}{\sqrt{3}}$ for bands of lowest order above the light line. This is indicated in Fig. 4.2 (a) by the white, dashed line, and in the band diagram in Fig. 4.3 (b) by the $\mathbf{k}_{||} = 0$ starting point of the lowest order bands.

Further differences in the numerical and analytical calculations of the band structure presented in Fig. 4.3 (b) originate in two more aspects. (i) The numerical calculations incorporate the asymmetric environment (i.e. a GST semi-infinite substrate vs. an infinite homogeneous medium, respectively). (ii) The numerical calculations account for multiple scattering effects

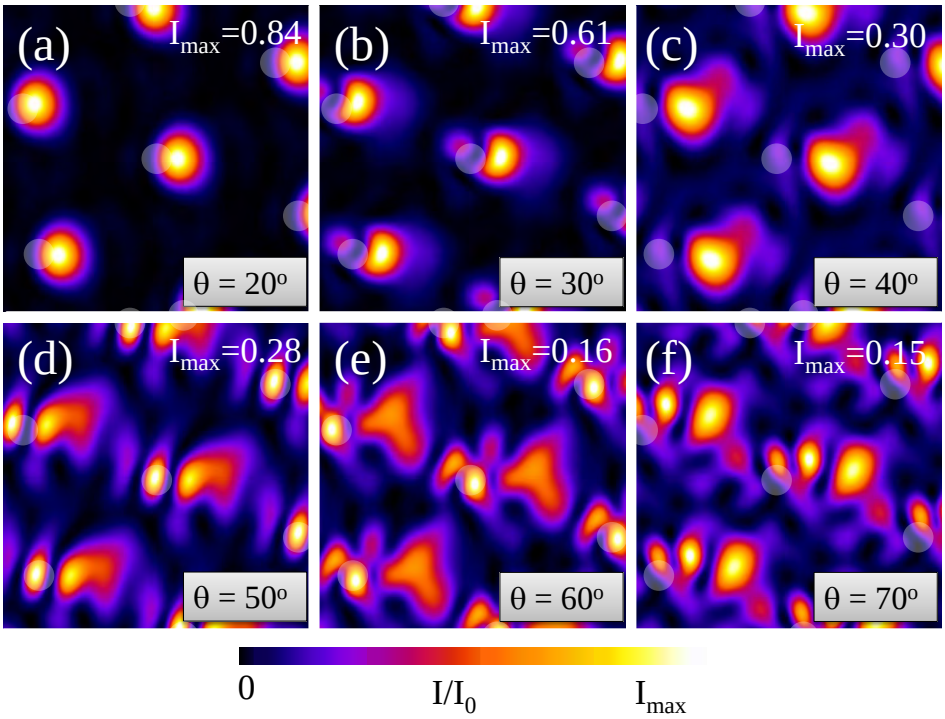

Fig. 4.4: **Imprinted near-field intensity calculated for increasing angles of incidence** with fixed azimuthal sample lattice rotation $\varphi = 21°$, particle size $a = 1730$ nm, and p-polarized light of wavelength $\lambda = 900$ nm. Gray circles signal particle positions. The maximum of intensity beneath the GST-air interface is given in each figure, while the color scale is normalized as indicated in the lower color bar. The imprinted intensity drops for increasing inclination.

among the particles. The latter is illustrated in Fig. 4.2 (b). Figure 4.2 (a) shows the reflection of the monolayer as a function of particle size, indicating a range of particle sizes for which multiple-scattering becomes relevant and where, on the other hand, the empty lattice calculations are valid.

Results and discussion

Figure 4.3 (b) shows the calculated band diagram for a hexagonal PS sphere monolayer on crystalline GST. The upper triangular region above the light line ($k = \frac{\omega}{c} n_{\mathrm{PS}} \equiv k_{\|}$) allows us to identify configurations of particle diameter a (equal to the lattice spacing in the closed-packed structures), incident wavelength $\lambda = \frac{2\pi}{k}$, and incidence angle (related to the parallel wave vector through $k_{\|} = k \sin\theta$) associated with resonant optical modes, where high local field enhancement is expected. Incidentally, the kinematical small-particle bands given by $|\mathbf{k}_{\|} - \mathbf{G}_{nm}| = k$, superimposed curves in Fig. 4.3 (b), differ from the numerical bands due to inter-particle interaction for the previously discussed reasons.

Unique near-field patterns are achieved when changing the system parameters, shown for selected points of the disperison diagram Fig. 4.3 (c)-(e), clearly illustrating the large sensitivity of the imprinted structures to geometrical and illumination parameters. This allows a

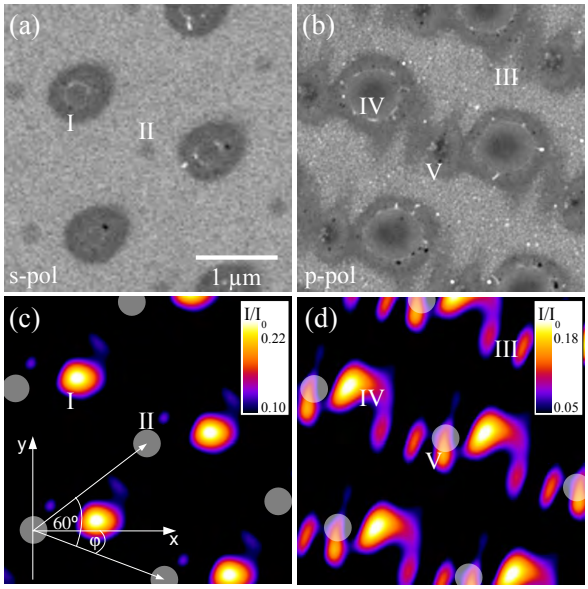

Fig. 4.5: **Influence of incident light polarization on the imprinted near-field** for $\lambda = 799$ nm, $a = 1704$ nm, and $\theta = 52.2°$. Gray circles in the calculated graphs indicate the sphere-substrate contact points. Measured SEM images (a), (b) are compared with theory (c), (d) for the following parameters: (a), (c) *s*-polarization, and lattice rotation $\varphi = 22.3°$ (see inset to (c)); (b), (d) *p*-polarization, $\varphi = 20.6°$.

rich variety of patterns to be created that display the periodicity of the colloidal monolayer mask. Notice that the change in the particle size-to-wavelength ratio of the patterns shown in Fig. 4.3 varies the complexity of the near-fields.

In Fig. 4.4 we compare simulations for fixed azimuthal sample orientation, increasing the angle of *p*-polarized light incidence. The imprinted intensity drops, but it also acquires a more complex structure, presumably due to the involvement of a richer structure of modes, as observed in the band diagram of Fig. 4.3 (b) with increasing $k_{\parallel}$.

Additionally, pattern complexity is influenced by the incident-light polarization, see Fig.,4.5. The upper panels show measured SEM images of structures created with a single laser pulse at an angle of incidence of 52.2°. The dark spots at position II in Fig. 4.5 (a) indicate small modifications of the GST surface that result from adsorbants deposited at the PS spheres contact region. In contrast, the dark regions with a brighter circle inside (position I) are a direct result of irradiation. By comparison with optical micrographs, the observed modifications of the GST film can be attributed to amorphization of the otherwise crystalline film (outer ring) and ablation (enclosed by the bright rim).[175]

A further relevant experimental parameter is the lattice orientation angle φ relative to the light incidence direction (see inset of Fig. 4.5 (c)). Regions of similar orientation φ were selected in Fig. 4.5, so the main differences between panels (a) and (b) is the light polarization (*s* and *p*, respectively). While displaying only a simple elliptically shaped maximum at I for *s*-polarization, the imprint is more complex for *p*-polarization. Beside the main maximum

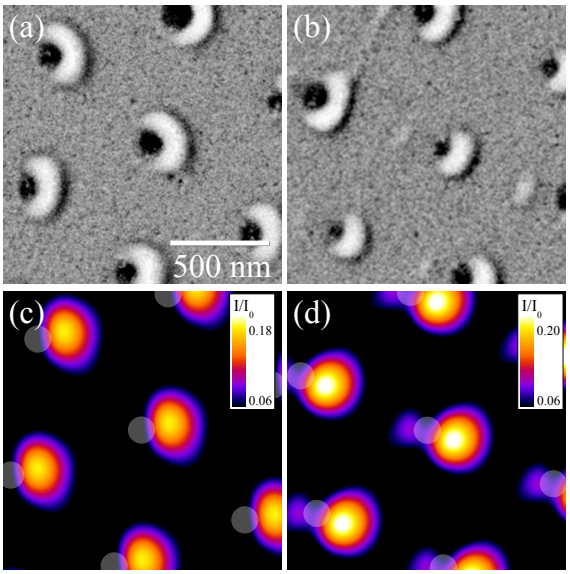

Fig. 4.6: **Influence of lattice rotation φ on the imprinted near-field** for $a = 817$ nm and p-polarized light incident with $\lambda = 799$ nm and $\theta = 52.2°$. Gray circles signal contact points in the calculated images. Measured SEM images (a), (b) (acquired with a sideways detector that is insensitive to the contact-point surface modifications) are compared with theory (c), (d) for $\varphi = 41°$ in (a), (c) and $\varphi = 23°$ in (b), (d).

at IV, which is still well pronounced, several less intense features are revealed (see III), including an auxiliary maximum at the contact point V, which cannot be observed for s-polarization. The remarkable modifications observed in the spatial patterns when the light polarization is changed can be traced back to the involvement of several array modes for any given light frequency and direction of incidence. Their excitation strongly depends on the orientation and amplitude of the in-plane electric field vector of the incoming light, see Fig. 4.3 (b). Essentially, different polarizations couple with different strengths to these modes, thus producing different spatial patterns. A similar explanation applies to the variations with angle of incidence (Fig. 4.4) and the lattice rotation that we discuss next.

The lower panels in Fig. 4.5 depict our corresponding calculations with grey circles superimposed to indicate the positions of contact points. The agreement between theory and experiment is good. In particular, the occurence of multiple local maxima as well as their detailed shape and position is well reproduced in the calculations. As indicated in Fig. 4.3 (c), the number of near-field maxima is not limited by the number of particles and can exceed it depending on the laser polarization.

The dependence on the lattice orientation relative to the projected light incidence direction (angle φ) is discussed in Fig. 4.6. The left (right) side corresponds to $\varphi = 41°$ ($\varphi = 23°$). Symmetry is reduced with respect to the horizontal axis and significant differences between both of them are observable in the detailed shape of the position of the near-field maxima relative to the spheres.

We want to emphasize that the intensity patterns produced by a colloidal monolayer cannot

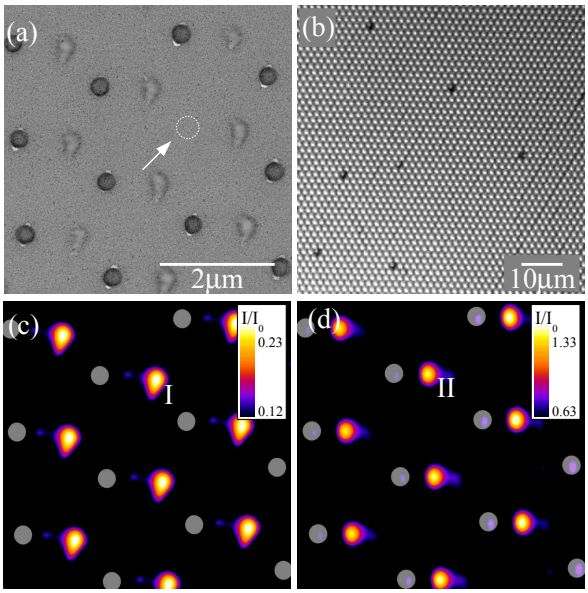

Fig. 4.7: **Observation of an imprinted pattern imaged with a SEM inlens mode detector.** The sample and illumination parameters are $\lambda = 799$ nm, $a = 1730$ nm, $\theta = 52.2°$, p-polarization, and $\varphi = 26.4°$. (a) The single lattice defect is marked by an arrow. No perturbation in the imprinted near-field pattern is observed. (b) Optical microscopy image of a different, larger region of the same monolayer before irradiation, showing the presence of single defects (vacancies). (c) Multiple-scattering calculation of the corresponding full lattice (no defect). (d) Simple superposition model.

be described by a simple superposition of patterns produced by single spheres, without considering particle interactions. To demonstrate this, we have performed an experiment using conditions for imprinting a relatively simple pattern (Fig. 4.7 (a)), which we compare with calculations both for the multiple scattering method noted above (Fig. 4.7 (c)), as well as with a simple superposition of the scattered field of each individual particle[168] (single scattering, Fig. 4.7 (d)). The latter was carried out for a hexagonal lattice of 11×11 particles, neglecting collective effects such as multiple scattering from neighboring particles. This superposition model does not reproduce the position of the dominant intensity maxima, which are predicted to lie much closer to the contact points than found experimentally. At the same time, the multiple scattering model predicts a distance between maxima and contact points that is in agreement with experiment. Notice that the contact points are more pronounced here than in Fig. 4.5, presumably as a result of slightly varying conditions during sample preparation. Furthermore, the intensity maxima calculated with the superposition model display considerably different shapes and amplitudes with respect to those measured in Fig. 4.7 (a) or calculated with the full model. This demonstrates that the patterns produced cannot be explained by simple interference of incoming and scattered light because each particle reacts to significant field contributions originating in scattering from its neighbors.

A remarkable feature can be observed in Fig. 4.7 (a): the absence of a single contact

point (at the position marked by a dashed circle), indicating that the particle at this position might have been missing in the monolayer during illumination. Such lattice defects in form of vacancies are frequently observed in colloidal monolayers, as shown in Fig. 4.7 (b). Despite this defect, the imprinted pattern in Fig. 4.7 (a) features the corresponding main maximum next to the defect, just as if there was no defect. We speculate that the strong collective interaction between the particles might render the optical response of the monolayer robust against the presence of lattice defects, featuring collective photonic crystal-like properties. Yet, we cannot exclude the possibility that the defect was not a vacancy but a particle slightly elevated above the substrate, thus not forming a contact point but contributing in a slightly different way to the optical response. Nonetheless, both explanations imply that the imprinted patterns are not too sensitive to small displacements and structural defects of the colloids. Further analysis of the degree of tolerance against monolayer defects is still needed.

4.1.2 Enhanced photovoltaics with regular plasmonic structures

We introduce the reflection and transmission coefficients of a particle array in the dipolar approximation and derive fully analytical solutions for the absorption of a simplified photovoltaic device consisting of the particle layer embedded in a (either absorbing or non-absorbing) material at some distance above a metal substrate and demonstrate that 100% absorption for a range of geometrical, angular and spectral parameters is achievable. Both electric and magnetic contributions to the optical response of the particle array are considered. An enhancement of the mean absorption in comparison to a bare Si substrate of up to 20% is found. The presented approach readily allows rapid evaluation of different geometrical and compositional parameters.

To achieve total light absorption, we use a Salisbury screen setup,[176,177] which was originally designed for enhancing radio frequency waves by placing a thin absorbing screen in front of a perfectly conducting plane. It was previously shown that this configuration allows total absorption in the visible spectrum for a layer of graphene discs[145,178] and in metamaterials.[179,180] A realization with a Si or Ag nanoparticle array, replacing the thin sheet in the original idea, is investigated here, see Fig. 4.8 (a). In this configuration, the absorption efficiency is enhanced in the visible for suitable conditions of the geometrical parameters of the particle array.

The unique properties and high tunability of plasmonic particle arrays enable strongly increased light-matter interaction and boost the absorption efficiency of photovoltaic devices. We develop step by step the optical response coefficients for a particle layer and the complete setup. First we study the conditions required to achieve total absorption and explain the assumptions made in the analytical approach and the resulting range of suitable parameters. We develop analytical expressions for the optical response of a metal particle array in terms of its reflection and transmission coefficients and compare our results to higher-order numerical calculations,[150] resulting in excellent agreement within a given range of particle size and

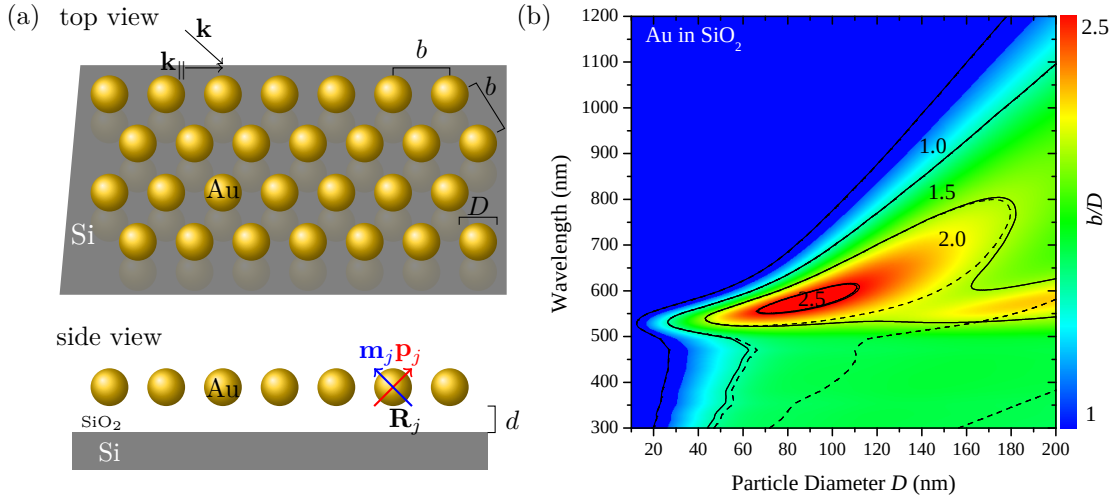

Fig. 4.8: **(a) Top and side view illustrating the investigated Salisbury screen for photovoltaics.** A hexagonal particle layer of lattice constant b embedded in SiO_2, Si or GaAs is placed at some distance d above a substrate. Each particle j at position R_j is contributing with its electric and magnetic dipole moments $\mathbf{p}_j$ and $\mathbf{m}_j$ to the optical response of the particle array. (b) Spectral regions where total absorption is possible for a hexagonal Au particle array in SiO_2 is shown as a function of the particle diameter D. The normalized, effective lattice parameter b/D is depicted with contours indicating analytical (dipolar, dashed) and numerical (multipolar, $l_{\max} = 10$, solid) calculations showing a wide range of regions with possible high absorption (i. e. satisfying the condition $b/D > 1$).

interparticle distance. Contributions from magnetic moments can not be neglected (e. g. in Si[181]), and expressions are derived with both electric and magnetic dependencies. In the limit of non-magnetic materials, the angular dependence is additionally studied, see appendix, section 6.5 for details.

Conditions for total absorption

First, we analyze for which geometrical parameters total absorption is possible. We consider particles of diameter D, made of different materials, that are arranged in a hexagonal lattice with center-to-center distance b, cp. Fig. 4.8 (a). Total absorption can be expected where the geometrical cross section of the particle array is exceeded by its optical, absorption cross section, see eq. (2.9). In particular, we study the dipolar absorption cross section including magnetic effects

$$\sigma_{\text{ext},1}(\omega) = 4\pi k \sqrt{\epsilon}\, \text{Im}(\alpha_1^E + \alpha_1^M). \tag{4.1}$$

We use complex dielectric functions based on experimental, wavelength-dependent data for GaAs and Si as summarized in table 6.2. The optical response of the particles is given by their dipolar polarizability α_1^ν, with different contributions from electric ($\nu = E$) and magnetic ($\nu = M$) response. We determine the corresponding lattice parameter b, assuming a hexagonal

lattice, from comparison with the corresponding geometrical cross section $\sigma_{\text{geo}} = \frac{\sqrt{3}}{2}b^2$. In spectral regions with an effective lattice parameter $b/D > 1$, total absorption is expected under physically realizable geometries.

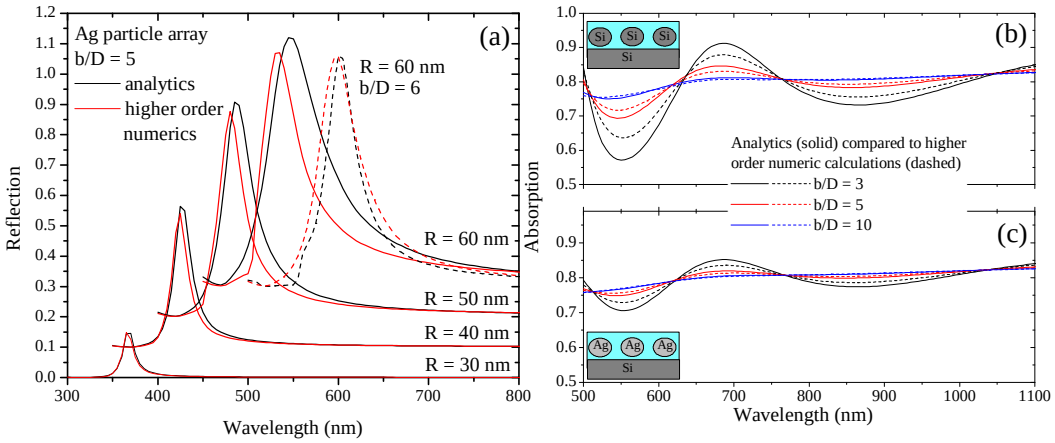

Fig. 4.9: **Comparison of our analytical dipolar approach to higher-order numerical calculations.** (a) For a fixed effective lattice parameter, we show the emerging discrepancy in the description of the reflection coefficient of Ag particle arrays for increasing particle diameter. Larger particle diameters need increased b/D ratios to converge with the all-multipoles numerical calculations (dashed curves). (b) The absorption of Si and Ag particle arrays above a Si substrate is given for different effective lattice parameters b/D. For the array to be physically realizable, the relation $D < b$ has to be satisfied. For $b/D \geq 5$ the results are sufficiently converged.

In Fig. 4.8 (b), we evaluate the effective lattice parameter obtained for dipolar analytical (dashed curves) and all-multipoles numerical (solid curves) calculations. The dipolar approximation used for the analytical model enables rapid evaluation of various device compositions. However, we have to restrict ourselves to wavelengths above $\lambda \geq 500$ nm and particle diameters below $D \leq 120$ nm to ensure that our results coincide with equivalent numerical simulations. The optical cross section in dipolar approximation is compared to cross sections computed numerically,[150] using a higher angular momentum number ($l_{\text{max}} = 10$) to assess the quality of the approximations used in our approach, shown in Fig. 4.9. The analytical results converge towards the numerical simulations for the appropriate parameters.

For photovoltaics applications, this particle size regime yields optimum scattering properties, and absorption is mostly due to ohmic losses.[119] To emphasize this, we calculate the albedo (scattering cross section over total cross section) for the materials considered here in Fig. 4.10 (c) for two particle sizes in this regime. Fig. 4.10 (a) shows the absorption at the substrate enabling us to identify the positions of absorption at the particle layer for solid Au particles and Au nanoshells in SiO_2. The solid particles absorb below 550 nm, whereas this spectral position can be tuned by particle size, shape and composition, as is shown for an array of Au nanoshells. Total absorption around the resonant wavelength of the particle array is easily achieved, but is subject to direct absorption of the particles. It is therefore important to investigate, how nanoparticle layers can be exploited to achieve total absorp-

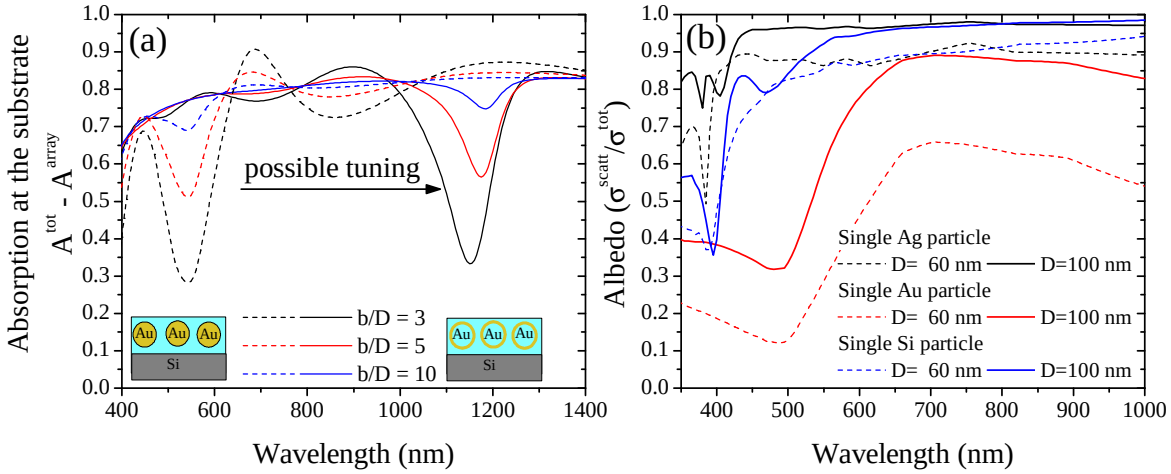

Fig. 4.10: **Basic properties of the materials under consideration.** (a) Absorption at the substrate for two representative systems. The spectral range between solid Au particle arrays and Au nanoshells, here both above a Si substrate, can be exploited by tuning the particle size and shell thickness, respectively. The particle diameter is $D = 60\,\text{nm}$, and the distance between the substrate and the particle array is chosen $d = 500\,\text{nm}$. (b) Albedo for Ag, Au and Si particles for two sizes. Ag and Si particles are very efficient scatterers. However, for smaller particles ohmic losses determine the absorption. Resonant particle absorption is found below 550 nm.

tion beyond the resonance of the nanoparticles, ensuring that light at higher wavelengths is directly absorbed in the active material.

Analytical expressions for the reflection of a particle array and the absorption in the composite device are derived and we demonstrate high absorptivity beyond particle absorption.

Derivation of electric and magnetic dipole moments

We introduce the reflection and transmission coefficients of a particle array in the dipolar approximation including contributions from both magnetic and electric dipole moments under normal incidence conditions, as introduced in section 2.2.3. In the case of nonmagnetic materials, the presented theory can be readily extended to include angular dependence for different polarizations[145] which is discussed in the appendix 6.5.

We assume a single layer of a hexagonal lattice of identical particles, where each particle j contributes to the optical properties of the array with its individual magnetic and electric dipole moments $\mathbf{p}_j = p_j \mathbf{e}_x$ and $\mathbf{m}_j = m_j \mathbf{e}_y$. Thus the self-consistent solution for the dipole moments of the whole particle array, derived from eqs. (2.28) and (2.29), reads

$$p = \frac{E^{ext}(\frac{1}{\alpha^M} - G) - HH^{ext}}{(\frac{1}{\alpha^E} - G)(\frac{1}{\alpha^M} - G) + H^2}, \tag{4.2}$$

$$m = \frac{H^{ext}(\frac{1}{\alpha^E} - G) + HE^{ext}}{(\frac{1}{\alpha^E} - G)(\frac{1}{\alpha^M} - G) + H^2}. \tag{4.3}$$

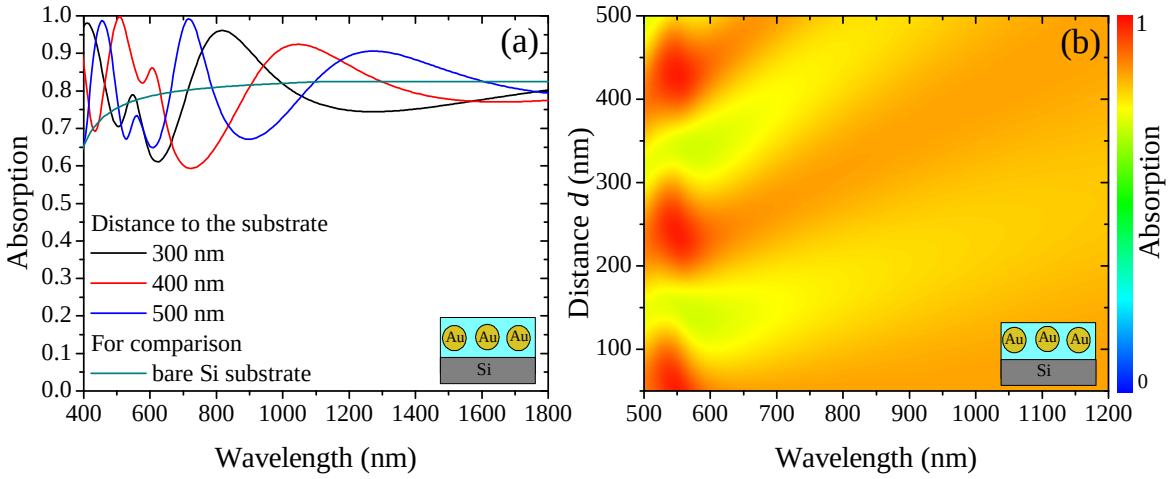

Fig. 4.11: **Comparing absorption of a Salisbury screen configuration with bare a Si substrate.** (a) The absorption of Au particles on Si is shown for different distances between the particle array and the substrate. The particle size is $D = 100\,\text{nm}$ and the effective lattice parameter is $b/D = 3$. An optimum distance for each wavelength exists. (b) Complete contour plot of the absorption as a function of the distance d for this device.

We obtain $G = G^{\text{EE}} = G^{\text{MM}}$ and $H = G^{\text{ME}} = -G^{\text{EM}}$ (cp. eq. (2.31)) via the evaluation of lattice sums after the method of Kambe,[182] where G takes the analytical form

$$G_{jj} = \frac{g_{jj}}{b^3} + \frac{2\pi i}{Ak_z}(k_\parallel^2 - k_j^2) - i\frac{2k^3}{3}, \tag{4.4}$$

with the unit cell area A. The real part $g_{jj} = b^3 Re(G_{jj})$ remains to be determined by the lattice sum procedure, see appendix 6.5.

Reflection and transmission coefficients

The total scattered field is determined by using the limit of the Green's function, cp. eq. (2.32),

$$G = \lim_{\mathbf{r}\to 0} \sum_{j\neq 0} (k^2\mathcal{I} + \nabla^2) \frac{e^{i\mathbf{k}(\mathbf{r}-\mathbf{R}_j)}}{|\mathbf{r}-\mathbf{R}_j|}. \tag{4.5}$$

The external electric field is considered to be $\mathbf{E}^{\text{ext}} = E_0^{\text{ext}} e^{ik'z}\mathbf{e}_x$, so that the related magnetic field is $\mathbf{H}^{\text{ext}} = \sqrt{\epsilon} E_0^{\text{ext}} e^{ik'z}\mathbf{e}_y$. The wavevector is defined as $\mathbf{k}^{\pm} = \pm k\mathbf{e}_z$ with $k' = k\sqrt{\epsilon}$. The total scattered field has magnetic and electric contributions

$$\mathbf{E}^{\text{scat}} = \sum_j \int \frac{d^2Q}{(2\pi)^2} \frac{2\pi i}{k'} e^{i\mathbf{k}(\mathbf{r}-\mathbf{R}_j)} (\mathbf{E}^p + \mathbf{E}^m). \tag{4.6}$$

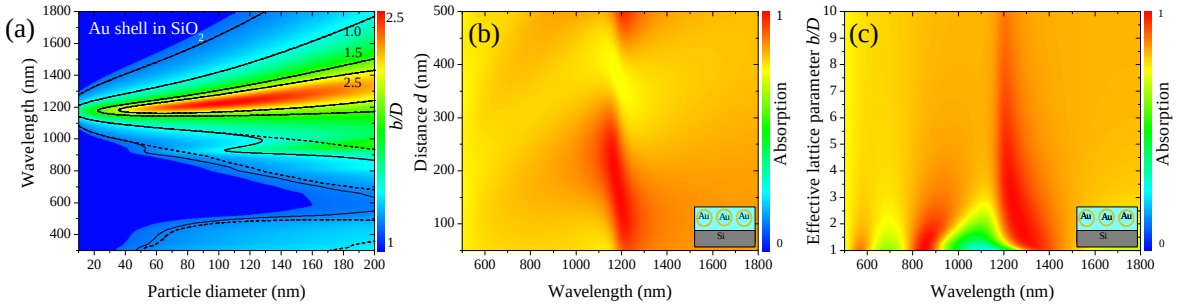

Fig. 4.12: **Particle arrays of gold nanoshells above a Si substrate in SiO_2.** The shell thickness is 5% of the radius. The parameters used are $D = 60\,\text{nm}$ and $b/D = 5$ and $d = 500\,\text{nm}$. The presence of the Au nanoshells boosts efficiently the absorption around its resonance $\lambda = 1.2\,\mu\text{m}$. (a) The spectral regime where total absorption is possible (i. e. $b > D$) is shown as a function of the particle diameter. (b) Absorption for this structure as a function of distance between the particle array and the substrate. (c) Absorption spectrum as a function of the effective lattice parameter.

We derive expressions for both electric ($\mathbf{E}^p$) and magnetic contributions ($\mathbf{E}^m$) in the scattering field in momentum space. Note that the external fields depend linearly on the dipolar moments in momentum space as

$$\mathbf{E}(\mathbf{k}) \sim \frac{1}{\epsilon} k'^2 \mathbf{p} \qquad \text{and} \qquad \mathbf{H}(\mathbf{k}) \sim \frac{1}{\epsilon} k'^2 \mathbf{m}, \tag{4.7}$$

respectively. From Maxwell's equation $ik\mathbf{H} = \nabla \times \mathbf{E}$, we find the magnetic contribution to the scattering with the ansatz $\mathbf{E}^m = \lambda \mathbf{k}'^{\pm} \times (k\mathbf{H})$. This results in $\lambda = -\frac{1}{\epsilon k^2}$ so that

$$\mathbf{E}^m = -\frac{1}{\epsilon k} \mathbf{k}'^{\pm} \times \mathbf{H} \sim -\frac{k'^2}{\epsilon^2 k} \mathbf{k}'^{\pm} \times \mathbf{m}. \tag{4.8}$$

Finally, the total scattered field is given by

$$\mathbf{E}^{\text{scat}} = \frac{k'^2}{\epsilon} \sum_j \int \frac{d^2Q}{(2\pi)^2} \frac{2\pi i}{k'} e^{i\mathbf{k}(\mathbf{r}-\mathbf{R}_j)} (\mathbf{p} - \frac{1}{\epsilon k} \mathbf{k}'^{\pm} \times \mathbf{m}). \tag{4.9}$$

Using $\sum_j e^{-i\mathbf{Q}\mathbf{R}_j} = \sum_{\mathbf{G}} \frac{(2\pi)^2}{A} \delta(\mathbf{Q} - \mathbf{G})$ and considering normal incidence ($\mathbf{G} = 0$), we arrive at

$$\mathbf{E}^{\text{scat}} = \frac{2\pi i k}{A} e^{ik|z|} (p \mp m) \mathbf{e}_x \tag{4.10}$$

in the far field. For the reflection and transmission coefficients, we find

$$r = \frac{2\pi i k}{A}(p - m), \qquad t = 1 + \frac{2\pi i k}{A}(p + m). \tag{4.11}$$

Together with the expressions from eqs. (4.2) and (4.3), the optical properties of a particle array are described by eq. (4.11) within the dipolar approximation. This is shown in Fig. 4.9, where we compare this approximation with higher-order numerical calculations demonstrating the range of parameters where convergence with rigorous solutions of Maxwell's equations is achieved.

The combined optical properties are found by summing up multiple reflection and transmission paths, leading to the expression

$$R = r + \frac{t^2 r_0 e^{2ik_z d}}{1 - r_0 r e^{2ik_z d}}, \tag{4.12}$$

where r_0 is the reflection of the substrate. The overall transmission of the substrate is assumed to be vanishing, $t_0 = 0$, and accordingly the absorbance is simply given by $1 - |R|^2$. Next, we compare configurations with and without absorbing material between the particle array and the conducting substrate, discussing total absorption features in those structures and the influence of the different system parameters.

Results and discussion

In Fig. 4.11, we demonstrate total absorption at specific wavelengths for a Au particle layer in SiO_2 above a Si substrate. Several absorption spectra with varying distance d between the particle array and the substrate are compared to the case of a bare Si substrate ($> 100\,\mu$m) in Fig. 4.11 (a). Figure 4.11 (b) shows the absorption spectra in this composition as a function of distance d. It can be seen that total absorption is achieved at different spectral positions for the different distances. This is due to the resonator type structure. A direct extension of our work would allow considering multiple particle layers of the same configuration, placed at different distances above the substrate, with overlapping spectral regions of enhanced absorption, leading to a broadband total absorber.

Notice that the Au particle array is resonant at low wavelengths (see Fig. 4.10) and absorptivity is increased beyond this resonant absorption, indicating an exclusive contribution to the absorption in the active material. The average absorption for a bare Si substrate in the 300-1200 nm range is 72.5% which we compare in Fig. 4.10 (a) to the Salisbury screen configuration. We find an enhancement of the mean absorption by 11.4% (d=300 nm), 11.6% (d=400 nm) and 8.7% (d=500 nm). The presented device composition is just an example that is not yet optimized. Ag and Si particle arrays are yet more promising due to their higher albedo, see Fig. 4.10 (b).

Our model allows for studying different particle shapes, that are defined via their polarizabilities. In Fig. 4.12 we apply our method to Au nanoshells. As for solid gold (Fig. 4.8 (b)), we show spectral regions where total absorption is possible in Fig. 4.12(a) by comparing the geometrical and optical cross section of these particles. Figures 4.12 (b) and (c) present the absorption spectra as a function of the distance to the substrate and the effective lattice parameter, respectively. The particle resonance is found at high wavelengths around 1200 nm

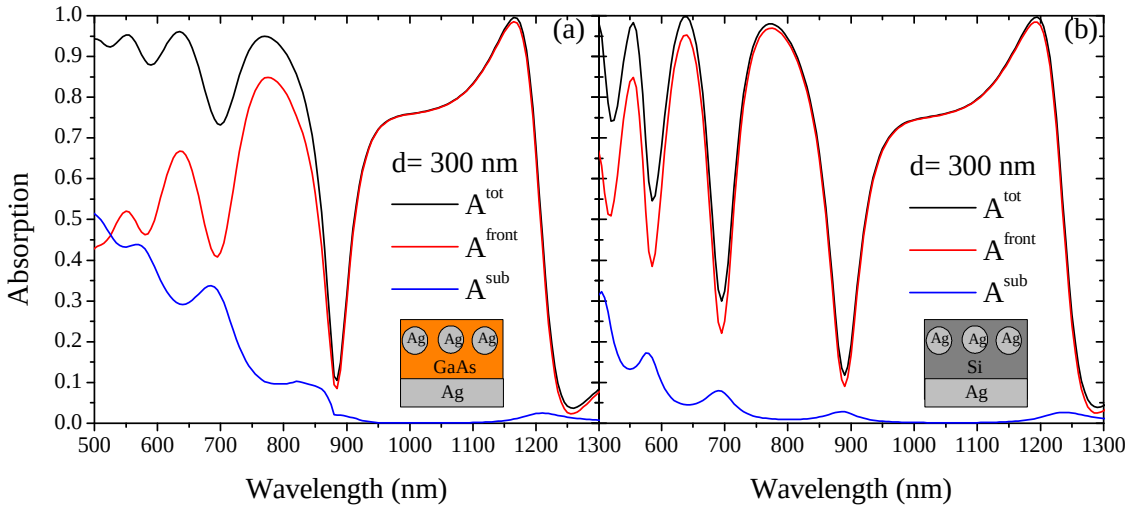

Fig. 4.13: **Study of a Ag particle array** in (a) GaAs and (b) Si above a Ag substrate at a distance of $d = 300$ nm. Due to Fabry-Pérot like resonances in the structure, total absorption is achieved at various wavelengths. The absorption of the Ag substrate, considered here as the contacts of the opto-electronic device, is small and most of the light is absorbed in the semiconductor.

in SiO_2, cp. also Fig. 4.10 (a). At this wavelength, most of the light is absorbed by the particles themselves. However, beyond that wavelength absorption is increased directly at the substrate. Tuning the particle size and shape to exhibit a resonance at certain wavelengths, enables us to design the particle array in such a way that individual particle absorption does not hinder the absorption in the active material. However, placing the particle array within the semiconductor material makes it interesting to adjust the resonance of the particle array close to the bandgap of the active material to ensure high field enhancement in this spectral region. In Fig. 4.13, we demonstrate this idea using Ag nanoparticles in GaAs and Si above a Ag substrate, in the role of a back contact. The absorption is again shown separately for the substrate and the volume in front of it, indicating that in this case, the substrate is indeed absorbing very little and the main part of the absorption is achieved in the semiconductor where the particle array is embedded. Remember that Ag particles are absorbing at very low wavelengths, cp. Fig. 4.10 (b). Although the absorption shows strong oscillations and it appears to be reduced at many wavelengths, the mean absorption in the spectral range of 300–1200 nm is efficiently increased, namely by 11.2% (GaAs) and 9.3% (Si).

We give a further example of a more realistic structure in Fig. 4.14. An array of Si particles at a short distance to the underlying Si substrate is considered, leading to an efficient increase in the mean absorption. The SiO_2 matrix embedding the particle array can be considered a passivation layer of 10 nm thickness below the particle array. It also plays the role of an index matching layer above the particle array, necessary in a real photovoltaic device to avoid destructive interference of incoming and scattered waves.[180] For the two chosen particle sizes, the mean absorption compared to bare Si is enhanced by 16.0% ($D = 60$ nm) and 18.9%

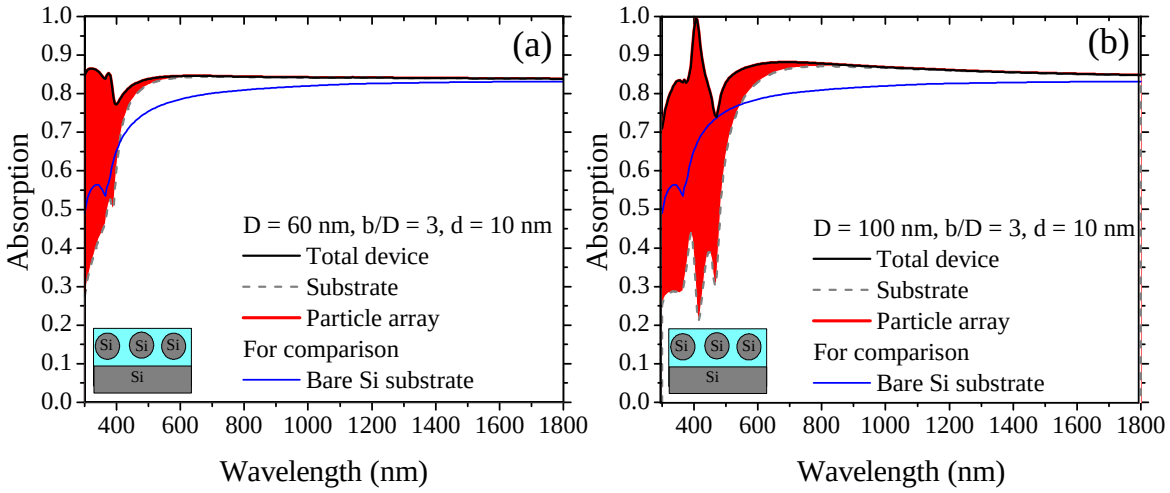

Fig. 4.14: **Absorption in a device consisting of a Si particle** array of diameter (a) $D = 60\,\text{nm}$ and (b) $D = 100\,\text{nm}$ with center-to-center separation $b = 3D$ on top of a Si substrate at a distance of $d = 10\,\text{nm}$. Both the absorption of the complete device and the share of absorption at the substrate level are shown. Red regions indicate absorption subjected to losses at the nanoparticles. The bare Si absorption is given by the blue curve.

($D = 100\,\text{nm}$).

There are various other compositions that can be investigated within our formalism. It is not the purpose of this study to provide an optimum design. However, all investigated compositions have revealed an increase in the mean absorption with respect to a bare Si substrate of at least 10%. This approach can be used for a rapid evaluation of a variety of designs, comparing different particle types and system parameters.

4.2 Random particle distributions

The high precision of the fabrication methods necessary for producing accurate regular particle arrays of a certain geometry may be difficult or simply expensive to implement in a complex production line. Production costs and efforts are very much reduced seeking a solution with self-assembled, random particle distributions. While we render the high control on size and shape, self-assembly techniques allow us to determine the average particle size and variance with reproducible statistical characteristics.[6,100,183]

Irregular plasmonic structures are of special interest for many applications within plasmonics since they provide a high density and broad spectrum of optical modes,[22,118,184] where weak coupling and increased scattering dominates the optical properties. This enhances the effective absorptivity of molecules or substrates in proximity to the particle layer enabling e. g. enhanced photoluminescence, nonlinear processes and efficient coupling of light to an

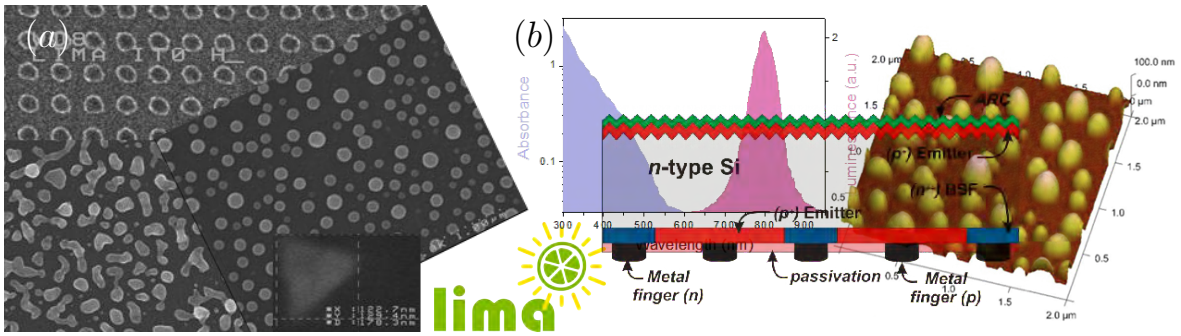

Fig. 4.15: **Illustration of the objectives of the LIMA European project.** (a) SEM images of various plasmonic particle layers studied here. (b) Photoluminescence of a SiO_x nanocrystal multilayer, atomic force microscopy (AFM) graph of a MNP layer and improved IBC design.

underlying structure.[14,25,98,185]

Another important application and our central interest in this section is plasmon-enhanced photovoltaics. The solar cell design rules developed to date have concentrated on regular structures and optimized absorption efficiency for a narrow spectral range.[22,118,124,128,186–188] Random particle layers, however, are known to provide a broad spectrum of overlapping plasmon modes.[6,107,122,189] Light coupling efficiency increases with the number of modes that can be coupled into the system.[190] However, theoretical studies and predictions of the optical properties of random patterns are difficult.[191,192] Most research in this direction considers alloys or structured metal films[193,194] describing their optical properties with effective medium theory.

In this section, we use a simple route towards the modeling of optical spectra of random samples where only the particle size and distance distributions are needed as an input for optical calculations including interactions between these particles. We use this formalism to simulate the optical properties of specific random distributions of nanoparticles. Note, that the theory of random distributions for photovoltaic applications can equally be applied for metal and dielectric structures, as well as particles of any shape. However, we concentrate on random layers made of Al and Ag spherical nanoparticles.

4.2.1 FP7 LIMA project in perspective

To "improve photovoltaic eficiency by applying novel effects at the limits of light to matter interaction" is the set aim of the European LIMA project.[8,101] It exploits cutting edge photonic technologies to enhance silicon solar cell efficiencies with new concepts in nano-structured materials. On the front of an integrated back contact (IBC) solar cell,[112] nano-structured surface layers (plasmonic particles and Si nanocrystals) are designed to increase light absorption via a variety of effects, such as downshifting, scattering and near-field enhancement and to improve industry compatible light management in solar cells on the nanoscale.

The baseline cell has been improved tremendously to show an optimized efficiency of 19,6%

at the end of the project. Si nanocrystal layers were used for downconversion via photoluminescence reaching a projected efficiency enhancement of 10% relative to the baseline cell.[98] Experiments and theoretical work on these topics have been done by a number of partners in Europe and Australia. We concentrate here on our contributions to plasmon-assisted enhancement of standard Si solar cells to increase e. g. the probability of multiple exciton generation (MEG process) by providing high local fields. On the other hand, in combination with the Si nanocrystal layer, an enhanced downconversion efficiency was achieved.

The main contribution of the random plasmonic particles is the increase of the optical path length of the incident light and thus enhanced absorption inside the device, due to its strong scattering making use of individual particles efficient subwavelength scattering. Furthermore, light incident from a large angular range is captured by these layers. We develop design rules for random plasmonic particle layer (PPL) specifications which yield an overall increase in absorption efficiency and a high density of optical modes. The PPL is combined with standard anti-reflection coating (ARC) technology, resulting in an overall improved performance and acting similar to cell texturing, as a result of light scattering at the PPL.[5,6,35]

Experiments were performed at the Nanotechnology Center (NTC) of the Universidad Politécnica de Valéncia (UPVLC), Spain.

4.2.2 Random electron beam lithography

Random Al and Ag nanoparticle distributions are studied on varying substrates, where we exploit the nanosphere self-aggregation method (NSA) for fabrication. Relying on the measured particle size distributions of these samples, we develop a theoretical model that can be applied to arbitrary random nanostructure layers as is demonstrated for several distinct NSA samples, see Fig. 4.16. As a proof of concept, the optical properties of the exact same particles distributions, made from the quasi random modeling input with electron beam lithography (EBL), are investigated from both theory and experiment. Our numerical procedure is based on rigorous solutions of Maxwell's equations and yields optical spectra of fully interacting randomly positioned nanoparticles. These results constitute a new methodology for improving the optical performance of layers of nanoparticles with direct application to enhanced photovoltaics.

Nanospheres self-aggregation

The industry-compatible nanosphere self-aggregation method (NSA) yields random distributions of particle geometries that are determined by statistical parameters only, such as particle size mean and variance.[100,183] It is a low cost fabrication method assuring technical adequacy without any necessary cleaning steps. Here, see Fig. 4.17, a thin silver film is exposed to evalated temperature and self-aggregates on its substrate into a sheet of randomly placed metallic nanoparticles. During fabrication, the anneal temperature and time as well as the initial Ag precursor thickness define the final particle density and homogeneity allowing

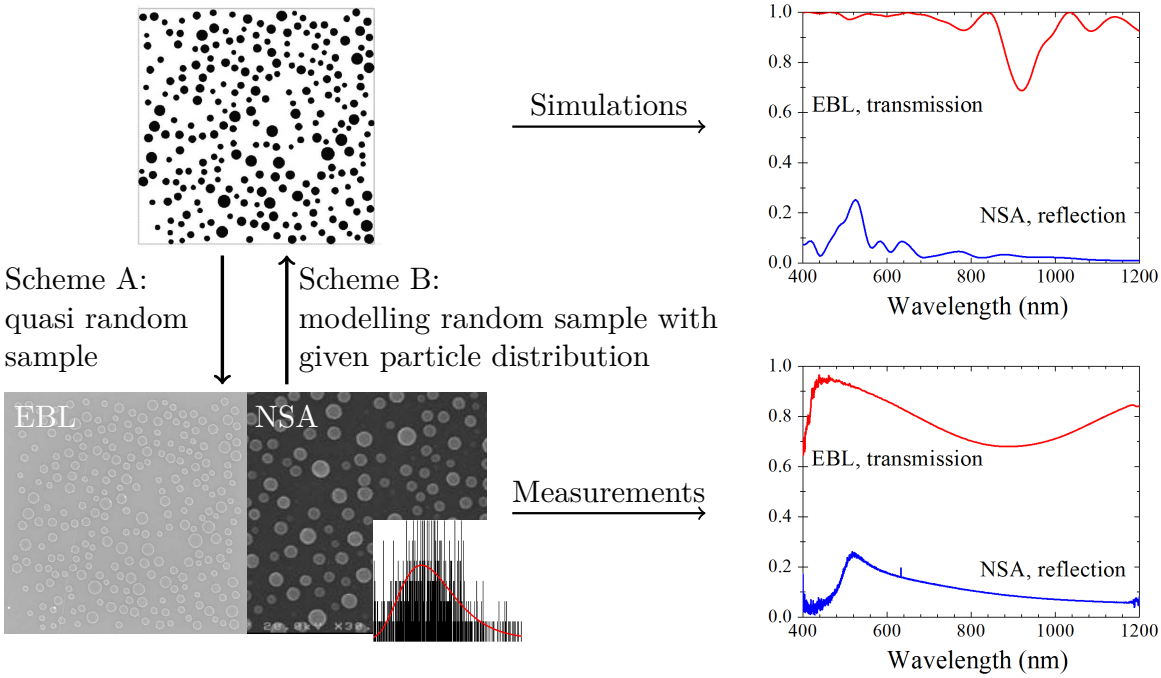

Fig. 4.16: **Illustration of the numerical procedure behind REBL.** Quasi-random numerical samples are set up and subsequently fabricated with EBL in order to compare the optical characterization and simulations (scheme A). On the other hand, statistical data from random nanosphere self-aggregation method (NSA) samples are used as input to the modeling (scheme B).

control of metal nanoparticle (MNP) geometrical parameters to some extent. Anneal temperatures can be below other processing temperatures, usually used during solar cell fabrication, enabling integration of MNP layers in photovoltaic device manufacturing. A further advantage is its high integrability, since the deposition of a plasmonic layer on various structures and substrates can be achieved without diffculties.

This method is well suited to fabricate large area films, and as such is suitable for mass fabrication of semiconductor solar cells. Other types of solar cells, such as synthetic dyes or organic polymer cells, are equally benefiting from the addition of plasmonic particles.[195] However, the MNPs need to be placed directly inside the dye or polymer, which requires mehods such as electrodeposition or chemical deposition.

To achieve a high degree of homogeneity, temperatures of hundreds of degrees Celsius are favored during the annealing process. The obtained particles are then hemi-spherical with negligible differences between minor and mayor axis. However, in our case we cannot use high temperatures in order to prevent damage of the solar cell, so that we restrict ourselves to the 100°-400°C temperature range, hence requiring 1-3 hours of annealing. Finally, the choice of the Ag precursor thickness determines the mean particle size in the sample. This fabrication method enables a wide range of parameters (particle diameters 70-400 nm and interparticle spacings 20-200 nm).

NSA samples fabricated at both high and low temperatures have been investigated where

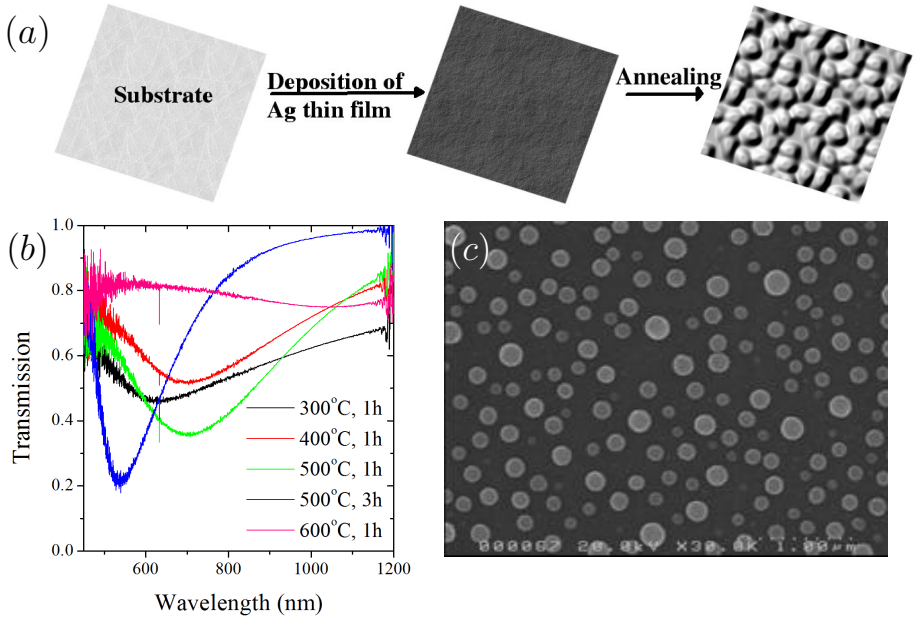

Fig. 4.17: **(a) Schematic process of the nanosphere self-aggregation (NSA) method.** (b) Optical characterization results for different annealing temperatures and times. This demonstrate how sensitive the optical properties are to fabrication parameters that result in different statistical characteristics of the NSA samples. (c) SEM image of a sample fabricated at 500°C and annealed for 3 hours for an initial Ag film thickness of 20 nm.

a clear difference in e. g. the mean particle size can be seen. This directly translates into different optical properties. The resulting NSA samples are structurally characterized by scanning electron microscopy (SEM, Fig. 4.17 (c)) and by spectrally resolved transmission and reflection measurements (Fourier transform infrared spectroscopy (FTIR)). As can be seen from measurements under different anneal conditions in Fig. 4.17 (b), the final particle layer characteristics crucially determine the optical spectra.

While the particle geometry obtained by NSA (Fig. 4.17 (c)) is relatively homogeneous, the plasmon resonance strongly dependends on the average particle size, and the broadening is related to the width of the particle size distribution.

The optical characterization demonstrates NSA plasmonic layer transmission (Fig. 4.17 (b)) above 90% in the long wavelengths range, but also shows a reduced transmission for short wavelengths. This reduced transmission and associated loss due to reflection, interference, and absorption, has been identified as a concern in prior art, as the losses at short wavelength range[183] compete with the enhanced absorption efficiency at long wavelengths. Solutions reducing the short wavelength loss include adjusting particle size and distribution, and incorporating an additional index matching layer on top of the PPL.[114]

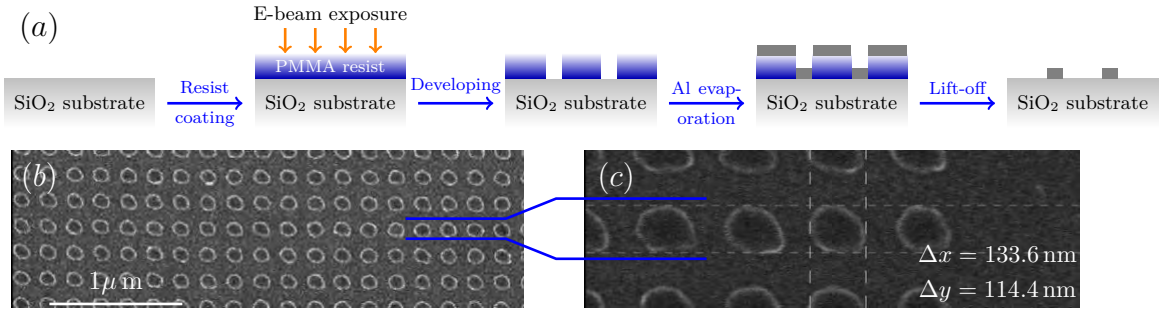

Fig. 4.18: **(a) Schematic process of electron beam lithography (EBL).** (b) SEM image of a fabricated sample showing a high control over particle position and shape. (c) Zooming into the finalized structure reveals a good homogeneity of the obtained particles.

Electron beam lithography (EBL)

High quality nanostructures fabricated with electron beam lithography (EBL) show very regular pattern with high size and shape control, see Fig. 4.18. This procedure is perfectly reproducible exploiting resist development using a standard Al deposition method.

The physical samples obtained with the NSA are difficult to model. To resolve this issue, we first present a combined experimental and theoretical study on the same exact particle distributions, chosen with a high degree of randomness. First, an quasi-random distribution is constructed numerically based on mimicking a truly random NSA distribution. An exact copy of this is fabricated by exploiting high-resolution electron beam lithography (EBL), see Fig. 4.18, following specific particle sizes and positions that are analytically defined. Then, the theoretical response is simulated for this quasi-random distribution and compared with the corresponding measurements for this distribution.

This combination of experimental analysis and theory is a novel approach. It first allows validation of the modeling methodology by comparison with exact data on characterization of (random) EBL samples. This in turn allows the modeling of experimental self-aggregated particle distributions, yielding a methodology for optimizing experimental PPL properties.

Theoretical approach towards random particle distributions

We numerically study the optical performance of random PPLs by applying exact electrodynamic modeling[132] briefly summarised in this section.

The resulting design methodology enables us to identify desirable particle diameters for the highest possible scattering efficiencies. The recommendations from the modeling are well within the wide range of parameters achievable with the NSA technique, and distributions with particle sizes of less than 100 nm in diameter are best suited. In this range, MNPs are efficient scatterers and dispersive losses are negligible.[118,183] A detailed image analysis provides us with information about the particle size and distance distribution. With the knowledge of these statistical parameters, we intend to predict optical spectra of related

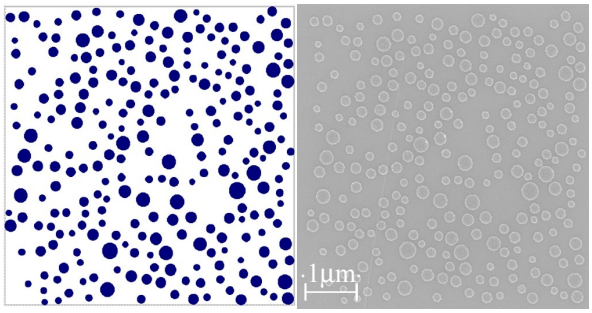

Fig. 4.19: **Agreement achieved between numerical and fabricated quasi-random REBL sample.** Comparison of a numerical (left) and the corresponding physical sample (right, SEM picture) fabricated with electron beam lithography (EBL), covering an area of $5 \times 5\mu\text{m}^2$ with homogeneous Al particles. The achieved agreement is excellent, thus enabling direct comparison of optical characterization and its simulation.

random patterns as obtained by the NSA method using the numerical procedure described previously.

Exact theoretical modeling of random PPLs is challenging. We introduce a quasi-random electron beam lithography (REBL) technique that enables direct comparison between experiment and modeling. EBL is an accurate nanofabrication method well suited for systematic study of precisely defined geometries, enabling exact comparison with modeling. Its resolution and the particle size in the quasi-random samples guarantee that aberrations from the ideal circular shape are negligible.

Numerical quasi random PPLs are obtained with a random number generator using a suitable distribution for particle sizes and, independently, a uniform distribution of particle positions. We provide several $5 \times 5\mu\text{m}^2$ samples numerically, maintaining minimum distances as determined by EBL resolution. Physical Al samples with exactly the same geometries were fabricated with EBL, enabling direct comparison of optical spectra calculated and measured on equal quasi-random samples. A comparison of the exact numerical sample specification with SEMs of the EBL fabricated experimental analogue show exact agreement (see Fig. 4.19). Note, however, that the shape of the particles fabricated through EBL is cylindrical rather thean spherical, in contrast to the assumption in the simulations. For optical measurements, a much larger area has to be provided, so we use repeated patterning of the random sample to obtain areas of $200 \times 200\mu\text{m}^2$. Parallel experimental and computational optical characterization (Figs. 4.20 and 4.21 and following discussions) provides optimum insight into the physical behaviour of the truly random Ag PPL fabricated by NSA and the quality of the theoretical modeling. The modeling method is based on exact electrodynamic simulations as mentioned above, using a multiple scattering technique[132] for a large number of interacting particles. They are represented in terms of self-determined multipolar expansions up to a maximum value of the multipolar order ~ 25 in order to obtain numerical convergence. This method includes retardation arising from both particle size and cluster size.

Here, each spherical particle α randomly placed at $\mathbf{r}_\alpha$ contributes to the electric field $\mathbf{E}$ via its corresponding far-field-amplitude $\mathbf{f}_\alpha$. This contains the full optical response of the particle α, including the refractive index of the environment and the self-consistent interaction with all other particles. The particle interaction is calculated on the basis of the scattering matrix of the single particles, and thus, it includes all spectral and geometrical information. The far field can thus be written as

$$\mathbf{E}(\mathbf{r}) = \sum_\alpha \mathbf{f}_\alpha \frac{e^{ik|\mathbf{r}-\mathbf{r}_\alpha|}}{|\mathbf{r}-\mathbf{r}_\alpha|}. \tag{4.13}$$

The wavevector is defined as $\mathbf{k} = (\mathbf{Q}, k_z)$, with k_z perpendicular to the 2D array and $k_z = \sqrt{k^2 - Q^2}$. The particle positions are $\mathbf{r}_\alpha = (\mathbf{R}_\alpha, 0)$, assuming that the relative z-coordinate does play a minor role due to the small particle sizes. Thus, we can express eq. (4.13) as

$$\mathbf{E}(\mathbf{r}) = \sum_\alpha \mathbf{f}_\alpha \int \frac{d\mathbf{Q}}{(2\pi)^2} \frac{2\pi i}{k_z} e^{-i\mathbf{Q}\mathbf{R}_\alpha} e^{i\mathbf{k}\mathbf{r}}. \tag{4.14}$$

Both the numerical and the experimental samples consist of a $5\times5\mu\text{m}^2$ region that is repeated periodically over a square array of 40×40 periods of spacing $d = 5\mu$m. The sum in eq. (4.14) can then be separated into a sum over each unit cell (index α_0 of the contributing particles) and a sum over all unit cells (index j), so that the positions become $\mathbf{R}_\alpha = \mathbf{R}_{\alpha_0} + \mathbf{R}_j$. This can be performed for an infinite array by separating it as

$$\sum_\alpha \mathbf{f}_\alpha e^{-i\mathbf{Q}\mathbf{R}_\alpha} = \sum_{\alpha_0} \mathbf{f}_{\alpha_0} e^{-i\mathbf{Q}\mathbf{R}_{\alpha_0}} \sum_{\mathbf{R}_j} e^{-i\mathbf{Q}\mathbf{R}_j}. \tag{4.15}$$

Using $\sum_{\mathbf{R}_j} e^{-i\mathbf{Q}\mathbf{R}_j} = \frac{(2\pi)^2}{A} \sum_{\mathbf{G}} \delta(\mathbf{Q}+\mathbf{G})$ and performing the 2D discrete Fourier transform in the particle plane for the regular superlattice, we find

$$\mathbf{E}(\mathbf{r}) = \sum_{\alpha_0} \mathbf{f}_{\alpha_0} \sum_{\mathbf{G}} \frac{2\pi i}{A k_z^{\mathbf{G}}} e^{i\mathbf{G}\mathbf{R}_\alpha} e^{i\mathbf{k}^{\mathbf{G}}\mathbf{r}}, \tag{4.16}$$

where we now sum over reciprocal lattice vectors $\mathbf{G}$ of the superlattice and the wavevector has become $\mathbf{k}^{\mathbf{G}} = (-\mathbf{G}, k_z^{\mathbf{G}})$ and $k_z^{\mathbf{G}} = \sqrt{k^2 - G^2}$. Here, A denotes the area occupied by the particles in the unit cell (i. e. $A = 25\mu\text{m}^2$). Then, the total far-field amplitude $\mathbf{f}$ for $(z \to \infty)$ of the PPL is used to calculate the transmission and reflection coefficients. A high angular resolution in the measurements assures normal scattering conditions $\mathbf{G} = 0$. We can write (for normal incidence)

$$\mathbf{E}(\mathbf{r}) = \mathbf{f} \sum_{\mathbf{G}} \frac{2\pi i}{A k_z} e^{ik_z|z|}, \qquad \mathbf{f} = \sum_{\alpha_0} \mathbf{f}_{\alpha_0}, \tag{4.17}$$

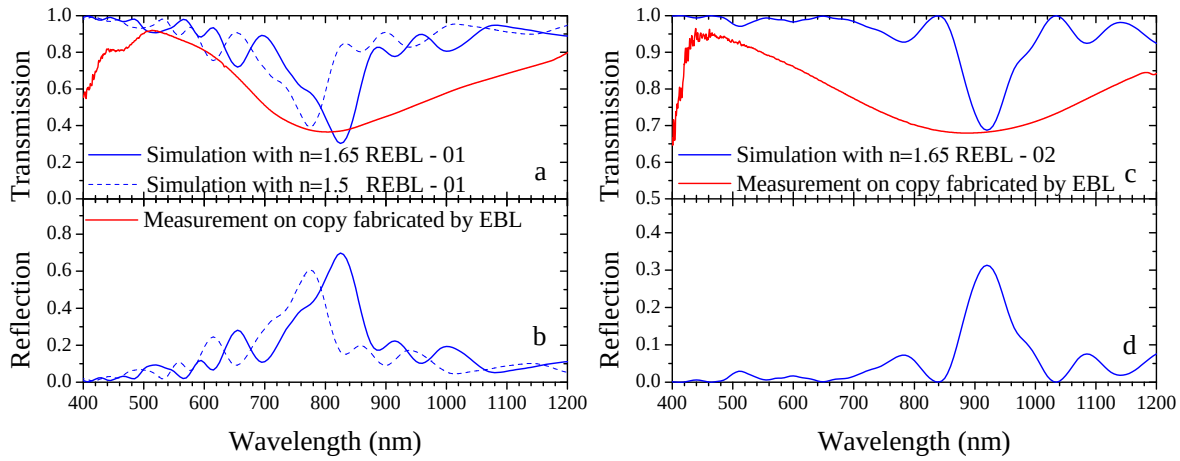

Fig. 4.20: **Comparison between measured and calculated transmission spectra for two REBL samples of Al particles.** (a), (c) Measured (red) and calculated (blue, upper panel) transmission spectra for two $5 \times 5\mu\text{m}^2$ REBL samples of Al particles. By comparing with measurements on exact copies of the numerical samples fabricated by standard EBL we show that the main plasmon peak position of the random ensemble and the transmission value thereof are well described by our computational approach. Additionally, (a) gives results for two glass environments with different refractive index n to demonstrate the effect of the permittivity of the surrounding medium. (b), (d) From the calculated reflection (blue, lower panel), eq. (4.18), we obtain the transmission by neglecting absorption contributions $T = 1 - |r|^2$.

and find the reflection coefficient at a given wavelength $\lambda = \frac{2\pi}{k_z}$ to reduce to

$$r \approx \frac{i(\mathbf{f} \cdot \hat{\mathbf{x}})\lambda}{A} \frac{n}{E^{\text{inc}}}. \tag{4.18}$$

Here, n indicates possible contributions from spots of higher order $\mathbf{G} \neq 0$. We assume $n = 1$ for our calculations. Note that the procedure is identical for metallic or dielectric particles.

In contrast to regular patterns of MNPs, which display a narrow plasmon resonance, a PPL exhibits a broad plasmon resonance which can be understood as a superposition of localized resonances from individual particles as well as resonances emerging from interparticle coupling. The host permittivity, in which the PPL is embedded, is included as a wavelength independent constant. In Fig. 4.20(a), we investigate the influence of the permittivity of the surrounding medium. Optical measurements of physical REBL samples are directly compared with optical simulations in Fig. 4.20 giving valuable feedback on the procedure.

Finally, after analyzing Al particle sizes and distributions in NSA samples, numerical samples using these geometrical parameters are modeled and characterized. An improved prediction of expected transmission (calculated as $T = 1 - |r|^2$ and thus not showing absorption explicitly) and reflection spectra is then obtained (see Fig. 4.21). Wavelength-dependent calculations of finite substrates, as used in these experiments, were performed separately and combined with the PPL response simulated in a homogeneous medium. A summary of the

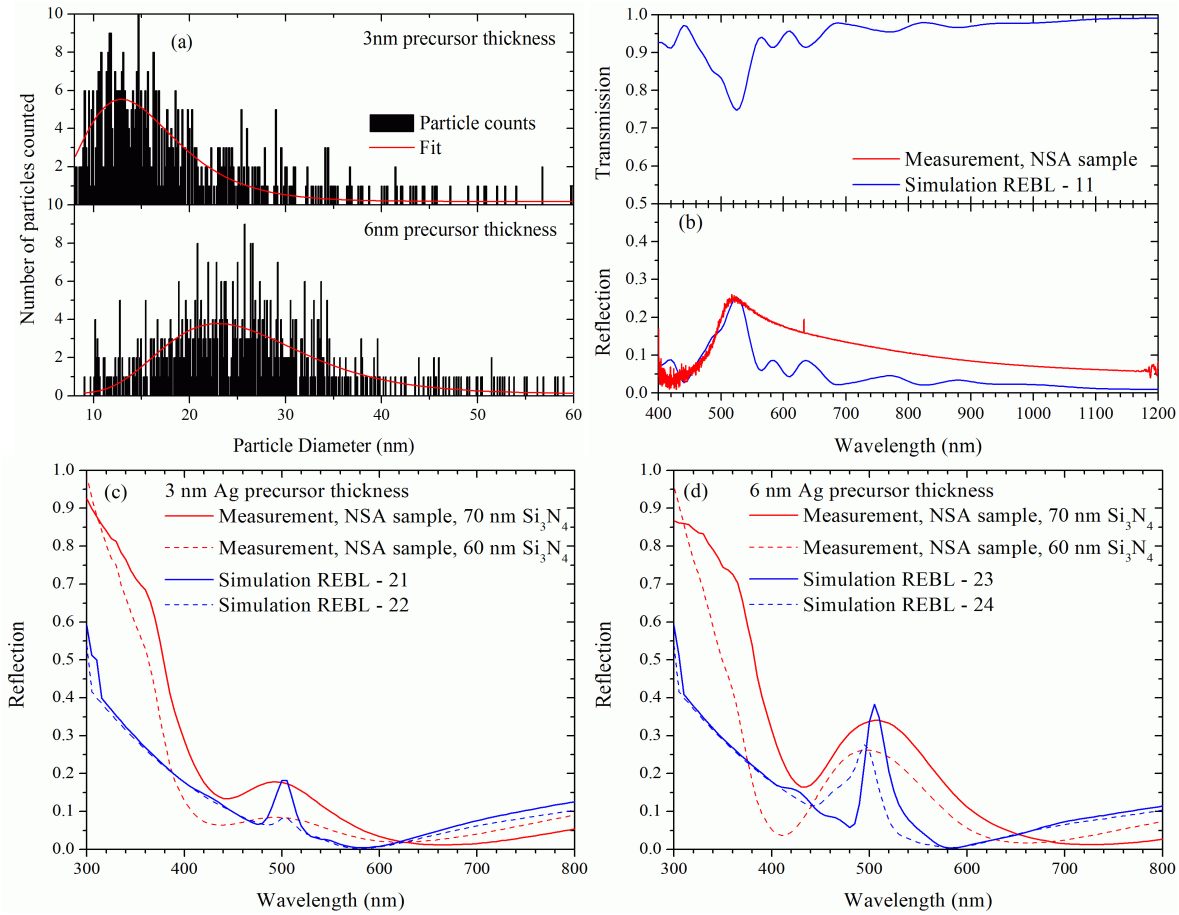

Fig. 4.21: **Application of the REBL approach to real NSA samples for different Ag precursor thicknesses, annealing temperature and annealing time, as well as different substrates.** Examples of the REBL approach (blue curves show simulated spectra) compared to real NSA samples (measurements depicted in red) for different Ag precursor thicknesses, annealing temperature and annealing time, as well as different substrates. (a) Statistical parameters are retrieved by an automated image analysis and fitting of the particle diameter counts to a suitable distribution function (here Gaussian). (b) Reflection spectrum for a high temperature (500°C, 3h) sample encompassing glass with a Ag precursor thickness of 20 nm. Excellent agreement of plasmon peak position and maximum reflection is found between theory and experiment. (c)-(d) Results on low temperature samples fabricated on Si_3N_4 layers of different thickness on Si. The Ag precursor thickness was varied from 3 nm to 6 nm. In the numerical samples of particle distributions, this is reflected through distinct statistical parameters, as shown in (a).

statistical parameters used can be found in Table 4.1, demonstrating that this procedure can cope with several hundreds of particles including their full interaction and retardation. Note, that a multiple scattering approach is more feasible than finite difference time domain (FDTD) calculations on random samples of that size.

	Mean Diameter	Variance	Particles	Substrate
REBL-01	150 nm	25 nm	102	SiO_2
REBL-02	150 nm	25 nm	128	SiO_2
REBL-11	100 nm	20 nm	250	SiO_2
REBL-21	12 nm	2 nm	555	Si_3N_4
REBL-22	12 nm	4 nm	527	Si_3N_4
REBL-23	24 nm	10 nm	441	Si_3N_4
REBL-24	30 nm	10 nm	710	Si_3N_4

Table 4.1: Parameters of particle distributions used as input for optical calculations on quasi random REBL samples. The first two samples have been fabricated with EBL using Al particles (cf. Fig. 4.19 and Fig. 4.20). A minimum distance compatible with the experimentally achievable spatial resolution was set to $d_{\min} = 50\,\text{nm}$. Further REBL samples assume $d_{\min} = 1\,\text{nm}$ to allow for all possible spacings. NSA samples are fabricated using Ag particles. The third sample was made under high temperature NSA conditions (500° C), whereas the lower samples on Si_3N_4 were produced at low temperatures (200° C).

Results and discussion

Optical spectra are presented for REBL samples in Fig. 4.20 and directly compared to the corresponding FTIR measurements on exact copies made with EBL. The $5 \times 5\mu\text{m}^2$ samples on glass show very good agreement both in the plasmon peak position and in the expected minimum transmission. The broadening is however underestimated. The obtained oscillatory behavior indicates the different plasmon peak positions arising from (a) particles of different sizes and (b) the interaction between particles (coupled modes) that naturally lead to a smooth broadening of the main peak in the measured, more extended samples. We note here again that the physical samples include larger ensembles of repeated quasi-random patterns, whereas the simulations are restricted to a single pattern, see Fig. 4.19. The effect of the host permittivity is shown in Fig. 4.20 (a). As expected, for higher permittivities the main peak is shifted to higher wavelengths. Note that the drop in the measured transmission for wavelengths below 450 nm (red curves) is due to the lower FTIR detector sensitivity in that spectral range.

Transmission for even shorter wavelengths is expected to decrease due to two aspects: Single particle resonances (LSPRs) are found below 400 nm for Ag and Al particles and result in typical antenna reflection. In random samples, both single particle resonances and lattice (geometric) resonances are always found.[103,183] On the other hand, very small particles, as used for the samples discussed in Fig. 4.21 suffer from ohmic losses at low wavelengths. Furthermore, in the case of Si_3Ni_4, the reflection of the substrate increases strongly, see Fig. 4.21 (c) and (d). Therefore, the range below 400 nm is not considered here.

Aiming at a description of physical NSA samples, we introduce in Fig. 4.21 (a) typical statistical data from NSA samples used as an input for the calculations. Image analysis of SEM pictures of the $2 \times 2\ \text{cm}^2$ samples was performed on $300 \times 300\ \text{nm}^2$ representative areas

with total particle numbers of 500 - 1500. This experimental statistical particle data is then fed into the model, which yields a simulation of the physical NSA samples.

In this manner, both high and low temperature NSA samples have been fabricated and simulated. The main difference is in particle distribution characteristics, as can be seen from the data in table 4.1. The numerical method introduced relies only on the statistical paramters and is proven to describe both cases equally well, see Fig. 4.21 (b).

Samples were fabricated on Si_3N_4 layers of different thicknesses on top of Si. The substrate layers optical response has been calculated seperately, and REBL calculations are obtained assuming a wavelength-independent host material. Both spectra are then combined, and although interaction between wavelength-dependent substrate and PPL is thus not included, the agreement of plasmon peak positions and expected reflection are very good. Including this interaction might lead to improved agreement, especially at low wavelengths.

4.3 Summary

In this chapter, we investigate different aspects of collective effects in regular and random particle arrays.

The measured intensity distributions are in excellent agreement with our electromagnetic simulations on the complex optical near-fields of colloidal monolayers imprinted on thin GST films. This simple yet effective concept is well suited for nanostructuring and mapping arbitrary intensity distributions with high spatial resolution, which can be implemented directly for large scale fabrication on other substrates. The imprinted near-fields inherit the full translational invariance from the colloidal monolayer. At the same time, by studying the influence of various setup parameters, we conclude that the detailed near-field distribution is not only determined by the particle arrangement but also strongly depends on light polarization and angle of incidence. In particular, the number of near-field maxima is not limited by the number of particles and can be increased by the proper choice of illumination conditions. The orientation of the lattice with respect to the light incidence direction is found to have a significant impact on the near-field distribution, thus providing an additional degree of freedom to tailor patterned imprinted structures.

The Salisbury screen configuration can lead to complete optical absorption in photovoltaic devices exploiting the unique properties of regular nanoparticle arrays. We demonstrate this in particular for setups incorporating Au nanospheres and nanoshells, Ag particles and contacts and Si particles investigating GaAs and Si as active materials and SiO_2 as embedding matrix. The analytical method developed allows for rapid evaluation of different compositional and structural parameters. Our work provides thus a fast way of estimating the performance of devices composed of particle arrays, which is advantageous for optimizing compositional and geometrical parameters for the fabrication of actual devices. Further work is needed to apply this model to more realistic systems such as those considered in the many designs that have

been introduced in recent literature.[18,22,103,108,114,115,117–129]

To achieve a photovoltaic device with broadband total absorption, several routes are possible, which we summarize here. Firstly, adding multiple particle arrays of the same configuration, placed at different distances above the substrate, covers a broad spectral range, assuring at the same time, that each particle array absorbs itself at low wavelengths. This is a direct extension of our work. Secondly, combining within a single particle layer different geometrical parameters, shapes, or sizes, allows for adjusting the resonances on a structural basis. This has been demonstrated for metamaterials.[179] Thirdly, addressing the high absorption at the nanoparticles by directly placing them in absorbing material, enables to boost the absorptivity directly in the device without changing the outer geometry. Furthermore, we develop under the same scheme, expressions that account for the angular dependence of the Salisbury screen.

Finally, a simple procedure is given for describing the optical properties of random metal nanoparticle distributions on substrates as possible, cost efficient building blocks for photovoltaic devices. A combination of experiment and theory is presented using standard EBL fabrication to provide exact copies of numerically provided quasi-random samples. Optical characterization and electromagnetic simulation on the exact same random samples are made possible by this dual approach.

Excellent agreement on the wavelength position and the value of transmission features is achieved, although experimental broadening of the spectral features is underestimated by our calculations. This indicates that the particle density is sufficient to predict peak positions and transmission values, but the number of particles taken into account in this study is too low, as the broadened features presumably arise from coupling a vast number of particles.

Our experimental work is based on the findings of Yang et al.[183] and reproduces the low reflectances found for Ag particle samples. To our knowledge, previous theoretical work on random particle layers is mostly based on effective medium theories (alloys, structured metal films[193,194]) and can therefore not capture the full interaction picture given in the present study.

Our procedure can be used to predict optical spectra of specific realizations of random samples. It can be exploited to optimize the optical properties and therefore provide statistical parameters of an optimum, random nanoparticle layer. Both metal and dielectric nanostructures can be considered. Furthermore, since the procedure is based on the scattering matrix of simple objects, it can easily be used for studying other shapes, such as hemispheres and disks on various substrates.

The method was applied to predict optical spectra of physical random samples fabricated using the nanosphere self-aggregation (NSA) and by relying only on measured geometrical parameters as an input for the calculations.

Our study opens a new methodology for designing optimized geometries of nanophotonic structures, and in particular, samples of nanoparticles as those discussed here, to improve the efficiency of optical absorption in photovoltaics.

5 Conclusions

Understanding is, after all, what science is all about - and science is a great deal more than mindless computation.

(Sir Roger Penrose)

Both fundamental and application-inspired aspects related to collective excitations of the free electron gas in metals are studied.

In a first central topic, we provide strategies to account for nonlocal electron interactions with semi-classical approaches that allow for a rapid evaluation of a variety of plasmonic nanostructures as compared to *ab initio* methods. We are able to identify simple nonlocal expressions vanishing in the local limit ($k_{\parallel} \to 0$), that provide a straightforward extension of known procedures. An accurate description of nonlocal properties of metal nanostructures is important to predict the optical response of molecules in close proximity to metal surfaces, the resulting field enhancements and the accompanying nonlinear effects.

The impact of nonlocal effects is studied within the following different models:

- The non-retarded specular reflection model (SRM) relying on the k-dependent Mermin dielectric function;

– The retarded hydrodynamic model, where we derive

  > extended Mie scattering coefficients for metal spheres and nanoshells, comparing the retarded limit of the obtained expressions with the SRM, allowing us to study aggregates of such particles by exploiting multiple scattering theory;

  > the nonlocal analogue to Fresnel's coefficients for planar interfaces, which can be employed directly to study complex planar multilayer structures;

– The electrostatic regime, for which we provide an extension of the hydrodynamic model including the electron spill-out;

  > using a transfer matrix approach to describe smooth surfaces in terms of realistic electron density profiles;

  > demonstrating the remarkable impact of the spill-out in the local limit, independently of nonlocal interactions in the electron gas, but including the smooth electron density profiles;

  > introducing an extended framework to account for the local density of optical states (LDOS) placing a probe emitter close to a smooth metal surface.

These different approaches have been applied to and compared in a variety of plasmonic structures, namely

- Spheres, nanoshells, dimers and Yagi-Uda nano-antennas;
- Planar structures, such as metal surfaces, slot waveguides and thin films;
- With direct consequences to fundamental optical concepts such as imaging, sensing and other field enhancement related applications, as well as light guidance on the nanoscale.

We calculate radiation scattering cross sections, reflection and transmission coefficients, the LDOS, as well as plasmon dispersion curves for several of these geometries and we identify structural parameters in these devices towards the common local approximation beyond which ideal concepts of electrodynamics are compromised. All of the above is carried out in the scope of nonlocal material properties in the involved metal components.

The explicit differentiation between nonlocal bulk effects, using sharp boundaries, and nonlocal edge effects including realistic smooth electron density distributions at metal surfaces, allows us to discuss the different contributions to commonly observed effects at the nanoscale, such as increased plasmon quenching (resulting in reduced field enhancement), frequency shifts and additional damping channels provided by the longitudinal pressure waves of the dynamic electron density. Furthermore, we can reproduce nonlocal and other effects observed in experiment and so far only predicted by first-principle methods.

In conclusion, the main difference between the local sharp and the numerical evaluation of nonlocal smooth electron densities for different types of basic plasmonic building blocks lies within the smooth density itself and not in the influence of nonlocal phenomena in this description. Local smooth and nonlocal smooth descriptions show similarities in all investigated geometries and differ significantly from the optical response found in the common local approximation and also from a nonlocal model assuming sharp interfaces. Effects of bulk nonlocality are thus counterbalanced by the smooth interface. A smooth interface, however, which we study by comparing the local sharp and smooth theories, leads already to plasmon quenching and broadening, but not to a shift in mode positions.

In summary, we demonstrate that the hydrodynamic model can suitably describe the nonlocal phenomena that arise from the quantum nature of the free electrons. It provides physical insight and rapid evaluation of systems involving nanostructures and does not involve free parameters. This study is particularly relevant for broad, active areas involving applications of local field enhancement to biosensing and nonlinear optics. Our results pave the way toward a comprehensive, computationally affordable description of nonlocality for arbitrary nanometallic morphologies.

The second central topic is strongly application oriented and focuses on collective effects in the local fields for regular and random particle arrays with an emphasis on optical data storage and enhanced absorption efficiencies in 3rd generation solar cells.

A promising concept for large scale nanoprocessing is the nanoimprint of optical near-fields using colloidal monolayers. In this context, we

- experimentally and theoretically study a close-packed hexagonal monolayer of dielectric micrometer-sized polystyrene (PS) spheres;
- achieve the nanoimprint of optical near-field patterns into a thin $Ge_2Sb_2Te_5$ (GST) film via ablation through short laser pulses varying the illumination conditions in terms of
  - > polarization of the incoming light;
  - > rotation of the hexagonal lattice with respect to the plane of incidence;
  - > angle of incidence;
  - > particle size and incoming wavelength through bandstructure calculations;
- find excellent agreement with experiment using calculations based on multiple scattering theory for regular, layered homogeneous materials;
- discussed the robustness of imprinted patterns in the presence of small defects.

The imprinted near-fields inherit the full translational invariance from the colloidal monolayer. In addition, the number of near-field maxima is not limited by the number of particles and can be increased by the proper choice of illumination conditions. This simple yet effective concept is well suited for nanostructuring and mapping arbitrary intensity distributions with high spatial resolution, which can be implemented directly for large scale fabrication on other substrates.

Plasmon-assisted absorption enhancement in solar cells is investigated in two ways. Firstly, we apply the Salisbury screen setup using regular particle arrays. Hereby, we

- demonstrate total light absorption and an overall improvement of the average absorption by up to 20% in the visible spectrum;
- develop an analytical study including both electric and magnetic particle response allowing for rapid evaluation of different material compositions and geometrical setups
  - > Si, Au and Ag nanospheres and nanoshells with the possibility to tune spectral features;
  - > Si particles investigating GaAs and Si as active materials in a SiO_2 matrix;
- suggest simple extensions including multiple particle arrays of the same configuration to cover a broad spectral range or combining different particle types, e. g. shapes or sizes, within a single layer.

Our work provides thus a fast way of estimating the performance of devices composed of particle arrays, which is advantageous for optimizing compositional and geometrical parameters for the fabrication of actual devices.

Random nanoparticle layers exhibit a broad spectrum and a high density of states with overall weak coupling, i. e. mostly scattering. Those plasmonic particle layers (PPLs) are fabricated in a cost efficient way and we have developed a combined numerical and experimental approach in this context, where we

- describe the optical response of random nanoparticle layers using statistical data of the particle size distribution of fabricated samples as an input to our modeling;
  - > set up comparable numerical, quasi-random samples used as a supercell in an otherwise regular structure;
  - > fully capture the particle-particle interaction in the quasi-random intra-cell arrangement and between supercells;
- perform optical characterization and electromagnetic simulation on the exact same random samples exploiting electron beam lithography (EBL) in this dual approach;
  - > achieve excellent agreement on the wavelength position and the value of transmission features;
  - > underestimate experimental broadening of the spectral features in our calculations;
- find that each particle distribution can be adjusted to particle material and shape allowing us to study both metal and dielectric nanostructures for complex optimization tasks.

The method has been applied to predict optical spectra of actual random samples fabricated using the nanosphere self-aggregation (NSA) and by relying only on measured geometrical parameters as an input for the calculations. Our study opens a new methodology for designing optimized geometries of nanophotonic structures, and in particular, samples of nanoparticles as those discussed here to improve the efficiency of optical absorption in photovoltaics.

5 Conclusiones

En la presente tesis se estudian aspectos fundamentales y aplicadas relacionados con excitaciones colectivas en el gas de electrones libres en los metales.

En el primer tema central de esta tesis proporcionamos estrategias para tener en cuenta las interacciones de electrones no locales con enfoques semi-clásicos, que permitan una evaluación rápida de una variedad de nanoestructuras plasmónicas en comparación con métodos *ab initio*. Somos capaces de identificar las expresiones simples no locales que desaparecen en el límite local ($k_{\parallel} \to 0$), que permiten una extensión directa de procedimientos conocidos. Una descripción exacta de las propiedades no locales de nanoestructuras de metal es importante para predecir la respuesta óptica de las moléculas próximas a las superficies de metal y los campos mejorados relacionados y los efectos no lineales acompañados.

El impacto de los efectos no locales se estudia para los siguientes modelos:

- El modelo especular no retardado (SRM) basándose en la función dieléctrica de Mermin que depende de k,
- El modelo hidrodinámico retardado, donde derivamos
  - > Mie coeficientes de dispersión extendidos de esferas de metal y nanocápsulas, comparando el límite retardado de las expresiones con el SRM y permitiendo estudiar los agregados de tales partículas que explotan la teoría de dispersión múltiple;
  - > el análogo no local a los coeficientes de Fresnel para interfaces planas, que se pueden emplear directamente para estudiar complejas estructuras de multicapas planas;
- El régimen electrostática donde proporcionamos una extensión del modelo hidrodinámico incluyendo el desbordamiento de electrones dentro del entorno;
  - > utilizando un enfoque de matriz de transferencia para describir las superficies suaves en términos de perfiles de densidad de electrones realistas;
  - > que demuestra el notable impacto del desbordamiento en el límite local de forma independiente de las interacciones no locales en el gas de electrones, pero incluyendo los perfiles de densidad de electrones suaves;
  - > la introducción de un marco extendida para dar cuenta de la densidad local de estados ópticos (LDOS) colocando un emisor de sonda cerca de una superficie metálica suave.

Estos diferentes enfoques están aplicados y comparados para una variedad de estructuras plasmónicas, es decir

- Esferas, nanocápsulas, dímeros y nano-antenas de tipo Yagi-Uda;
- Estructuras planas, como las superficies metálicas, guías de ondas y películas finas;

– Con consecuencias directas a conceptos ópticos fundamentales, tales como imágenes, sensores y otros campos relacionados con las aplicaciones de la mejora del campo local, así como la guía de luz a escala nanométrica.

Cálculamos la radiación de dispersión secciones transversales, coeficientes de reflexión y transmisión, el LDOS, y además curvas de la dispersión de plasmones para algunas de estas geometrías. Identificamos parámetros estructurales en estos dispositivos hacia la aproximación común local más allá del cual los conceptos ideales de la electrodinámica se comprometieron. Todo esto hacemos en el ámbito de las propiedades no locales en los componentes metálicos involucrados.

La diferenciación explícita entre los efectos del bulk no locales, utilizando límites definidos, y los efectos de borde no locales, incluyendo las distribuciones de densidad de electrones realistas suaves en las superficies metálicas, nos permitió discutir las diferentes contribuciones a efectos comúnmente observados en la nanoescala, tales como el ensanche de la resonancia plasmónica (resultando en una reducción de la mejora de los campos), cambios de frecuencia y canales de atenuación adicionales proporcionadas por las ondas de presión longitudinales de la densidad de los electrones dinámicos. Además, podemos reproducir efectos no locales y otros observados en el experimento que hasta ahora sólo habían sido predecidos por métodos basados en primeros principios.

En conclusión, las principales diferencias entre el modelo local con interfaces abruptas y la evaluación numérica de la densidad de electrones suave no locales para los diferentes tipos de bloques básicos de construcción plasmónicos se encuentran dentro de la propia densidad suave y no en la influencia de los fenómenos no locales en esta descripción. Usando perfiles suaves, se muestran similitudes en todas las geometrías investigadas y difieren significativamente de la respuesta óptica que se encuentra en la aproximación local y también de un modelo no local asumiendo las interfaces abruptas. Los efectos de la no localidad en el bulk se ven contrarrestados por la interfaz suave. Una interfaz suave, sin embargo, conduce al ensanche del plasmón y su atenuación, pero no a un cambio en las posiciones de modo que estudiamos por la comparación de las teorías abruptas y suaves locales.

En resumen, demostramos que el modelo hidrodinámico puede también describir los fenómenos no locales que surgen de la naturaleza cuántica de los electrones libres. Proporciona una comprensión profundida y una evaluación rápida de los sistemas que involucran nanoestructuras sin implicar parámetros libres. Este estudio es especialmente importante para grandes áreas activos relacionados con las aplicaciones de la mejora del campo local para biosensores y en la óptica no lineal. Nuestros resultados abren el camino hacia una descripción exhaustiva y computacionalmente económica de la no localidad de morfologías metálicas arbitrarias.

El segundo tema central está fuertemente orientado a las aplicaciones y focaliza en los efectos colectivos en los ámbitos locales de las capas de partículas regulares y aleatorias con un énfasis en el almacenamiento óptico de datos y la eficiencia de absorción mejorada en las células solares de tercera generación.

Un concepto prometedor para procesar en gran escala estampados de campos cercanos

imprimidos es utilizar monocapas coloidales. En este contexto,

- estudiamos una monocapa dieléctrico hexagonal compacto de tamaño micrométrico de esferas de poliestireno (PS);
- logramos por la nanoimpresión los estampados de campos cercanos ópticos en una película fina del material $Ge_2Sb_2Te_5$ (GST) a través de la ablación por pulsos cortos de un láser varíando las condiciones de la iluminación en términos de
  - > la polarización de la luz incidente;
  - > la rotación la rejilla hexagonal con respecto al plano de incidencia;
  - > el ángulo de incidencia;
  - > tamaño de las partículas y la longitud de onda entrante a través de cálculos de las bandas;
- encontramos excelente concordancia con los datos experimentales mediante cálculos basados en la teoría de la dispersión múltiple para materiales homogéneos regulares;
- discutimos la solidez de los estampados impresados en presencia de pequeños defectos.

Los impresos de los campos cercanos heredan la invariancia traslacional de la monocapa coloidal. Además, el número de los máximos del campo cercano no está limitado por el número de partículas y se puede aumentar mediante la elección adecuada de las condiciones de la iluminación. Este concepto simple pero eficaz es muy adecuado para la nanoestructuración y cartografía de distribuciones de intensidad arbitrarios con una alta resolución espacial, que pueden aplicarse directamente para la fabricación a gran escala sobre otros substratos.

La mejora de la absorción en las células solares asistida por los plasmones se investiga de dos maneras. En primer lugar, aplicamos la configuración de pantalla de Salisbury utilizando capas de partículas regulares. Por la presente,

- demostramos la absorción de luz total y una mejora general de la absorción media hasta en un 20 % en el espectro visible;
- desarrollamos un estudio analítico incluyendo tanto la respuesta eléctrica y magnética de las partículas que permite una rápida evaluación de diferentes composiciones de materiales y configuraciones geométricas, como
  - > nanoesferas y nanocápsulas de Si, Au y Ag y la posibilidad de ajustar las características espectrales;
  - > partículas de Si usando GaAs y Si como materiales activos en una matriz de SiO_2;
- sugerimos extensiones simples que incluyen: varias matrices de partículas de la misma configuración para cubrir un amplio rango espectral o la combinación de diferentes tipos de partículas, por ejemplo, variando la forma u el tamaño dentro de una capa individual.

Nuestro trabajo proporciona de este sentido una forma rápida de estimar el rendimiento de los dispositivos compuestos por capas de partículas, lo cual resulta ventajoso para la optimización de parámetros de composición y geométricos para la fabricación de dispositivos reales.

Las capas de nanopartículas aleatorias exhiben un amplio espectro y una alta densidad de estados con acoplamiento débil en general. Estas capas plasmónicas (PPLs) se fabrican de una manera rentable y desarrollamos un enfoque numérico y experimental combinado en este contexto, en el que

- describimos la respuesta óptica de las capas de nanopartículas aleatorias a partir de datos estadísticos de la distribución de los tamaños de las partículas de muestras fabricadas;
  - > creamos muestras comparables numéricas, cuasi-aleatorios usados como una supercélula en una estructura regular;
  - > captamos plenamente la interacción entre partículas en la capa cuasi-aleatoria con colocación intra-célular y entre las supercélulas;
- realizamos la caracterización óptica y simulación electromagnética en las mismas muestras aleatorias que explotan la litografía por haz de electrones EBL en este enfoque dual;
  - > logramos un excelente acuerdo sobre la posición de longitud de onda y el valor de la transmisión;
  - > subestimamos la ampliación experimental de las características espectrales en nuestros cálculos;
- notamos que cada distribución de partículas se puede ajustar al material y forma de partículas que permite estudiar tanto de metal y nanoestructuras dieléctricas para las tareas de optimización complejos.

Aplicamos el método para predecir espectros ópticos de muestras aleatorias fabricadas en realidad usando la auto-agregación de nanoesferas (NSA) y apoyándose exclusivamente en parámetros geométricos de las muestras experimentales como únicos datos de entrada en nuestros cálculos. Nuestro estudio abre una nueva metodología para el diseño de geometrías optimizadas de estructuras nanofotónicas, y, en particular, muestras de nanopartículas como los discutidos aquí para mejorar la eficiencia de absorción óptica en dispositivos fotovoltaicos.

6 Appendix

When I was in school I liked math because all the problems had answers. Everything else seemed very subjective.

(Lisa Randall)

6.1 Material parameters

Gold and aluminium are employed as representatives for noble and simple metals in our study on the impact of nonlocality induced by a smooth electron density profile. Density profiles are taken from original data[42] and shown in Fig. 6.1(a). The position dependent plasmon frequency is connected to the electron density via $\omega_p = 4\pi e^2 n_0/m_e$. The bulk electron density n_0^B can be determined from the Wigner-Seitz radius r_s given in Fig. 3.9 (a) and in table 6.1 from $1/n_0^B = \frac{4\pi}{3}(r_s)^3$. Bulk parameters are used in optical calculations for the local approximation and the nonlocal model with sharp boundaries.

The dielectric permittivities $\epsilon_\perp = \epsilon_b - \frac{w_p^2}{\omega(\omega+i\gamma_p)}$ are modeled using tabulated data from Ref.[42] for gold for $\epsilon_\perp$ in order to obtain a "measured" ϵ_b and a plasmon frequency and damping of $\omega_p = 8.9\,\text{eV}$ and $\gamma_p = 0.071\,\text{eV}$ respectively. The choice of parameters is motivated by comparing the resulting permitivities to the commenly used approximation of $\epsilon_b = 9 + i0$. In Fig. 6.1 (a) we vary the plasmon frequency to adjust the real part of ϵ_b, and in Fig. 6.1 (b)

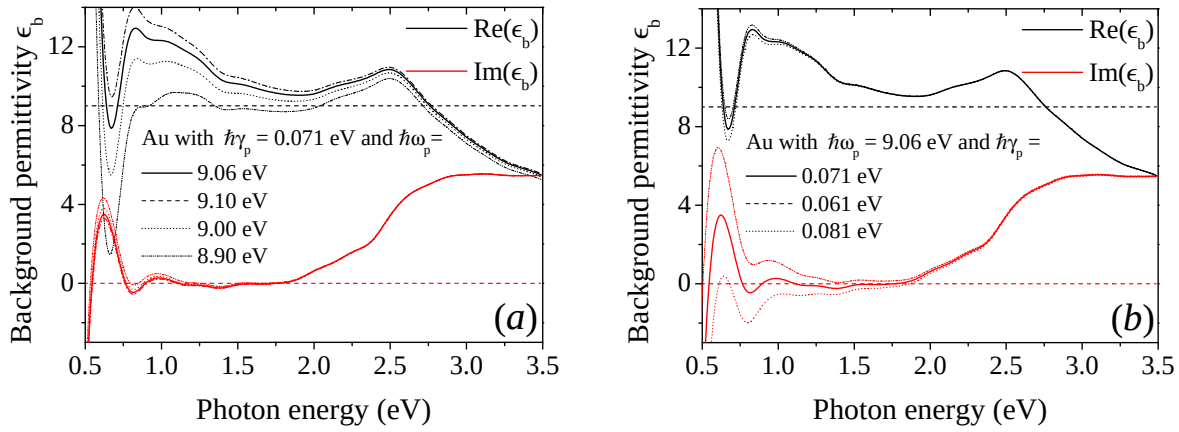

Fig. 6.1: **Real and imaginary part of the background permitivity of gold for varying Drude parameters. (a)** Variation of the plasmon frequency changes the real part significantly. **(b)** Variation of the plasmon damping influences the imaginary part. From this a good fit is given by $\omega_p = 8.9$ eV and $\gamma_p = 0.071$ eV. Dashed horizontal lines indicate the common approximation of $\epsilon_b = 9 + i0$.

Material	ϵ_b	ω_p (eV)	γ_p (eV)	r_s (a.u.)	Sec.	Ref.
Gold (Au)	$\epsilon(\omega)$	8.9-9.0	0.05-0.071	3	3.2	146, 164
Aluminium (Al)	1	15.34	0.5	2.07	3.2	146, 165

Table 6.1: Material parameters used to calculate nonlocal optical response for smooth electron density profiles. The background permittivity $epsilon_b(\omega)$ for gold is obtained from optical data,[146] which yields a value close to 9.

the influence of the plasmon damping on the imaginary part is shown. For aluminium we use $\epsilon_b = 1$, $\omega_p = 15.34\,\text{eV}$ and $\gamma_p = 0.05\,\text{eV}$, in accordance to the spectral position of the surface plasmon for vanishing parallel momenta in the experiments performed in Ref.[165] Notice that the chosen values slighty differ from the ones found directly from the Wigner-Seitz radius.

Parameters used exclusively for the calculation of nonlocal optical response properties are given in table 6.1. Table 6.2 gives an overview of the different material parameters used in the present work together with the source references.

Material	$n + i\kappa$	Sec.	Ref.
$Ge_2Sb_2Te_5$ (GST), crystalline	5.72+4.09 i	4.1.1	196
$Ge_2Sb_2Te_5$ (GST), amorph	4.74+1.45 i	4.1.1	196
Polystyrene (PS)	1.58+0.003i	4.1.1	3
Material	ϵ_b	**Sec.**	**Ref.**
Si	$\epsilon(\omega)$	4.1.2	197
Aluminium (Al)	$\epsilon(\omega)$	4.1.2, 4.2	146
Silver (Ag)	$\epsilon(\omega)$	4.1.2, 4.2	146
SiO_2	2.1	4.1.2, 4.2	
Gold (Au)	$\epsilon(\omega)$	4.1.2	146
GaAs	$\epsilon(\omega)$	4.1.2	197
Si_3N_4 (polycrystalline)	$\epsilon(\omega)$	4.2	198

Table 6.2: Material parameters and sources for local calculations.

6.2 Hydrodynamic pressure for a non-degenerated electron gas

In the Thomas-Fermi theory, the free, degenerate electron gas is associated with a characteristic pressure term p. The internal energy $U = \sum_{\mathbf{k}} \epsilon_{\mathbf{k}} n^F_{\mathbf{k}}$ is locally defined as a sum over all energies.[141, 199, 200] The total number of states of the fermionic system $n = \frac{N}{V}$ is described by a sphere in momentum space with radius $\frac{2\pi}{k_F}$, where k_F is the corresponding Fermi wave vector. With the $T \to 0$ Fermi distribution function this results in

$$n = \frac{g}{V} \sum_{\mathbf{k}} n^F_{\mathbf{k}} = g \frac{4\pi}{3} \left(\frac{k_F}{2\pi} \right)^3 \quad \Rightarrow \quad k_F = \left(\frac{N}{V} \frac{6\pi^2}{g} \right)^{\frac{1}{3}} \tag{6.1}$$

where we account for the degeneration of states with $g = 2s + 1$. With the energy at the Fermi level $\epsilon_F = \frac{\hbar^2 k_F^2}{2m_e}$ and the spin of electrons $s = \frac{1}{2}$ we find

$$\epsilon_F = \frac{\hbar^2}{2m_e}(3\pi^2)^{\frac{2}{3}} n^{\frac{2}{3}}. \tag{6.2}$$

With that, the kinetic internal energy U results in

$$U = \sum_{\mathbf{k}} \epsilon_{\mathbf{k}} n_{\mathbf{k}}^F = \frac{V}{(2\pi)^3}\frac{\hbar^2}{2m_e}\int d^3k k^2 n_{\mathbf{k}}^F = \frac{3}{5}\epsilon_F \frac{4\pi}{3}\frac{k_F^3}{(2\pi)^3} = \frac{3}{5}\epsilon_F N, \tag{6.3}$$

leading to a mean energy per fermionic particle of $U/N = \frac{3}{5}\epsilon_F$. The pressure p of the electron plasma is given by the variation of the kinetic energy with respect to volume $-p = \frac{\partial}{\partial V}U$

$$p = \frac{1}{5}\frac{\hbar^2}{m_e}(3\pi)^{2/3} n^{5/3}. \tag{6.4}$$

Assuming small changes δn in the electron density $n = n_0 + \delta n$ with respect to the equilibrium situation of an unperturbed electron density profile n_0, we find

$$p = \frac{1}{5}\frac{\hbar^2}{m_e}(3\pi)^{2/3} n_0^{5/3} + \frac{1}{3}\frac{\hbar^2}{m_e}(3\pi)^{2/3} n_0^{2/3}\delta n + \mathcal{O}(\delta n^2) \equiv p_0 + \beta_{\mathrm{cl}}^2 \delta n + \mathcal{O}(\delta n^2). \tag{6.5}$$

This defines the nonlocal $\beta_{\mathrm{cl}}^2 = \frac{1}{3}\frac{\hbar^2}{m_e^2}(3\pi)^{2/3} n_0^{2/3} = \frac{1}{3}v_F^2 \approx (p - p_0)/(m_e \delta n)$ from the statistics of a free, non-interacting Fermi gas. Fully taking the quantum nature of electrons into account the prefactor is corrected to $\frac{3}{5}$, as found by Refs.[142,143] . This quantum mechanical result is in agreement with the low momentum limit of the Lindhard dielectric function.

6.3 Mie scattering coefficients in the hydrodynamical model

The parameters used for the analytical calculations are depicted in Fig. 6.2 and consist of the (outer) particle radius a, the dielectric constant of the surrounding medium ϵ_0, the transversal part of the dielectric function $\epsilon_\perp$ in the metal region, and, in case of the nanoshell, an additional inner radius b and the dielectric constant of the core material ϵ_c.

Scattering by a spherical particle

We derive the scattering coefficient t_l^ν for the magnetic ($\nu = M$) and electric ($\nu = E$) scalar function introduced in section 3.1.2. Inside the particle, the field is given by $A_l^\nu j_L$, with $j_L = j_{lm}(k_\perp r)$, and outside the electric scalar field is given by eq. (3.15), namely $j_{lm}(k_0 r) + t_l^\nu h_{lm}^+(k_0 r)$, with unknown parameters A_l^ν and t_l^ν. Exploiting the boundary conditions given in section 3.1.2 for the magnetic scalar function ψ^M at $r = a$, we find the following set of

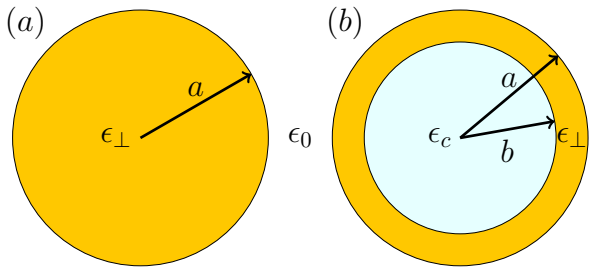

Fig. 6.2: Illustration of the variables used in the calculation of the scattering coefficients of a metallic sphere and a nanoshell.

linear equations

$$A_l^M j_l(\theta_\perp) = j_l(\theta_0) + t_l^M h_l^+(\theta_0), \tag{6.6}$$

$$A_l^M [\theta_\perp j_l(\theta_\perp)]' = [\theta_0 j_l(\theta_0)]' + t_l^M [\theta_0 h_l^+(\theta_0)]', \tag{6.7}$$

where $\theta_0 = ka\sqrt{\epsilon_0}$ and $\theta_\perp = ka\sqrt{\epsilon_\perp}$ and the primes indicate differentiation with respect to the θ variables. The resulting transfer matrix for the magnetic scalar function is

$$t_l^M = \frac{j_l(\theta_0)\theta_\perp j_l'(\theta_\perp) - j_l(\theta_\perp)\theta_0 j_l'(\theta_0)}{j_l(\theta_\perp)\theta_0 h_l^{+\prime}(\theta_0) - h_l^+(\theta_0)\theta_\perp j_l'(\theta_\perp)}. \tag{6.8}$$

This result is the same as the one obtained within local theory, indicating that magnetic modes are not sensitive to nonlocal effects. The scattering matrix for the electric scalar function is more complicated due to the appearance of ψ^L in the metallic region. Here, we find the set of equations

$$A_l^E \epsilon_\perp j_l(\theta_\perp) = \epsilon_0 \left(j_l(\theta_0) + h_l^+(\theta_0) t_l^E \right) \tag{6.9}$$

$$\left(\frac{\eta k}{k_\perp^2 - q^2} \right) \rho_l j_l(qa) + A_l^E [\theta_\perp j_l(\theta_\perp)]' = [\theta_0 j_l(\theta_0)]' + t_l^E [\theta_0 h_l^+(\theta_0)]'. \tag{6.10}$$

The additional boundary condition, eq. (3.19), given by the hydrodynamic equation (see discussion in sections 2.1.2 and 3.1.2) yields a presctiption to calculate ρ_l . This results in

$$\beta^2 \rho_l q j_l'(qa) = \frac{n_0}{k} \rho_l \frac{\eta k}{k'^2 - q^2} q j_L'(qa) + \frac{l(l+1)\omega_p^2}{4\pi a k} A_l^E j_l(\theta_\perp) \tag{6.11}$$

$$\Rightarrow \rho^{\text{ind}} = \frac{\epsilon_\perp}{\epsilon_b} \frac{l(l+1)}{aqk} \frac{\omega_p^2}{4\pi\beta^2} \frac{j_l(\theta_\perp)}{j_l'(qa)} A_l^E. \tag{6.12}$$

This allows us to define a simple, nonlocal parameter $g_l = \frac{l(l+1)j(qa)}{qaj'(qa)} \left(\frac{\epsilon_\perp}{\epsilon_b} - 1 \right)$ with which we can shortly summerize eqs. 6.12 and 6.10 as

$$A_l^E \{ [\theta_\perp j_l(\theta_\perp)]' + g_l \} = [\theta_0 j_l(\theta_0)]' + t_l^E [\theta_0 h_l^+(\theta_0)]'. \tag{6.13}$$

Finally, the scattering coefficient reads:

$$t_l^E = \frac{-\epsilon_\perp j_l(\theta_\perp)[\theta_0 j_l(\theta_0)]' + \epsilon_0 j_l(\theta_0)([\theta_\perp j_l(\theta_\perp)]' + g_l)}{\epsilon_\perp j_l(\theta_\perp)[\theta_0 h_l^+(\theta_0)]' - \epsilon_0 h_l^+(\theta_0)([\theta_\perp j_l(\theta_\perp)]' + g_l)}, \tag{6.14}$$

where, compared to the local theory ($\epsilon_\perp \longrightarrow \epsilon_b$), the only difference is the presence of an additional quantity describing nonlocal behavior of conduction-electron motion.

Scattering by a nanoshell

Another important nanostructure is the coated spherical particle, for which we use the notation of Fig. 6.2. In particluar, we examine metallic coatings on dielectric cores (e. g. glass particles coated with gold) with local dielectric function ϵ_c and radius b. From the above analysis, the elctric ($\nu = E$) and magnetic ($\nu = M$) scalar functions must take the following form inside the three different regions of the system

$$\begin{aligned}
\psi^\nu &= A_l^\nu j_{lm}(k_c r) && r < b, \\
\psi^\nu &= B_l^\nu j_{lm}(k_\perp r) + C_l^\nu h_{lm}^{(+)}(k_\perp r) && b < r < a, \\
\psi^\nu &= j_{lm}(k_0 r) + t_l^\nu h_{lm}^{(+)}(k_0 r), && a < r,
\end{aligned}$$

where $k_c = k\sqrt{\epsilon_c}$ and with unknown amplitudes A_l^ν, B_l^ν and C_l^ν. When boundary conditions are applied for the electric scalar functions, the longitudinal scalar function ψ^L enters at both interfaces. For the magnetic component, the continuity of $\psi^M, \partial(r\psi^M)/\partial r$ leads to the equations

$$\begin{aligned}
A_l^M j_l(k_c b) &= B_l^M j_l(k_\perp b) + C_l^M h_l^{(+)}(k_\perp b) \\
j_l(k_0 a) + t_l^M h_l^{(+)}(k_0 a) &= B_l^M j_l(k_\perp a) + C_l^M h_l^{(+)}(k_\perp a) \\
A_l^M [k_c b j_l(k_c b)]' &= B_l^M [k_\perp b j_l(k_\perp b)]' + C_l^M [k_\perp b h_l^{(+)}(k_\perp b)]' \\
[k_0 a j_l(k_0 a)]' + t_l^M [k_0 a h_l^{(+)}(k_0 a)]' &= B_l^M [k_\perp a j_l(k_\perp a)]' + C_l^M [k_\perp a h_l^{(+)}(k_\perp a)]'.
\end{aligned}$$

This constitutes a system of four linear equations with four unknowns $(A_l^M, B_l^M, C_l^M, t_l^M)$ that can be solved analytically, although in practice it is more convenient to compute t_l^M using linear algebra. Like in the homogeneous sphere, the nanoshell magnetic response is insensitive to nonlocal effects.

Again, the electric part is more complicated because the metal contains longitudinal components of the form

$$\psi^L = -\frac{4\pi k}{\epsilon_b q^2}\left(\rho_l^1 j_{lm}(qr) + \rho_l^2 h_{lm}^+(qr)\right) \qquad b < r < a. \tag{6.15}$$

The boundary conditions together with the additional boundary condition imposed by the

hydrodynamic equation at the two interaces lead to the following system of six linear equations

$$\begin{aligned}
\epsilon_\perp(B_l^E j_l(k_\perp b) + C_l^E h_l^+(k_\perp b)) &= A_l^E \epsilon_c j_l(k_c b) \\
\epsilon_\perp(B_l^E j_l(k_\perp a) + C_l^E h_l^+(k_\perp a)) &= \epsilon_0 j_l(k_\perp a) + \epsilon_0 t_l^E h_l^+(k_\perp a) \\
B_l^E[k_\perp b j_l(k_\perp b)]' + C_l^E[k_\perp b h_l^+(k_\perp b)]' + \frac{\eta k}{k_\perp^2 - q^2}\left(\rho_l^1 j_l(qb) + \rho_l^2 h_l^+(qb)\right) &= A_l^E[k_c b j_l(k_c b)]' \\
B_l^E[k_\perp a j_l(k_\perp a)]' + C_l^E[k_\perp a h_l^+(k_\perp a)]' \quad + \frac{\eta k}{k_\perp^2 - q^2}\left(\rho_l^1 j_l(qa) + \rho_l^2 h_l^+(qa)\right) &= [k_\perp a j_l()]' + \\
t_l^E[k_\perp a h_l^+(k_\perp a)]' & \\
q\beta^2 \frac{\epsilon_b}{\epsilon_\perp}\left(\rho_l^1 j_l'(qa) + \rho_l^2 h_l'^{(+)}(qa)\right) + \frac{l(l+1)\omega_p^2}{4\pi a k}(B_l^E j_l(ka) + C_l^E h_l^+(ka)) &= 0 \\
q\beta^2 \frac{\epsilon_b}{\epsilon_\perp}\left(\rho_l^1 j_l'(qb) + \rho_l^2 h_l'^{(+)}(qb)\right) + \frac{l(l+1)\omega_p^2}{4\pi b k}(B_l^E j_l(kb) + C_l^E h_l^+(kb)) &= 0
\end{aligned}$$

Obviously, we solve this system of six linear equations and six unknowns ($A_l^E, B_l^E, C_l^E, t_l^E$, ρ_l^1, ρ_l^2) numerically to obtain the scattering matrix t_l^E.

6.4 Local density of optical states for nonlocal sharp interfaces

Here, we are in particular interested in the LDOS of a dipole emitter placed on the dielectric (described by permittivity ϵ_0) side, i. e. $z_d > 0$ of a dielectric to nonlocal metal interface at $z = 0$. Then

$$\phi(z)^{\text{ind}} = B\rho(z) + e^{i\mathbf{k}_\parallel \mathbf{R}} \begin{cases} \beta e^{k_\parallel z} + \frac{\phi^{\text{ext}}}{\epsilon_0} & z \geq 0 \\ \alpha e^{-k_\parallel z} & z < 0 \end{cases}, \tag{6.16}$$

$$\rho(z) = e^{i\mathbf{k}_\parallel \mathbf{R}} \begin{cases} 0 & z \geq 0 \\ A e^{iq_0 z} & z < 0 \end{cases}, \tag{6.17}$$

with $B = \frac{4\pi\beta_0^2}{\epsilon_\perp \omega(\omega + i\gamma)}$, cp. eq. (2.25). The induced electric potential is given by

$$\phi^{\text{ind}}(z_d) = e^{i\mathbf{k}_\parallel \mathbf{R}} \beta e^{k_\parallel z_d} + \phi^{\text{ext}}\left(\frac{1}{\epsilon_0} - 1\right), \tag{6.18}$$

where the contribution from the dipole vanishes, if $\epsilon_0 = 1$, which we assume in the dielectric region.

Before deriving analytic expressions for the local density of optical states (LDOS) at planar, sharp interfaces with the surface normal parallel to the z-direction, we give an account on the external potential produced by a unit dipole $\mathbf{d} = \hat{\mathbf{z}}$ at position z_d. Again, we are particularly

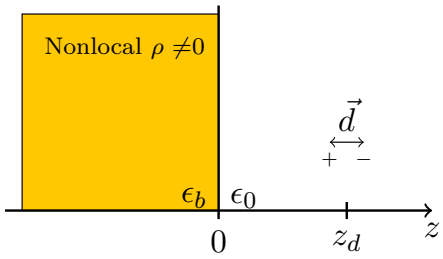

Fig. 6.3: Schematic of the setup to calculate the LDOS for sharp, nonlocal metal surfaces.

interested in the dependence on parallel momentum and thus derive

$$\begin{aligned}
\phi^{\text{ext}} = -\mathbf{d}\nabla\frac{1}{r} &= \int \frac{d^2k_\parallel}{(2\pi)^2}\phi^{\text{ext}}(k_\parallel,\omega)e^{i\mathbf{k}_\parallel\mathbf{R}} \\
&= \int \frac{d^2k_\parallel}{(2\pi)^2}\frac{2\pi}{k_\parallel}(-\mathbf{d}\nabla)e^{i\mathbf{k}_\parallel\mathbf{R}-k_\parallel|z|} \\
&= \int \frac{d^2k_\parallel}{(2\pi)^2}2\pi\,\text{sgn}(z)e^{i\mathbf{k}_\parallel\mathbf{R}-k_\parallel|z|} \\
\Rightarrow\ \phi^{\text{ext}}(k_\parallel,\omega) &= 2\pi\,\text{sgn}(z-z_d)e^{-k_\parallel|z-z_d|}.
\end{aligned} \tag{6.19}$$

For the nonlocal system we first evaluate the additional boundary condition $j_z^{\text{ind}} = 0$ at the interface. We find

$$\begin{aligned}
\beta_0^2\partial_z\rho(z) &= -\frac{\omega_p^2}{4\pi}\partial_z\phi^{\text{ind}}(z_d) \\
iq_0\beta_0^2 A\left(1+\frac{\omega_p^2}{\epsilon_\perp\omega(\omega+i\gamma)}\right) &= \frac{\omega_p^2}{4\pi}\alpha \\
A &= \frac{\omega_p^2}{4\pi\beta_0^2}\frac{k_\parallel}{iq_0}\frac{\epsilon_\perp}{\epsilon_b}\alpha,
\end{aligned} \tag{6.20}$$

which we substitute and by noting the nonlocal parameter in the electrostatic limit, cp. eq. (3.29), $g = \frac{k_\parallel}{iq_0}\left(1-\frac{\epsilon_\perp}{\epsilon_b}\right)$ we obtain

$$\phi(z) = e^{i\mathbf{k}_\parallel\mathbf{R}}\begin{cases}\beta e^{k_\parallel z} + \frac{\phi^{ext}}{\epsilon_0} & z<0\\ \alpha(e^{-k_\parallel z} + ge^{iq_0 z}) & z\geq 0\end{cases} \tag{6.21}$$

Exploiting now the usual boundary conditions, $\phi(z)$ and $\epsilon\partial_z\phi(z)$ being continuous, we find the set of linear equations

$$\beta + \frac{2\pi}{\epsilon_0}e^{-k_\parallel|z_d|} = \alpha(1+g), \tag{6.22}$$

$$\epsilon_0\left(\beta - \frac{2\pi}{\epsilon_0}e^{-k_\parallel|z_d|}\right) = -\epsilon_b\alpha(1-\frac{iq_0}{k_\parallel}g), \tag{6.23}$$

which together yields

$$\beta = \frac{2\pi}{\epsilon_0} e^{-k_\parallel |z_d|} \frac{\epsilon_0(1+g) - \epsilon_\perp}{\epsilon_0(1+g) + \epsilon_\perp} = \frac{2\pi}{\epsilon_0} e^{-k_\parallel |z_d|} r_p^{\mathrm{stat,nl}}. \tag{6.24}$$

The induced potential is thus given by the reflected part of the external potential with contributions from the nonlocality of the metal

$$\phi^{\mathrm{ind}}(z_d) = e^{i\mathbf{k}_\parallel \mathbf{R}} \left(\frac{2\pi}{\epsilon_0} r_p^{\mathrm{stat,nl}} e^{-2k_\parallel |z_d|} + 2\pi \left(\frac{1}{\epsilon_0} - 1 \right) \right). \tag{6.25}$$

The LDOS contribution becomes

$$\rho^{\mathrm{ind}} = \frac{-k_\parallel}{\pi\omega} e^{i\mathbf{k}_\parallel \mathbf{R}} \mathrm{Im} \left\{ \frac{e^{-2k_\parallel |z_d|}}{\epsilon_0} r_p^{stat,nl} - \left(\frac{1}{\epsilon_0} - 1 \right) \right\}. \tag{6.26}$$

Using $\epsilon_0 = 1$ (e. g. air) and neglecting the $e^{i\mathbf{k}_\parallel \mathbf{R}}$ contribution (by e. g. chosing $(x, y) = 0$), this simplifies to

$$\rho^{\mathrm{ind}} = \frac{-k_\parallel}{\pi\omega} e^{-2k_\parallel |z_d|} \mathrm{Im}\{r_p^{\mathrm{stat,nl}}\} > 0. \tag{6.27}$$

Notice that the only difference here, for the dipole in the dielectric medium, is the usage of the nonlocal reflection coefficient, cp. eq. (3.26a).

For the case of the dipole inside the metal region, the expression obtained from the additional boundary conditions involves both the optical coefficient from the induced potential inside the metal and the external potential. This yields a more complicated expression that produces negative LDOS values due to the nonlocal contributions, thus emphasizing the *ad hoc* character of the LDOS definition used here inside a lossy medium (i.e. it is no longer a physically meaningful quantity).

The local LDOS at a sharp metal to dielectric interface is obtained by setting $k_\parallel \to 0$, with the nonlocal parameter $g \to 0$.

6.5 Angular dependence in the absorption of a particle array

In the case of nonmagnetic materials, the analytic theory introduced in section 4.1.2 can be readily extended to account for the angular dependence in the optical response for particle arrays. Materials of low magnetic response are e. g. Ag and Au, but for Si particles the contributions of the magnetic dipole moment can not be neglected.[181]

An incoming electromagnetic wave with wave vector $\mathbf{k} = (\mathbf{k}_\parallel, k_z)$ and $k_z = k\cos\theta$ is assumed, where the angle of incidence is denoted by θ. We derive reflection coefficients for both s- and p-polarizations, and write the electric field as $\mathbf{E}_\sigma = e^{i\mathbf{k}_\parallel \mathbf{R}}(A\hat{\epsilon}_\sigma^+ e^{ik_z z} + B\hat{\epsilon}_\sigma^- e^{-ik_z z})$, with normalized polarization vectors $\hat{\epsilon}_\sigma^\pm$, complex amplitudes A, B and polarization $\sigma = s, p$.

We start from the self-consistent description eq. (2.30), that gives the total dipole moment $\mathbf{p} = \frac{1}{1/\alpha^E - G}\mathbf{E}^{ext}$ of the system accounting for the influence of all other particles in the array. Each particle j at position R_j is contributing with its electric dipole moment p_j to the optical response of the particle array. The self-consistent coupling of all particles is reflected in the properties of the G tensor. For a symmetric environment and $\mathbf{k}_{\|}$ along a principal lattice direction, G is a diagonal tensor[145]

$$G_{jj} = \frac{g_{jj}}{b^3} + i\left(\frac{2\pi}{Ak_z}(k^2 - k_j^2) - \frac{2k^3}{3}\right) \tag{6.28}$$

and the real part $g_{jj} = b^3 Re(G_{jj})$ is determined by the lattice sum procedure after the method of Kambe,[182] see Fig. 6.4, where b is the lattice parameter.

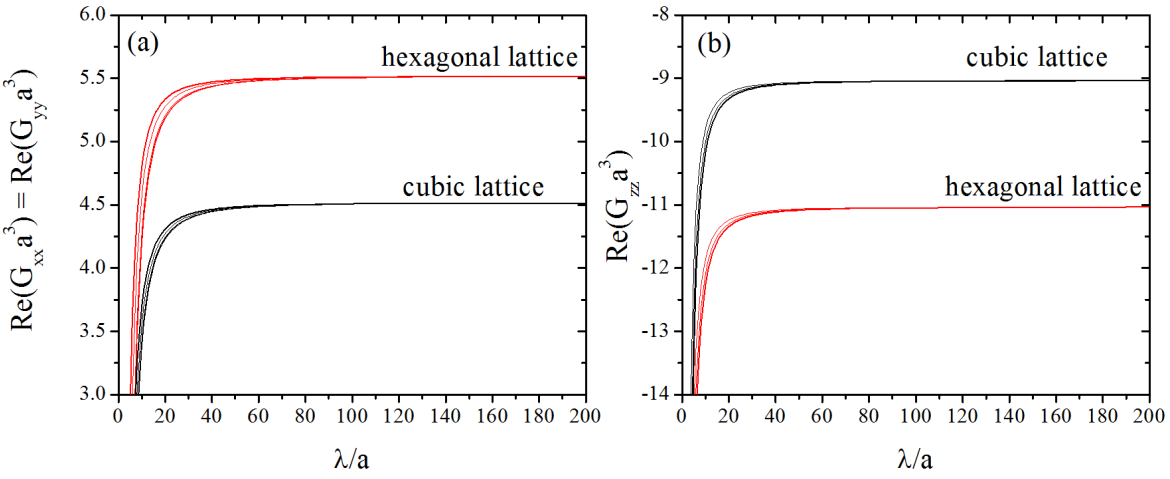

Fig. 6.4: **Values of g_{jj} calculated by a lattice sum procedure for cubic and hexagonal lattices.** (a) We show g_{xx} and g_{yy}, which are equal due to symmetry, and (b) g_{zz} as a function of normalized wavelength λ/b.[145] These values are used as an input to eq. (6.28) and are similar for different b's.

The reflection coefficient of the particle array, depending on the angle of incidence and the polarization of the incoming light, is then derived from

$$r_\sigma = \frac{2\pi i}{Ak_z}k^2(\epsilon_\sigma \cdot \mathbf{p})\frac{1}{E^{ext}}. \tag{6.29}$$

With this expression for the entries of the Green's tensor, eq. (6.29) leads for $\mathbf{k}_{\|} = k\sin\theta\mathbf{e}_x$ and s-polarization to

$$r_s = \frac{2\pi i}{Ak_z}k^2\frac{1}{1/\alpha^E - G_{yy}} = \frac{-1}{1 + \frac{iA\cos\theta}{2\pi k}(1/\alpha^E - \frac{g_{yy}}{b^3} + i2\frac{k^3}{3})} \tag{6.30}$$

and for p-polarization we find likewise

$$\begin{aligned} r_p &= \frac{2\pi i}{Ak_z} k^2 \left[\frac{-\cos^2\theta}{1/\alpha^E - G_{xx}} + \frac{\sin^2\theta}{1/\alpha^E - G_{zz}} \right] \\ &= \frac{1}{1 + \frac{iA}{2\pi k\cos\theta}(1/\alpha^E - \frac{g_{xx}}{b^3} + i2\frac{k^3}{3})} - \frac{1}{1 + \frac{iA\cos\theta}{2\pi k\sin^2\theta}(1/\alpha^E - \frac{g_{zz}}{b^3} + i2\frac{k^3}{3})}. \end{aligned} \tag{6.31}$$

The transmission coefficient is then $t_\sigma = 1 \pm r_\sigma$. Note that the condition $\mathrm{Im}\{1/\alpha^E\} \leq -2\frac{k^3}{3}$ has to be fulfilled.

7 Acknowledgement

> [. . .] because many times a wise questioner makes one consider many things and come to know many others which, if one had not been asked about, one would never have known.
>
> *(Niccolo Machiavelli)*

Watching a great deal of work and efforts come to an end is a great pleasure and it is not without pride that I am looking at my achievements of the past years.

All of this, however, would not have been possible without the continuous assistance, technical and moral support by my friends and colleagues to whom I wish to express my sincere gratitude.

First and foremost, I want to thank my supervisor and "wise questioner", Javier, for this interesting assignment and the many opportunities, exciting travels and responsibilities connected to my participation in his group and the different projects resulting in this thesis. I am indepted for the room for development and the encouraging and critical comments on my performances throughout. I believe, this journey has been a challenge for both of us!

In his theoretical Nanophotonics group, we were never short of amusements, for which I want to thank all the guys who shared this time with me, namely, my fellow PhD students Xesús Bendaña, Alejandro Manjavacas, Ana Asenjo and Iván Silveiro and the live image of what we wanted to achieve given by our post-docs Sukosin Thongrattanasiri, Viktor Myroshnychenko and Johan Christensen.

A fair amount of this work was produced in relation to the FP-7 project LIMA. Here, I would like to thank the whole consortium for their immediate acceptance of me as a an equal scientist despite the little experience I initially brought to the project. I am particularly obliged to the Nanotechnology Center (NTC) of the Universidad Politécnica de Valencia (UPVLC) for hosting me on several occasions. If it would not be for the companionship of James P. Connolly, Guillermo Sánchez, Esther Pérez and Caterina Calatayud, I would not know and love Valencia – and Spanish culture – as much as I do today. Also, their always helpful way successfully led me through the administrative aspects of the project management.

I would like to acknowledge my further co-workers, in particular Paul Kühler and Jan Siegel from the Instituto de Óptica (CSIC), who strongly influenced parts of the present thesis which would not have been accomplished without their inspiring experimental work.

Finally, for a pleasent research stay and a fruitful cooperation in a creative, open minded atmosphere, I would like to thank my hosts at DTU, Denmark, especially N. Asger Mortensen.

If you are still reading this, you see how the scientific experience I gained in the past years has been fueled by many contributions of many generous co-workers. It is often said, you have to climb that montain alone, forgetting to mention the experienced Sherpas you need

along your way, giving advice or taking care for the provisions.

My utmost admiration is reserved for my partner, Robert Hussein, who has not only shared my journey, but is sharing his own and has to deal with all the ups and downs of our strenuous professional life also after working hours. It is thanks to you, that I will miss everything in and around Madrid, because all my memories to this time are inevitably connected to you.

During my errand, I could visit many impressive sites in Spain, showing me different facets of its people, its culture and history. It is connected to the memory of many friends, some already mentioned above, who distracted me in idle times. Spain, this means a certain ring of music and a certain sense of taste that I will never forget and always long for.

8 Bibliography

[1] **Christin David** and F. Javier García de Abajo. Surface plasmon dependence on the electron density profile at metal surfaces. (submitted), 2014.

[2] **Christin David** and F. Javier García de Abajo. Towards total absorption in photovoltaics with the Salisbury screen. (submitted), 2014.

[3] **Christin David**, Paul Kühler, F. Javier García de Abajo, and Jan Siegel. Near-field nanoimprinting using colloidal monolayers. *Opt. Express*, 22(7):8226–8233, 2014.

[4] **Christin David**, N. Asger Mortensen, and Johan Christensen. Perfect imaging, epsilon-near zero phenomena and waveguiding in the scope of nonlocal effects. *Sci. Rep.*, 3:2526, August 2013.

[5] F. Cortés-Juan, C. Chaverri Ramos, J. P. Connolly, **Christin David**, F. J. García de Abajo, J. Hurtado, V. D. Mihailetchi, S. Ponce-Alcántara, and Guillermo Sánchez Plaza. Effect of Ag nanoparticles integrated within antireflection coatings for solar cells. *Journal of Renewable and Sustainable Energy*, 5(3):033116, 2013.

[6] **Christin David**, James P. Connolly, Christian Chaverri Ramos, F. Javier García de Abajo, and Guillermo Sánchez Plaza. Theory of random nanoparticle layers in photovoltaic devices applied to self-aggregated metal samples. *Solar Energy Materials and Solar Cells*, 109(0):294–299, 2013.

[7] **Christin David** and F. Javier García de Abajo. Spatial nonlocality in the optical response of metal nanoparticles. *J. Phys. Chem. C*, 115(40):19470–19475, 2011.

[8] Fp7-248909-lima: Improve photovoltaic efficiency by applying novel effects at the limits of light to matter interaction. www.limaproject.eu.

[9] **Christin David**, Marten Richter, Andreas Knorr, Inez M. Weidinger, and Peter Hildebrandt. Image dipoles approach to the local field enhancement in nanostructured Ag-Au hybrid devices. *The Journal of Chemical Physics*, 132(2):024712, 2010.

[10] Jiu-Ju Feng, U. Gernert, M. Sezer, U. Kuhlmann, D. H. Murgida, **Christin David**, Marten Richter, Andreas Knorr, Peter Hildebrandt, and Inez M. Weidinger. Novel Ag-Au Hybrid Device for Electrochemical SE(R)R Spectroscopy in a Wide Potential and Spectral Range. *Nano Letters*, 9 (1):298–303, 2009.

[11] Sergey V. Gaponenko. Introduction to nanophotonics. *Contemporary Physics*, 52(3), 2011.

[12] Lukas Novotny and Bert Brecht. *Principles of Nano-Optics*. Cambridge University Press, 2006.

[13] A. Polman. Plasmonics applied. *Science*, 322:868, 2008.

[14] Laura Rodríguez-Lorenzo, Ramón A. Álvarez-Puebla, Isabel Pastoriza-Santos, Stefano Mazzucco, Odile Stéphan, Mathieu Kociak, Luis M. Liz-Marzán, and F. Javier García de Abajo. Zeptomol detection through controlled ultrasensitive surface-enhanced raman scattering. *Journal of the American Chemical Society*, 131(13):4616–4618, 2009.

[15] Jon A. Schuller, Edward S. Barnard, Wenshan Cai, Young Chul Jun, Justin S. White, and Mark L. Brongersma. Plasmonics for extreme light concentration and manipulation. *Nat. Mater.*, 9(3):193–204, 2010.

[16] Oleg A. Yeshchenko, Igor M. Dmitruk, Alexandr A. Alexeenko, Mykhaylo Yu. Losytskyy, Andriy V. Kotko, and Anatoliy O. Pinchuk. Size-dependent surface-plasmon-enhanced photoluminescence from silver nanoparticles embedded in silica. *Phys. Rev. B*, 79(23):235438, 2009.

[17] Jin Zhang and Cecilia Noguez. Plasmonic optical properties and applications of metal nanostructures. *Plasmonics*, 3(4):127–150, 2008.

[18] Albert Polman and Harry A. Atwater. Photonic design principles for ultrahigh-efficiency photovoltaics. *Nat. Mater.*, 11(3):174–177, 2012.

[19] J. M. Pitarke, V. M. Silkin, E. V. Chulkov, and P. M. Echenique. Theory of surface plasmons and surface-plasmon polaritons. *Reports on Progress in Physics*, 70(1):1, 2007.

[20] Stefan A. Maier and Harry A. Atwater. Plasmonics: Localization and guiding of electromagnetic energy in metal/dielectric structures. *Journal of Applied Physics*, 98(1), 2005.

[21] Yongcai Qiu, Siu-Fung Leung, Qianpeng Zhang, Bo Hua, Qingfeng Lin, Zhanhua Wei, Kwong-Hoi Tsui, Yuegang Zhang, Shihe Yang, and Zhiyong Fan. Efficient photoelectrochemical water splitting with ultrathin films of hematite on three-dimensional nanophotonic structures. *Nano Lett.*, 2014.

[22] Martin A. Green and Supriya Pillai. Harnessing plasmonics for solar cells. *Nat Photon*, 6(3):130–132, 2012.

[23] Arthur J. Nozik. Nanoscience and nanostructures for photovoltaics and solar fuels. *Nano Letters*, 10(8):2735–2741, 2010.

[24] Katherine A. Willets. Probing local electromagnetic field enhancements on the surface of plasmonic nanoparticles. *Progress in Surface Science*, 87(9/12):209–220, 2012.

[25] Ramón Alvarez-Puebla, Luis M. Liz-Marzán, and F. Javier García de Abajo. Light concentration at the nanometer scale. *The Journal of Physical Chemistry Letters*, 1(16):2428–2434, 2010.

[26] Takayuki Okamoto, Fekhra H'Dhili, and Satoshi Kawata. Towards plasmonic band gap laser. *Applied Physics Letters*, 85(18):3968–3970, 2004.

[27] Koichi Okamoto, Isamu Niki, Alexander Shvartser, Yukio Narukawa, Takashi Mukai, and Axel Scherer. Surface-plasmon-enhanced light emitters based on InGaN quantum wells. *Nat. Mater.*, 3(9):601–605, 2004.

[28] Hideo Iwase, Dirk Englund, and Jelena Vučković. Analysis of the purcell effect in photonic and plasmonic crystals with losses. *Opt. Express*, 18(16):16546–16560, 2010.

[29] Pascal Anger, Palash Bharadwaj, and Lukas Novotny. Enhancement and quenching of single-molecule fluorescence. *Phys. Rev. Lett.*, 96(11):113002, 2006.

[30] G. Vecchi, V. Giannini, and J. Gómez Rivas. Surface modes in plasmonic crystals induced by diffractive coupling of nanoantennas. *Phys. Rev. B*, 80(20):201401, 2009.

[31] Gary F. Walsh and Luca Dal Negro. Enhanced second harmonic generation by photonic-plasmonic fano-type coupling in nanoplasmonic arrays. *Nano Lett.*, 13(7):3111–3117, 2013.

[32] Tobias Utikal, Thomas Zentgraf, Thomas Paul, Carsten Rockstuhl, Falk Lederer, Markus Lippitz, and Harald Giessen. Towards the origin of the nonlinear response in hybrid plasmonic systems. *Phys. Rev. Lett.*, 106(13):133901, 2011.

[33] G.A. Wurtz and A.V. Zayats. Nonlinear surface plasmon polaritonic crystals. *Laser & Photon. Rev.*, 2(3):125–135, 2008.

[34] G. A. Wurtz, R. Pollard, and A. V. Zayats. Optical bistability in nonlinear surface-plasmon polaritonic crystals. *Phys. Rev. Lett.*, 97(5):057402, 2006.

[35] F. Cortés-Juan, C. Chaverri Ramos, J. P. Connolly, **Christin David**, V. D. Mihailetchi, S. Ponce-Alcántara, and Guillermo Sánchez Plaza. Plasmonic nanoparticle integration with Si back contact solar cells. In *28th European Photovoltaic Solar Energy Conference and Exhibition*, pages 375–379, 2013.

[36] U. Kreibig and M. Vollmer. *Optical Properties of Metal Clusters*. 1995.

[37] J. B. Pendry. Negative refraction makes a perfect lens. *Phys. Rev. Lett.*, 85(18):3966–3969, 2000.

[38] S. Anantha Ramakrishna. Physics of negative refractive index materials. *Reports on Progress in Physics*, 68(2):449, 2005.

[39] L. de Broglie. Ondes et quanta. *Cmpt. Rend.*, 177:507–509, 1923.

[40] Max Planck. Über irreversible Strahlungsvorgänge. *Ann. Phys.*, 1:69–122, 1900.

[41] Teravolt at en.wikipedia. licensed under the creative commons attribution 3.0 unported.

[42] N. D. Lang and W. Kohn. Theory of metal surfaces: Charge density and surface energy. *Phys. Rev. B*, 1:4555–4568, 1970.

[43] A. Liebsch. Surface-plasmon dispersion and size dependence of Mie resonance: Silver versus simple metals. *Phys. Rev. B*, 48(15):11317–11328, 1993.

[44] J. Zuloaga, E. Prodan, and P. Nordlander. Quantum description of the plasmon resonances of a nanoparticle dimer. *Nano Letters*, 9:887–891, 2009.

[45] Ruben Esteban, Andrei G. Borisov, Peter Nordlander, and Javier Aizpurua. Bridging quantum and classical plasmonics with a quantum-corrected model. *Nat. Commun.*, 3:825, 2012.

[46] P. T. Leung. Decay of molecules at spherical surfaces: Nonlocal effects. *Phys. Rev. B*, 42(12):7622–7625, 1990.

[47] Kevin J. Savage, Matthew M. Hawkeye, Ruben Esteban, Andrei G. Borisov, Javier Aizpurua, and Jeremy J. Baumberg. Revealing the quantum regime in tunnelling plasmonics. *Nature*, 491(7425):574–577, 2012.

[48] J. Lermé, B. Palpant, B. Prével, E. Cottancin, M. Pellarin, M. Treilleux, J. L. Vialle, A. Perez, and M. Broyer. Optical properties of gold metal clusters: A time-dependent local-density-approximation investigation. *Eur. Phys. J. D*, 4:95–108, 1998.

[49] Jorge Zuloaga, Emil Prodan, and Peter Nordlander. Quantum plasmonics: Optical properties and tunability of metallic nanorods. *ACS Nano*, 4(9):5269–5276, 2010.

[50] A. I. Fernández-Domínguez, A. Wiener, F. J. García-Vidal, S. A. Maier, and J. B. Pendry. Transformation-optics description of nonlocal effects in plasmonic nanostructures. *Phys. Rev. Lett.*, 108(10):106802, 2012.

[51] E. M. Purcell, H. C. Torrey, and R. V. Pound. Resonance absorption by nuclear magnetic moments in a solid. *Phys. Rev.*, 69(1-2):37–38, 1946.

[52] Z. Fatih Öztürk, Sanshui Xiao, Min Yan, Martijn Wubs, Antti-Pekka Jauho, and N. Asger Mortensen. Field enhancement at metallic interfaces due to quantum confinement. *Journal of Nanophotonics*, 5(1):051602, 2011.

[53] Gustav Mie. Beiträge zur Optik trüber Medien, speziell kolloidaler Metallösungen. *Ann. Phys.*, 330(3):377–445, 1908.

[54] R. Ruppin. Optical properties of spatially dispersive dielectric spheres. *J. Opt. Soc. Am.*, 71(6):755–758, 1981.

[55] B. B. Dasgupta and R. Fuchs. Polarizability of a small sphere including nonlocal effects. *Phys. Rev. B*, 24:554–561, 1981.

[56] R. Ruppin. Reflectivity of a nonlocal dielectric with an excitonic surface potential. *Phys. Rev. B*, 29(4):2232–2237, 1984.

[57] R. Ruppin and R. Englman. Optical properties of nonlocal dielectrics independent of additional boundary conditions. *Phys. Rev. Lett.*, 53(17):1688–1691, 1984.

[58] Ronald Fuchs and Francisco Claro. Multipolar response of small metallic spheres: Nonlocal theory. *Phys. Rev. B*, 35(8):3722–3727, 1987.

[59] R. Rojas, F. Claro, and R. Fuchs. Nonlocal response of a small coated sphere. *Phys. Rev. B*, 37:6799–6808, 1988.

[60] R. Ruppin. Optical absorption by excitons in microcrystals. *Journal of Physics and Chemistry of Solids*, 50(9):877–882, 1989.

[61] R. Ruppin. Optical absorption by a small sphere above a substrate with inclusion of nonlocal effects. *Phys. Rev. B*, 45(19):11209–11215, 1992.

[62] R. Ruppin. Extinction properties of thin metallic nanowires. *Optics Communications*, 190:205–209, 2001.

[63] F. J. García de Abajo. Nonlocal effects in the plasmons of strongly interacting nanoparticles, dimers, and waveguides. *J. Phys. Chem. C*, 112:17983–17987, 2008.

[64] Javier Aizpurua and Alberto Rivacoba. Nonlocal effects in the plasmons of nanowires and nanocavities excited by fast electron beams. *Phys. Rev. B*, 78(3):035404, 2008.

[65] Jeffrey M. McMahon, Stephen K. Gray, and George C. Schatz. Nonlocal dielectric effects in core-shell nanowires. *J. Phys. Chem. C*, 114(38):15903–15908, 2010.

[66] Jeffrey M. McMahon, Stephen K. Gray, and George C. Schatz. Optical properties of nanowire dimers with a spatially nonlocal dielectric function. *Nano Lett.*, 10(9):3473–3481, 2010.

[67] Jeffrey M. McMahon, Stephen K. Gray, and George C. Schatz. Calculating nonlocal optical properties of structures with arbitrary shape. *Phys. Rev. B*, 82(3):035423, 2010.

[68] J. M. McMahon, S. K. Gray, and G. C. Schatz. Nonlocal optical response of metal nanostructures with arbitrary shape. *Phys. Rev. Lett.*, 103:097403, 2009.

[69] Søren Raza, Giuseppe Toscano, Antti-Pekka Jauho, Martijn Wubs, and N. Asger Mortensen. Unusual resonances in nanoplasmonic structures due to nonlocal response. *Phys. Rev. B*, 84(12):121412, 2011.

[70] Giuseppe Toscano, Søren Raza, Antti-Pekka Jauho, N. Asger Mortensen, and Martijn Wubs. Modified field enhancement and extinction by plasmonic nanowire dimers due to nonlocal response. *Opt. Express*, 20(4):4176–4188, 2012.

[71] G. Toscano, S. Raza, S. Xiao, M. Wubs, A.-P. Jauho, S. I. Bozhevolnyi, and N. A. Mortensen. Surface-enhanced raman spectroscopy: nonlocal limitations. *Opt. Lett.*, 37(13):2538–2540, 2012.

[72] G. Toscano, S. Raza, W. Yan, C. Jeppesen, S. Xiao, M. Wubs, A.-P. Jauho, S.I. Bozhevolnyi, and N.A. Mortensen. Nonlocal response in plasmonic waveguiding with extreme light confinement. *Nanophotonics*, 2(3):167–172, 2012.

[73] Aeneas Wiener, Antonio I. Fernández-Domínguez, Andrew P. Horsfield, John B. Pendry, and Stefan A. Maier. Nonlocal effects in the nanofocusing performance of plasmonic tips. *Nano Lett.*, 12:3308–3314, 2012.

[74] Wei Yan, Martijn Wubs, and N. Asger Mortensen. Hyperbolic metamaterials: Nonlocal response regularizes broadband supersingularity. *Phys. Rev. B*, 86(20):205429, 2012.

[75] Søren Raza, Thomas Christensen, Martijn Wubs, Sergey I. Bozhevolnyi, and N. Asger Mortensen. Nonlocal response in thin-film waveguides: Loss versus nonlocality and breaking of complementarity. *Phys. Rev. B*, 88(11):115401, 2013.

[76] Domenico de Ceglia, Salvatore Campione, Maria Antonietta Vincenti, Filippo Capolino, and Michael Scalora. Low-damping epsilon-near-zero slabs: Nonlinear and nonlocal optical properties. *Phys. Rev. B*, 87(15):155140, 2013.

[77] Yu Luo, A. I. Fernandez-Dominguez, Aeneas Wiener, Stefan A. Maier, and J. B. Pendry. Surface plasmons and nonlocality: A simple model. *Phys. Rev. Lett.*, 111(9):093901, 2013.

[78] Thomas Christensen, Wei Yan, Søren Raza, Antti-Pekka Jauho, N. Asger Mortensen, and Martijn Wubs. Nonlocal response of metallic nanospheres probed by light, electrons, and atoms. *ACS Nano*, 8(2):1745–1758, 2014.

[79] Jonathan A. Scholl, Ai Leen Koh, and Jennifer A. Dionne. Quantum plasmon resonances of individual metallic nanoparticles. *Nature*, 483(7390):421–427, 2012.

[80] C. Ciracì, R. T. Hill, J. J. Mock, Y. Urzhumov, A. I. Fernández-Domínguez, S. A. Maier, J. B. Pendry, A. Chilkoti, and D. R. Smith. Probing the ultimate limits of plasmonic enhancement. *Science*, 337(6098):1072–1074, 2012.

[81] Søren Raza, Nicolas Stenger, Shima Kadkhodazadeh, Søren V. Fischer, Natalie Kostesha, Antti-Pekka Jauho, Andrew Burrows, Martijn Wubs, and N. Asger Mortensen. Blueshift of the surface plasmon resonance in silver nanoparticles studied with EELS. *Journal of Nanophotonics*, 2:131, 2013.

[82] Isaac Newton. *Opticks*. 1704.

[83] Lord Rayleigh. Xvii. on the maintenance of vibrations by forces of double frequency, and on the propagation of waves through a medium endowed with a periodic structure. *Philosophical Magazine Series 5*, 24(147):145–159, August 1887.

[84] Euan Mcleod and Craig B. Arnold. Subwavelength direct-write nanopatterning using optically trapped microspheres. *Nat Nano*, 3(7):413–417, 2008.

[85] Xu A. Zhang, Jonathan Elek, and Chih-Hao Chang. Three-dimensional nanolithography using light scattering from colloidal particles. *ACS Nano*, 7(7):6212–6218, 2013.

[86] Arvind Sundaramurthy, P. James Schuck, Nicholas R. Conley, David P. Fromm, Gordon S. Kino, and W. E. Moerner. Toward nanometer-scale optical photolithography: Utilizing the near-field of bowtie optical nanoantennas. *Nano Lett.*, 6(3):355–360, 2006.

[87] Ignacio Marín-Fabiani, Jan Siegel, Stephen Riedel, Johannes Boneberg, Tiberio A. Ezquerra, and Aurora Nogales. Nanostructuring thin polymer films with optical near fields. *ACS Appl. Mater. Interfaces*, 5(21):11402–11408, 2013.

[88] Osamu Watanabe, Taiji Ikawa, Makoto Hasegawa, Masaaki Tsuchimori, and Yoshimasa Kawata. Nanofabrication induced by near-field exposure from a nanosecond laser pulse. *Applied Physics Letters*, 79(9):1366–1368, 2001.

[89] Z. B. Wang, M. H. Hong, B. S. Luk'yankchuk, Y. Lin, Q. F. Wang, and T. C. Chong. Angle effect in laser nanopatterning with particle-mask. *Journal of Applied Physics*, 96(11):6845–6850, 2004.

[90] D. Brodoceanu, L. Landström, and D. Bäuerle. Laser-induced nanopatterning of silicon with colloidal monolayers. 86(3):313–314, 2007.

[91] Tetsuo Sakai, Nikolay Nedyalkov, and Minoru Obara. Positive and negative nanohole-fabrication on glass surface by femtosecond laser with template of polystyrene particle array. *Journal of Physics D: Applied Physics*, 40(7):2102, 2007.

[92] Antonio Pereira, David Grojo, Mohamed Chaker, Philippe Delaporte, Daniel Guay, and Marc Sentis. Laser-fabricated porous alumina membranes for the preparation of metal nanodot arrays. *Small*, 4(5):572–576, 2008.

[93] Rodica Morarescu, Lars Englert, Branko Kolaric, Pascal Damman, Renaud A. L. Vallee, Thomas Baumert, Frank Hubenthal, and Frank Trager. Tuning nanopatterns on fused silica substrates: a theoretical and experimental approach. *J. Mater. Chem.*, 21:4076–4081, 2011.

[94] Fanghui Ren, Jeremy Campbell, Xiangyu Wang, Gregory L. Rorrer, and Alan X. Wang. Enhancing surface plasmon resonances of metallic nanoparticles by diatom biosilica. *Opt. Express*, 21(13):15308–15313, 2013.

[95] EEA-NEA OECD. Projected costs of generating electricity. Technical report, 2010.

[96] Brian A. Gregg. Excitonic solar cells. *The Journal of Physical Chemistry B*, 107(20):4688–4698, 2003.

[97] Arthur J. Nozik. Multiple exciton generation in semiconductor quantum dots. *Chemical Physics Letters*, 457(1-3):3–11, 2008.

[98] Zhizhong Yuan, Georg Pucker, Alessandro Marconi, Fabrizio Sgrignuoli, Aleksei Anopchenko, Yoann Jestin, Lorenza Ferrario, Pierluigi Bellutti, and Lorenzo Pavesi. Silicon nanocrystals as a photoluminescence down shifter for solar cells. *Solar Energy Materials and Solar Cells*, 95(4):1224–1227, 2011.

[99] Martin A. Green, Keith Emery, Yoshihiro Hishikawa, Wilhelm Warta, and Ewan D. Dunlop. Solar cell efficiency tables (version 42). *Prog. Photovolt: Res. Appl.*, 21(5):827–837, 2013.

[100] J. P. Connolly, **Christin David**, P. Rodríguez, A. Griol, P. Welti, L. Bellières, J. Ayucar, J. Hurtado, R. Lopez, G. Sánchez Plaza, and F. J. García de Abajo. Analysis of plasmonic nanoparticle fabrication techniques for efficient integration in photovoltaic devices. In *25th European Photovoltaic Solar Energy Conference and Exhibition / 5th World Conference on Photovoltaic Energy Conversion*, pages 773–776, 2010.

[101] J. P. Connolly. The lima project. *Public service Review: Europe*, 24, 2012.

[102] Vivian E. Ferry, Marc A. Verschuuren, Hongbo B. T. Li, Ruud E. I. Schropp, Harry A. Atwater, and Albert Polman. Improved red-response in thin film a-Si:H solar cells with soft-imprinted plasmonic back reflectors. *Appl. Phys. Lett.*, 95(18):183503–3, 2009.

[103] Harry A. Atwater and Albert Polman. Plasmonics for improved photovoltaic devices. *Nature Materials*, 9(3):205–213, 2010.

[104] Michael G. Deceglie, Vivian E. Ferry, A. Paul Alivisatos, and Harry A. Atwater. Design of nanostructured solar cells using coupled optical and electrical modeling. *Nano Lett.*, 12(6):2894–2900, 2012.

[105] Ragip A. Pala, Justin White, Edward Barnard, John Liu, and Mark L. Brongersma. Design of plasmonic thin-film solar cells with broadband absorption enhancements. *Adv. Mater.*, 21(34):3504–3509, 2009.

[106] Vivian E. Ferry, Marc A. Verschuuren, Hongbo B. T. Li, Ewold Verhagen, Robert J. Walters, Ruud E. I. Schropp, Harry A. Atwater, and Albert Polman. Light trapping in ultrathin plasmonic solar cells. *Opt. Express*, 18(S2):A237–A245, 2010.

[107] Koray Aydin, Vivian E. Ferry, Ryan M. Briggs, and Harry A. Atwater. Broadband polarization-independent resonant light absorption using ultrathin plasmonic super absorbers. *Nature Communications*, 2:517, 2011.

[108] Jonathan Grandidier, Dennis M. Callahan, Jeremy N. Munday, and Harry A. Atwater. Light absorption enhancement in thin-film solar cells using whispering gallery modes in dielectric nanospheres. *Adv. Mater.*, 23(10):1272–1276, 2011.

[109] P. Spinelli, V. E. Ferry, J. van de Groep, M. van Lare, M. A. Verschuuren, R. E. I. Schropp, H. A. Atwater, and A. Polman. Plasmonic light trapping in thin-film Si solar cells. *Journal of Optics*, 14(2):024002, 2012.

[110] Vivian E. Ferry, Marc A. Verschuuren, M. Claire van Lare, Ruud E. I. Schropp, Harry A. Atwater, and Albert Polman. Optimized spatial correlations for broadband light trapping nanopatterns in high efficiency ultrathin film a-Si:H solar cells. *Nano Lett.*, 11(10):4239–4245, 2011.

[111] Eli Yablonovitch. Statistical ray optics. *J. Opt. Soc. Am.*, 72(7):899–907, 1982.

[112] Emmanuel Van Kerschaver and Guy Beaucarne. Back-contact solar cells: a review. *Prog. Photovolt: Res. Appl.*, 14(2):107–123, 2006.

[113] G. Galbiati, V. D. Mihailetchi, A. Halm, R. Roescu, and R. Kopecek. Results on n-type IBC solar cells using industrial optimized techniques in the fabrication processing. *Energy Procedia*, 8(0):421–426, 2011.

[114] Jeremy N. Munday and Harry A. Atwater. Large integrated absorption enhancement in plasmonic solar cells by combining metallic gratings and antireflection coatings. *Nano Letters*, 11(6):2195–2201, 2011.

[115] P. Spinelli, M. A. Verschuuren, and A. Polman. Broadband omnidirectional antireflection coating based on subwavelength surface Mie resonators. *Nature Communications*, 3:692, 2012.

[116] Martin A. Green, Keith Emery, Yoshihiro Hishikawa, Wilhelm Warta, and Ewan D. Dunlop. Solar cell efficiency tables (version 39). *Prog. Photovolt: Res. Appl.*, 20(1):12–20, 2012.

[117] Vivian E. Ferry, Luke A. Sweatlock, Domenico Pacifici, and Harry A. Atwater. Plasmonic nanostructure design for efficient light coupling into solar cells. *Nano Lett.*, 8(12):4391–4397, 2008.

[118] K. R. Catchpole and A. Polman. Plasmonic solar cells. *Opt. Express*, 16(26):21793–21800, 2008.

[119] K. R. Catchpole and A. Polman. Design principles for particle plasmon enhanced solar cells. *Appl. Phys. Lett.*, 93(19):191113–3, 2008.

[120] Sang Eon Han and Gang Chen. Optical absorption enhancement in silicon nanohole arrays for solar photovoltaics. *Nano Lett.*, 10(3):1012–1015, 2010.

[121] M. D. Kelzenberg, S. W. Boettcher, J. A. Petykiewicz, D. B. Turner-Evans, M. C. Putnam, E. L. Warren, J. M. Spurgeon, R. M. Briggs, N. S. Lewis, and H. A. Atwater. Enhanced absorption and carrier collection in si wire arrays for photovoltaic applications. *Nat. Mater.*, 9:239, 2010.

[122] S. Pillai, F. J. Beck, K. R. Catchpole, Z. Ouyang, and M. A. Green. The effect of dielectric spacer thickness on surface plasmon enhanced solar cells for front and rear side depositions. *J. Appl. Phys.*, 109(7):073105–8, 2011.

[123] S Mokkapati, F J Beck, R de Waele, A Polman, and K R Catchpole. Resonant nano-antennas for light trapping in plasmonic solar cells. *Journal of Physics D: Applied Physics*, 44(18):185101, 2011.

[124] Fiona J. Beck, Sudha Mokkapati, and Kylie R. Catchpole. Light trapping with plasmonic particles: beyond the dipole model. *Opt. Express*, 19(25):25230–25241, 2011.

[125] F. J. Beck, E. Verhagen, S. Mokkapati, A. Polman, and K. R. Catchpole. Resonant SPP modes supported by discrete metal nanoparticles on high-index substrates. *Opt. Express*, 19(S2):A146–A156, 2011.

[126] Dennis M. Callahan, Jeremy N. Munday, and Harry A. Atwater. Solar cell light trapping beyond the ray optic limit. *Nano Lett.*, 12(1):214–218, 2011.

[127] Yanxia Cui, Kin Hung Fung, Jun Xu, Hyungjin Ma, Yi Jin, Sailing He, and Nicholas X. Fang. Ultrabroadband light absorption by a sawtooth anisotropic metamaterial slab. *Nano Lett.*, 12(3):1443–1447, 2012.

[128] A. Basch, F. J. Beck, T. Söderström, S. Varlamov, and K. R. Catchpole. Combined plasmonic and dielectric rear reflectors for enhanced photocurrent in solar cells. *Appl. Phys. Lett.*, 100(24):243903–5, 2012.

[129] Angelika Basch, Fiona Beck, Thomas Söderström, Sergey Varlamov, and Kylie R. Catchpole. Enhanced light trapping in solar cells using snow globe coating. *Prog. Photovolt: Res. Appl.*, 20(7):837–842, 2012.

[130] J. D. Jackson. *Classical Electrodynamics*. John Wiley & Sons, Inc., 1976.

[131] F. J. García de Abajo and A. Howie. Retarded field calculation of electron energy loss in inhomogeneous dielectrics. *Phys. Rev. B*, 65(11):115418, 2002.

[132] F. J. García de Abajo. Multiple scattering of radiation in clusters of dielectrics. *Phys. Rev. B*, 60:6086–6102, 1999.

[133] V. Myroshnychenko, J. Rodríguez-Fernández, I. Pastoriza-Santos, A. M. Funston, C. Novo, P. Mulvaney, L. M. Liz-Marzán, and F. J. García de Abajo. Modelling the optical response of gold nanoparticles. *Chem. Soc. Rev.*, 37:1792–1805, 2008.

[134] C. F. Bohren and D. R. Huffman. *Absorption and Scattering of Light by Small Particles*. Wiley, New York, 1983.

[135] U. Kreibig and C. v. Fragstein. The limitation of electron mean free path in small silver particles. *Z. Physik*, 224:307–323, 1969.

[136] H. Hövel, S.Fritz, A. Hilger, U. Kreibig, and M. Vollmer. Width of cluster plasmon resonances: Bulk dielectric functions and chemical interface damping. *Phys. Rev. B*, 48, No. 24:18178–18188, 1993.

[137] L. Genzel, T. P. Martin, and U. Kreibig. Dielectric function and plasma resonances of small metal particles, 1975.

[138] N. D. Mermin. Lindhard dielectric function in the relaxation-time approximation. *Phys. Rev. B*, 1:2362–2363, 1970.

[139] F. Bloch. Zur Bremsung rasch bewegter Teilchen beim Durchgang durch Materie. *Z. Phys.*, 81:363–376, 1933.

[140] F. J. García de Abajo. Optical excitations in electron microscopy. *Rev. Mod. Phys.*, 82:209–275, 2010.

[141] K. Huang. *Statistical Mechanics*. Wiley, New York, 1963.

[142] D. Pines and D. Bohm. A collective description of electron interactions: II. collective vs individual particle aspects of the interactions. *Phys. Rev.*, 85:338–353, 1952.

[143] R. H. Ritchie. Plasma losses by fast electrons in thin films. *Phys. Rev.*, 106:874–881, 1957.

[144] R. Ruppin. Effect of non-locality on nanofocusing of surface plasmon field intensity in a conical tip. *Physics Letters A*, 340:299–302, 2005.

[145] Sukosin Thongrattanasiri, Frank H. L. Koppens, and F. Javier García de Abajo. Complete optical absorption in periodically patterned graphene. *Phys. Rev. Lett.*, 108(4):047401, 2012.

[146] P. B. Johnson and R. W. Christy. Optical constants of noble metals. *Phys. Rev. B*, Vol. 6:4370–4379, 1972.

[147] F. J. García de Abajo. Colloquium: Light scattering by particle and hole arrays. *Rev. Mod. Phys.*, 79(4):1267–1290, 2007.

[148] N. Stefanou, V. Yannopapas, and A. Modinos. Heterostructures of photonic crystals: frequency bands and transmission coefficients. *Computer Physics Communications*, 113(1):49–77, 1998.

[149] N. Stefanou, V. Yannopapas, and A. Modinos. Multem 2: A new version of the program for transmission and band-structure calculations of photonic crystals. *Computer Physics Communications*, 132:189–196, 2000.

[150] R. Sainidou, N. Stefanou, I.E. Psarobas, and A. Modinos. A layer-multiple-scattering method for phononic crystals and heterostructures of such. *Computer Physics Communications*, 166(3):197–240, 2005.

[151] M. Danckwerts and L. Novotny. Optical frequency mixing at coupled gold nanoparticles. *Phys. Rev. Lett.*, 98:026104, 2007.

[152] P. S. Kumar, I. Pastoriza-Santos, B. Rodríguez-González, F. J. García de Abajo, and L. M. Liz-Marzán. High-yield synthesis and optical response of gold nanostars. *Nanotechnology*, 19:015606, 2008.

[153] E. Prodan, C. Radloff, N. J. Halas, and P. Nordlander. A hybridization model for the plasmon response of complex nanostructures. *Science*, 302:419–422, 2003.

[154] E. Prodan, P. Nordlander, and N. J. Halas. Electronic structure and optical properties of gold nanoshells. *Nano Lett.*, 3:1411–1415, 2003.

[155] J. Renger, R. Quidant, N. van Hulst, and L. Novotny. Surface-enhanced nonlinear four-wave mixing. *Phys. Rev. Lett.*, 104:046803, 2010.

[156] Ivan A. Larkin and Mark I. Stockman. Imperfect perfect lens. *Nano Lett.*, 5(2):339–343, January 2005.

[157] Søren Raza, Thomas Christensen, Martijn Wubs, Sergey I. Bozhevolnyi, and N. Asger Mortensen. Nonlocal response in thin-film waveguides: loss versus nonlocality and breaking of complementarity. *arXiv:1305.1185*, 2013.

[158] Domenico de Ceglia, Salvatore Campione, Maria Antonietta Vincenti, Filippo Capolino, and Michael Scalora. Low-damping epsilon-near-zero slabs: nonlinear and nonlocal optical properties. *physics optics: arXiv:1302.2392*, 2013.

[159] N. A. Mortensen, S. Raza, M. Wubs, T. Søndergaard, and S. I. Bozhevolnyi. A generalized non-local optical response theory for plasmonic nanostructures. *Nat. Commun.*, 5:3809, 2014.

[160] R. H. Ritchie and A. L. Marusak. The surface plasmon dispersion relation for an electron gas. *Surface Science*, 4:234–240, 1966.

[161] A. Messiah. *Quantum Mechanics*. North-Holland: New York, 1966.

[162] Francis E. Low. *Classical Field Theory - Electromagnetism and Gravitation*. Wiley-VCH Verlag, 1997.

[163] A.D. Boardman and R. Ruppin. The boundary conditions between spatially dispersive media. *Surface Science*, 112:153–167, 1981.

[164] A. Politano, V. Formoso, and G. Chiarello. Dispersion and damping of gold surface plasmon. *Plasmonics*, 3(4):165–170, 2008.

[165] Gennaro Chiarello, Vincenzo Formoso, Anna Santaniello, Elio Colavita, and Luigi Papagno. Surface-plasmon dispersion and multipole surface plasmons in Al(111). *Phys. Rev. B*, 62(19):12676–12679, 2000.

[166] N. W. Ashcroft and D. Mermin. *Solids State Physics*. Saunder's College Publishing, 1976.

[167] John D. Joannopoulos, Steven G. Johnson, Joshua N. Winn, and Robert D. Meade. *Photonic Crystals: Molding the Flow of Light (Second Edition)*. Princeton University Press, 2 edition, 2008.

[168] P. Kühler, F. J. García de Abajo, J. Solis, M. Mosbacher, P. Leiderer, C.N. Afonso, and J. Siegel. Imprinting the optical near field of microstructures with nanometer resolution. *Small*, 5(16):1825–1829, 2009.

[169] Noboru Yamada, Eiji Ohno, Kenichi Nishiuchi, Nobuo Akahira, and Masatoshi Takao. Rapid-phase transitions of GeTe-Sb_2Te_3 pseudobinary amorphous thin films for an optical disk memory. *J. Appl. Phys.*, 69(5):2849–2856, 1991.

[170] J. Siegel, A. Schropp, J. Solis, C. N. Afonso, and M. Wuttig. Rewritable phase-change optical recording in $Ge_2Sb_2Te_5$ films induced by picosecond laser pulses. *Appl. Phys. Lett.*, 84(13):2250–2252, 2004.

[171] J. Siegel, W. Gawelda, D. Puerto, C. Dorronsoro, J. Solis, C. N. Afonso, J. C. G. de Sande, R. Bez, A. Pirovano, and C. Wiemer. Amorphization dynamics of $Ge_2Sb_2Te_5$ films upon nano- and femtosecond laser pulse irradiation. *J. Appl. Phys.*, 103(2):023516–7, 2008.

[172] Z. B. Wang, W. Guo, B. Luk'yankchuk, D.J. Whitehead, L. Li, and Z. Liu. Optical near-field interaction between neighbouring micro/nano-particles. *J. Laser Micro/Nanoeng.*, 3 (1):14–18, 2008.

[173] T. Miyanishi, Y. Tsunoi, M. Terakawa, and M. Obara. High-intensity near-field generation for silicon nanoparticle arrays with oblique irradiation for large-area high-throughput nanopatterning. 107(2):323–332, 2012.

[174] L. Li, W. Guo, Z. B. Wang, Z. Liu, D. Whitehead, and B. Luk'yanchuk. Large-area laser nano-texturing with user-defined patterns. *Journal of Micromechanics and Microengineering*, 19(5):054002, 2009.

[175] Paul Kühler, F. Javier García de Abajo, Philipp Leiprecht, Andreas Kolloch, Javier Solis, Paul Leiderer, and Jan Siegel. Quantitative imaging of the optical near field. *Opt. Express*, 20(20):22063–22078, 2012.

[176] W. W. Salisbury. Absorbent body for electromagnetic waves, 1952.

[177] R. L. Fante and M. T. McCormack. Reflection properties of the salisbury screen. *IEEE Trans. Antennas Propag.*, 36:1443, 1988.

[178] Hugen Yan, Xuesong Li, Bhupesh Chandra, George Tulevski, Yanqing Wu, Marcus Freitag, Wenjuan Zhu, Phaedon Avouris, and Fengnian Xia. Tunable infrared plasmonic devices using graphene/insulator stacks. *Nature Nanotechnology*, 7:330–334, 2012.

[179] Xianliang Liu, Talmage Tyler, Tatiana Starr, Anthony F. Starr, Nan Marie Jokerst, and Willie J. Padilla. Taming the blackbody with infrared metamaterials as selective thermal emitters. *Phys. Rev. Lett.*, 107(4):045901, 2011.

[180] Yang Wang, Tianyi Sun, Trilochan Paudel, Yi Zhang, Zhifeng Ren, and Krzysztof Kempa. Metamaterial-plasmonic absorber structure for high efficiency amorphous silicon solar cells. *Nano Lett.*, 12(1):440–445, 2011.

[181] A. García-Etxarri, R. Gómez-Medina, L. S. Froufe-Pérez, C. López, L. Chantada, F. Scheffold, J. Aizpurua, M. Nieto-Vesperinas, and J. J. Sáenz. Strong magnetic response of submicron silicon particles in the infrared. *Opt. Express*, 19(6):4815–4826, March 2011.

[182] K Kambe. *Z. Naturforsch. A*, 23:1280, 1968.

[183] Cheng Yang, Gang Zhang, Hua Min Li, and Won Jong Yoo. Localized surface plasmon resonances caused by Ag nanoparticles on SiN for solar cell applications. *Journal of the Korean Physical Society*, 56:1488–1491, 2010.

[184] Z. Valy Vardeny, Ajay Nahata, and Amit Agrawal. Optics of photonic quasicrystals. *Nature Photonics*, 7(3):177–187, 2013.

[185] R. Zhang, Y. Zhang, Z. C. Dong, S. Jiang, C. Zhang, L. G. Chen, L. Zhang, Y. Liao, J. Aizpurua, Y. Luo, J. L. Yang, and J. G. Hou. Chemical mapping of a single molecule by plasmon-enhanced raman scattering. *Nature*, 498(7452):82–86, 2013.

[186] S. Pillai, K. R. Catchpole, T. Trupke, and M. A. Green. Surface plasmon enhanced silicon solar cells. *J. Appl. Phys.*, 101(9):093105, 2007.

[187] Yu. A. Akimov, W. S. Koh, S. Y. Sian, and S. Ren. Nanoparticle-enhanced thin film solar cells: Metallic or dielectric nanoparticles? *Appl. Phys. Lett.*, 96(7):073111–3, 2010.

[188] E. Wang, T. P. White, and K. R. Catchpole. Resonant enhancement of dielectric and metal nanoparticle arrays for light trapping in solar cells. *Opt. Express*, 20(12):13226–13237, 2012.

[189] Hongtao Cui, Supriya Pillai, Patrick Campbell, and Martin Green. A novel silver nanoparticle assisted texture as broadband antireflection coating for solar cell applications. *Solar Energy Materials and Solar Cells*, 109:233–239, 2013.

[190] K. J. Chau, G. D. Dice, and A. Y. Elezzabi. Coherent plasmonic enhanced terahertz transmission through random metallic media. *Phys. Rev. Lett.*, 94(17):173904, 2005.

[191] S. Grésillon, L. Aigouy, A. C. Boccara, J. C. Rivoal, X. Quelin, C. Desmarest, P. Gadenne, V. A. Shubin, A. K. Sarychev, and V. M. Shalaev. Experimental observation of localized optical excitations in random metal-dielectric films. *Phys. Rev. Lett.*, 82(22):4520, 1999.

[192] Sergey I. Bozhevolnyi, Valentyn S. Volkov, and Kristjan Leosson. Localization and waveguiding of surface plasmon polaritons in random nanostructures. *Phys. Rev. Lett.*, 89(18):186801, 2002.

[193] Vladimir M. Shalaev and Andrey K. Sarychev. Nonlinear optics of random metal-dielectric films. *Phys. Rev. B*, 57(20):13265–13288, 1998.

[194] Jun-ichi Nakayama, Kiyoshi Mitzutani, Hisanao Ogura, and Shinji Hayashi. Theory of light scattering from a random metal surface: Excitation of surface plasmons in a Ag film. *J. Appl. Phys.*, 56(5):1465–1472, 1984.

[195] Seok-Soon Kim, Seok-In Na, Jang Jo, Dong-Yu Kim, and Yoon-Chae Nah. Plasmon enhanced performance of organic solar cells using electrodeposited Ag nanoparticles. *Appl. Phys. Lett.*, 93(7):073307–3, 2008.

[196] B. Lee, J. Abelson, S. Bishop, D. Kang, B. Cheong, and K. Kim. Investigation of the optical and electronic properties of $Ge_2Sb_5Te_5$ phase change material in its amorphous, cubic, and hexagonal phases. *J. Appl. Phys.*, 97:1–8, 2005.

[197] D. E. Aspnes and A. A. Studna. Dielectric functions and optical parameters of Si, Ge, GaP, GaAs, GaSb, InP, InAs, and InSb from 1.5 to 6.0 eV. *Phys. Rev. B*, 27(2):985–1009, 1983.

[198] Edward D. Palik, editor. *Handbook of optical constants of solids*. Academic Press, 1985.

[199] I. Nagy. Short-range correlation in a two-dimensional electron gas. *Phys. Rev. B*, 52(3):1497–1499, 1995.

[200] Marian Rusek, Hervé Lagadec, and Thomas Blenski. Cluster explosion in an intense laser pulse: Thomas-fermi model. *Phys. Rev. A*, 63(1):013203, 2000.